# Surface Oxidation of Metallic Glasses and its Effects on Nanotribology

Dissertation
zur Erlangung des Grades
des Doktors der Naturwissenschaften
der Naturwissenschaftlich-Technischen Fakultät
der Universität des Saarlandes

Dipl. Phys. Kai Thomas Rittgen

Saarbrücken
2018

**Tag des Kolloquiums: 30.08.2018**

**Dekan: Prof. Dr. G. Kickelbick**

**Mitglieder des Prüfungsausschusses:**
**Prof. Dr. U. Hartmann (Vorsitzender)**
**Prof. Dr. R. Bennewitz**
**Prof. Dr. R. Birringer**
**Prof. Dr. R. Pelster**
**Dr. T. John**

**Eidesstattliche Versicherung**

Hiermit versichere ich an Eides statt, dass ich die vorliegende Arbeit selbständig und ohne Benutzung anderer als der angegebenen Hilfsmittel angefertigt habe. Die aus anderen Quellen oder indirekt übernommenen Daten und Konzepte sind unter Angabe der Quelle gekennzeichnet.

Die Arbeit wurde bisher weder im In- noch im Ausland in gleicher oder ähnlicher Form in einem Verfahren zur Erlangung eines akademischen Grades vorgelegt.

Datum, Unterschrift

# Zusammenfassung

Es werden grundlegende Mechanismen von Reibung und Verschleiß auf atomarer Skala auf metallischen Gläsern verschiedener Oxidationsstufen untersucht. Metallisches Glas wurde durch Saugguss hergestellt und mittels Röntgenbeugung und Dynamische Differenzkalorimetrie charakterisiert. Die Oberflächen wurden in kontrollierter Atmosphäre oxidiert und durch Elektronenmikroskopie und Röntgenphotoelektronenspektroskopie charakterisiert. Nanotribologische Experimente wurden mittels Rasterkraftmikroskopie im Ultrahochvakuum mit Normalkräften durchgeführt, deren Größenordnungen sich über drei Dekaden erstrecken. Die Oxidschicht auf $Zr_{60}Cu_{30}Al_{10}$ besteht hauptsächlich aus einer amorphen Matrix aus $ZrO_2$ und $Al_2O_3$ in welche kristalline $Cu_2O$-Nanopartikel eingebettet sind. Stick-Slip Reibung wurde sowohl auf dem metallischen Glas als auch auf der oxidierten Oberfläche gemessen. Vergleichende Messungen zeigten eine höhere Reibung und einen höheren Verschleiß nach der Oxidation. Aufgrund der Oberflächenrauhigkeit ist die Reibung auf der oxidierten Oberfläche abhängig von der Größenskala der Messung. Spitze Indenter ermöglichen das Eindringen in die Oxidschicht, was zu einem Aufschneiden der Oberfläche führt. Indenter mit größeren Kontaktflächen führen zunächst zu Plowing und schließlich zur Delamination der Oxidschicht vom metallischen Glas. Auf dem nicht oxidierten metallischen Glas wurde die plastische Verformung, unabhängig von der Kontaktfläche, Plowingmechanismen zugeordnet.

## Abstract

Fundamental mechanisms of friction and wear on the atomic scale were studied for different oxidation states of metallic glass surfaces. Bulk metallic glass was prepared by suction casting and characterised by X-Ray Diffraction and Dynamic Scanning Calorimetry. Surfaces were oxidised in controlled atmosphere and characterised by Electron Microscopy and X-ray Photoelectron Spectroscopy. Tribological experiments on the nano-scale were performed by Atomic Force Microscopy in ultra-high vacuum on a continuous load scale extending over three decades with different cantilevers. The oxide layer on $Zr_{60}Cu_{30}Al_{10}$ consists mainly of an amorphous matrix of $ZrO_2$ and $Al_2O_3$ with embedded crystalline $Cu_2O$ nanoparticles. Stick-slip friction was found on both, the metallic glass and on the oxidised surface. Comparative experiments revealed higher friction and wear after oxidation. Due to the surface roughness, friction is scale dependent on the oxidised surface. Sharp indenters were found to penetrate the oxide surface resulting in cutting wear. Indenters with larger contact areas initiate plowing and eventually delamination from the surface of metallic glass. On the clean metallic glass, plastic deformation was attributed to plowing mechanisms, independent on the contact area.

# Contents

# Abbreviations

| | |
|---|---|
| **AES** | **A**uger **E**lectron **S**pectroscopy |
| **AFM** | **A**tomic **F**orce **M**icroscopy |
| **DSC** | **D**ifferential **S**canning **C**alorimetry |
| **EDX** | **E**nergy **D**ispersive **X**-ray Analysis |
| **FFM** | **F**riction **F**orce **M**icroscopy |
| **FIB** | **F**ocussed **I**on **B**eam |
| **GFA** | **G**lass **F**orming **A**bility |
| **SEM** | **S**canning **E**lectron **M**icroscopy |
| **TEM** | **T**ransmission **E**lectron **M**icroscopy |
| **TGA** | **T**hermo **G**ravimetric **A**nalysis |
| **UHV** | **U**ltra-**H**igh **V**acuum |
| **XPS** | **X**-ray **P**hotoelectron **S**pectroscopy |
| **XRD** | **X**-**R**ay **D**iffraction |

# 1 Introduction

Owing to their high strength and hardness metallic glasses have been recognised as potential materials with enhanced wear resistance for tribological applications. While metallic glasses are prone to oxidation, the formation of surface oxide and its impact on tribological properties has been scarcely investigated.
This chapter provides a brief scholarly classification of the present work, and an overview of previous studies. In addition, an introduction on the history of the topic of this thesis and motivating aspects are presented.

## 1.1 From tribology to nanotribology

The words nano and tribology are derived from the greek words nános, which means "dwarf", and tribos, which means "rub". Tribology as a "science of friction" deals with the interaction of surfaces, which are in mechanical contact and are moved relative to each other. In addition to friction and lubrication, tribology is also related to the mechanical resistance of surfaces as well as their wear mechanisms. It includes scientific disciplines such as physics, chemistry, applied mathematics, solid state physics, fluid dynamics, thermodynamics, rheology and materials science.
In 1699 Amonton stated that the friction force between two surfaces is independent on the contact area and proportional to the normal load. He explained this result in terms of interlocking mechanisms between both surfaces. The friction force is then a result of lifting the asperities from one interlock to the next during motion of both surfaces relative to each other. Later, in 1785, Coulomb observed that the friction force is independent on sliding velocity. After further work was carried out by Rennie (1829) he suggested to take into account the bending and fracture of asperities. The action of lubricants was attributed to the filling of irregularities which leads to a more "slippery" contact. Around 1930 Sir William Hardy discovered the importance of lubricating boundary layers on the friction between solids. In 1929 Tomlinson stated that the friction force is due to energy dissipation when surface molecules are forced into each other and are then separated. Through systematic experiments by Bowden and Tabor it was shown that macroscopic friction can indeed be described by the collective interaction of many small asperities. In the case of smaller contact surfaces basic empirical laws are not always tenable.[1 Introduction] The larger the relation between surface area and volume of the respective contact partners, the greater the influence of adhesion, the surface structures, and their chemical properties. The development of the scanning force microscope as well as experiments with the surface-force apparatus and the quartz microbalance finally

led to the field of nanotribology. The reduction of contact area to a single asperity reduces the complexity of friction studies which provides basic insights into the relevant processes on atomic scale. During friction force microscopy the deflection of a force sensor's sliding tip, which is in contact to the sample surface, is related to the friction force. For a complete understanding of friction mechanisms the exact knowledge of atomic configuration at the interface between both contact partners is prerequisite. For friction measurements with scanning force microscope sample surfaces can often be obtained with atomic precision, whereas the atomic constitution of the tip's contact apex is usually less controlled. In addition, the transfer of atoms between the contact partners during sliding affects the friction process and has to be considered.(chapter 1 in [2])
The ability to investigate friction and wear on the atomic scale enabled the measurement of atomic stick-slip by Mate et. al. in 1987. Four years later, in 1991 Hirano et. al. explored friction anisotropy in the contact of two mica sheets, and 1997 Hirano et. al. observed superlubrication in the case of incommensurate surface structures. In 1997 Schwarz et. al. found a nonlinearity of friction force with the load and confirmed the presence of Hertzian contact during sliding on carbon substrates. Chemical forces were quantitatively measured for a single atomic bond by dynamic force microscopy in ultra-high vacuum by Lantz et. al. in 2001, and in 2002 Gnecco et. al imaged discrete plastic deformation phenomena on the atomic scale after nucleation of single dislocations by scratching on potassium bromide.[3]

## 1.2 From tribology of metallic glasses to nanotribology of their oxide surfaces

Since the discovery of metallic glasses, the physical parameters derived from their equations of state have been subject of intense research. Due to their amorphous structure metallic glasses show lack of microstructural features such as grain boundaries. This enables amorphous metals to exhibit different mechanical, thermal and electromagnetic properties compared to those of crystalline metallic materials. In addition to their high hardness and their corrosion resistance fig. 1.1 illustrates the superiority of metallic glasses over other material classes in terms of mechanical yield strength and fracture toughness. These properties, which are often preferred in practice, enable their application in MEMS (Micro Electro Mechanical Systems) and NEMS (Nano Electro Mechanical Systems).[4]

Depending on the rate of deformation, metallic glasses undergo a serrated flow which is attributed to local atomic arrangements within the material.[7] This phenomenon was observed during nano-indentation studies as well as micrometer scale

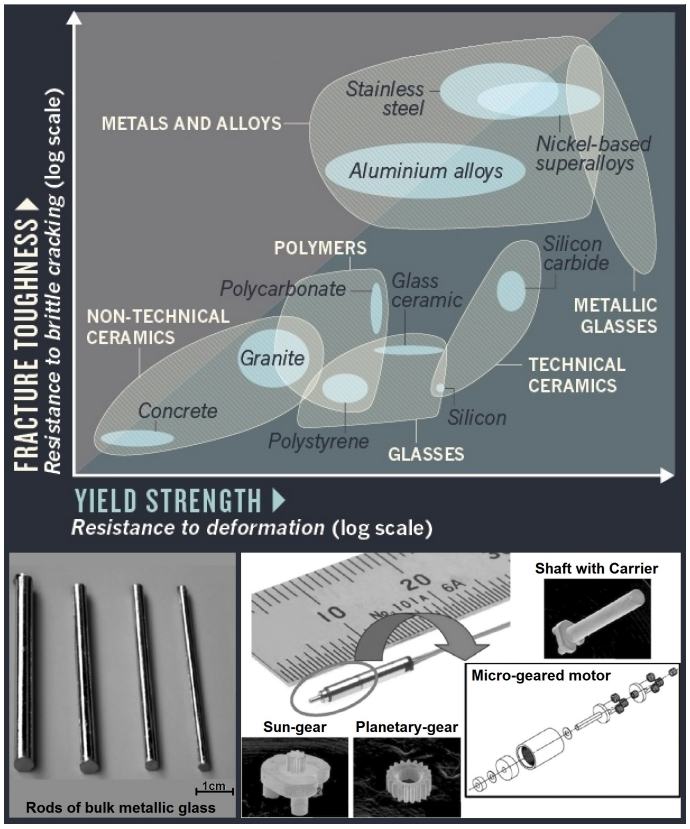


Figure 1.1: Classification of metallic glasses compared to other materials with regard to their yield strength and fracture toughness. Photographs of metallic glass rods are shown below together with an example for its application in NEMS devices. Graph from [6], images from [5].

scratch experiments on the surface of metallic glasses. Thereby, an enhanced wear resistance with increasing hardness was found.[8] Friction on metallic glasses is influenced by structural relaxation processes within the material.[9] This explains that, as long as measurements are not influenced by thermal effects, microscale friction was found to decrease with increasing sliding speed. Furthermore, friction and wear are not intrinsic properties and depend on the test environments. While the coefficients of friction on different metallic glasses depend only slightly on the materials composition, significant differences in the wear performance was observed. Compared to magnesium or nickel based metallic glasses, compositions based on titanium, copper, or zirconium revealed a higher wear resistance. After scratching debris was found to be partially crystallised.[10] Superior abrasive properties of metallic glasses compared to that of steel were mainly attributed to their high hardness.[11] Also the formation of protective oxide layers and material transfer during sliding influence the wear process. It was found that, depending on its direction, the material transfer

between contact partners lead to higher or reduced wear of the metallic glass.[12] Indentation studies on passivating films on metals revealed a high strength of the surfaces which drops dramatically at a yield point which is caused by the films fracture process.[13][14]

On zirconium based metallic glass, sliding in air resulted in a lower friction coefficient compared with sliding in vacuum. In air, wear mechanisms are accompanied by the oxidation of metallic constituents. Interfacial mixing due to plastic deformation and material transfer was found to determine the friction and wear mechanisms in case of sliding with a metallic counterface body. The most common type of debris was of flake and plate like shape. Although the zirconium based metallic glass had limited tensile ductility, it was ductile under sliding conditions and a subsurface material flow was observed due to the combination of shear and compression. After sliding, a decreased hardness of metallic glass was found and attributed to a wear softening effect. Increasing load in both vacuum and air resulted in an increased amount of wear volume.[15][16] Most freshly cleaned crystalline metals acquire an oxide layer of a few nanometers within the first minutes after exposure to air. During oxidation the oxide will either take on the same structure as the parent metal, or another independent structure which is bond to the metal at the coincident points of the lattices. An oxide layer prevents the metal and the counterface body from direct contact and a mostly low ductility of the oxide layer leads to lower friction until oxide breakdown at high loads.(chapter 5 in [1])

Tribological studies with AFM on the nanoscale showed that on a nickel based metallic glass the friction and adhesion between the sample surface and a Silicon-tip increase after surface oxidation at elevated temperature.[17] A strong positive correlation between produced wear volume and friction force on the oxidised surface has been revealed.[18] Scratch experiments with a chemical inert diamond tip on an oxidised surface of copper based metallic glass, revealed less wear volume on the oxidised surface compared to a polished surface after both, single and cyclic scratching.[19]

On zirconium based metallic glasses the oxide structure was found to be mainly amorphous with inclusions of crystalline phases.[20, 21]

The complexity of oxide growth on metallic glasses is demonstrated in fig. 1.2 which shows the different topographies of the oxidised surfaces of zirconium, copper, and an amorphous metal, consisting zirconium, copper, and aluminium. While the oxide on zirconium appears to be smooth and homogeneously distributed on the metals surface, on the copper surface oxidation has mainly affected the regions of the grain boundaries, and the copper oxide reveals a particle like structure. The last image

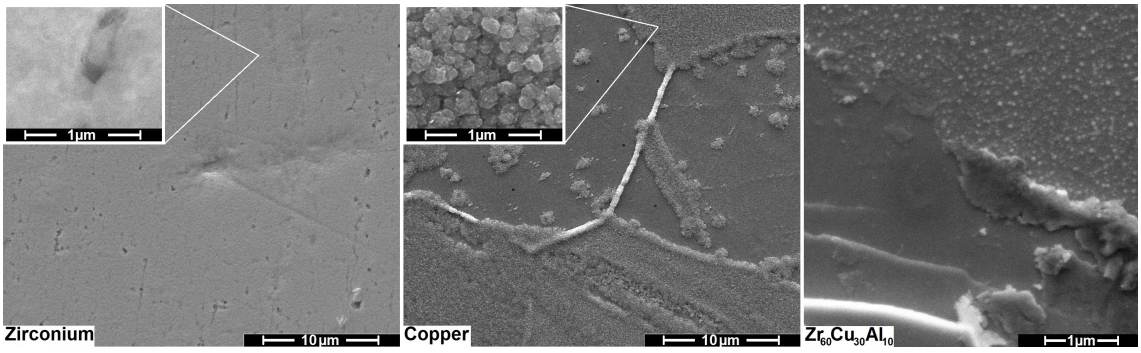


Figure 1.2: Secondary Electron Microscopical images of surfaces of Zr, Cu, and $Zr_{60}Cu_{30}Al_{10}$ bulk metallic glass after oxidation at 450K for 30min in synthetic air. The image of $Zr_{60}Cu_{30}Al_{10}$ shows the periphery of a scratch.

shows the periphery of a scratch on the oxidised surface of a zirconium based metallic glass with the oxide peeled of from the smooth surface of the amorphous metal. The oxide appears as a mixture of the oxides on the pure metals. Aforementioned studies studies have revealed structural as well as chemical compositions of oxide layers on zirconium based metallic glasses. Nevertheless, from their results it is only scarcely possible to draw definite conclusions as to which extend any constituent has affected each observed tribological phenomenon. As a result, fundamental mechanisms of friction and wear on oxides of metallic glasses are still unclear. Therefore, in this work, the results of recent previous studies were supplemented according to the following five aspects:

1. The oxidised surfaces were prepared in controlled atmosphere to prevent the influence of water, adhered to surfaces, on the oxidation due to the formation of hydrates.

2. Experiments were performed in ultra-high vacuum to prevent any adhesion of monolayers of water to the surfaces which may influence the experiments on the nanometer scale.

3. The correlation between the tribology of the surface oxide and of the clean surface of metallic glass was explored which was enabled by comparative investigations on the pure metal, due to experiments in inert atmosphere.

4. High resolution investigations down to the atomic scale were performed to achieve insights into the very fundamental mechanisms contributing to friction and wear.

5. Friction and wear mechanisms were attributed to the individual constituents of the oxide layers which therefore had to be identified due to comprehensive surface characterisation.

We ensured and confirmed the reproducibility of a representative oxide layer by surface preparations under controlled conditions, such as oxidation atmosphere, temperature, and time of exposure. We encountered the structure and chemistry of oxides on the metallic glass with Electron Microscopy, X-Ray Diffraction, and X-ray Photoelectron Spectroscopy. Studies using Atomic Force Microscopy in ultra-high vacuum enabled differentiated tribological investigations of the influences of surface properties on the friction and wear on clean and oxidised metallic glass on the nanometer scale.

# 2 Preparation

The design of reproducible experiments requires the capability to produce reliable sample material in terms of structure and composition. In this chapter the preparation of surfaces for nanotribological investigations is presented, beginning with the casting of $Zr_{60}Cu_{30}Al_{10}$ bulk metallic glass. The production process was monitored by verification of the amorphous structure of the sample material by X-Ray Diffraction technique. Thermal characterisation was carried out by Differential Scanning Calorimetry. Surface treatments such as grinding and polishing which are necessary to obtain a smooth topography, sufficient for examinations by Atomic Force Microscope, are described. Finally, the process of surface oxidation under controlled thermal conditions and atmosphere is presented. The chapter closes with a discussion of materials and characterisation results which will be important for further discussion of results presented in subsequent chapters.

## 2.1 Production of amorphous metals

To form an amorphous structure by cooling from an equilibrium liquid is equivalent to suppress a crystallisation within the supercooled liquid. For the kinetics of glass formation the viscosity is an important parameter because it reflects the mobility of the atoms during supercooling. In most cases the temperature dependence of the viscosity $\eta$ can be described by the Vogel-Fulcher-Tammann (VFT) relation.

$$\eta = \eta_0 \exp\left(\frac{DT_0}{T - T_0}\right) \tag{2.1}$$

Here, $T$ is the temperature, $T_0$ is the Vogel-Fulcher temperature, and $D$ is a characteristic parameter of the liquid. The structure changes quickly at high temperatures during temperature changes but becomes sluggish below the glass transition. When a liquid is rapidly cooled, the glass transition occurs at higher temperature and retards the formation of stable nuclei in the melt. The poor mobility of constituents inhibits the growth of thermodynamically favored phases.(chapter 2 in [5]) This process is illustrated in fig. 2.1a, where a phase diagram of an alloy, consisting of two components $A$ and $B$, is shown. When the melt is cooled slowly, it solidifies at the point $X$, a phase enriched with component $A$ crystallises and the remaining material moves towards the eutectic point $E$ where the final crystallisation as a solid mixture of composition $E$ takes place. At high cooling rates the equilibrium is prevented and the material formed is a nonequilibrium uniform glass.(chapter 1 in [22]) In fig. 2.1b the evolution of enthalpy is depicted for the process of rapid

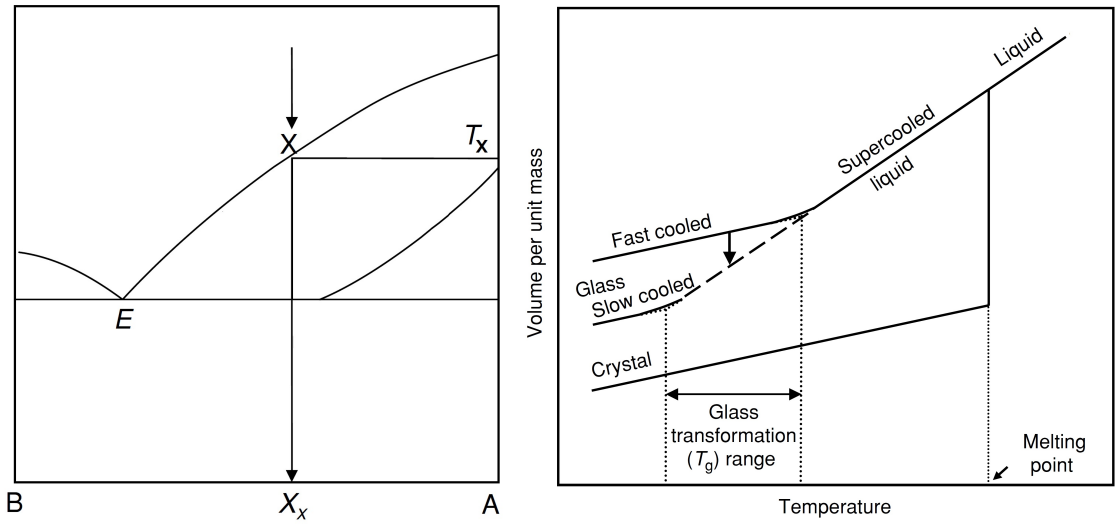


(a) Phase diagram of a binary alloy.

(b) Evolution of enthalpy of an alloy due to cooling from a melt.

Figure 2.1: Illustrations of the thermodynamical processes during cooling an alloy from a melt into an amorphous material. a) from [22], b) from [5]

cooling which leaves the system frozen above the glass transition with a high volume.(chapter 2 in [5])

Since the discovery of metallic glasses much research effort has been devoted to the examination of their thermodynamics and thermophysical properties. These include schemes to assess the glass forming ability of metallic glasses, such as structural models, nearly free electron theory, chemical factors, phase diagram features, minimum volume criterion, atomic size criterion, and solid solution criterion. According to Inoue, in addition to a sufficient cooling rate, intrinsic parameters play a significant role in the formation of metallic glasses during the production process. The glass forming ability of a metallic alloy is influenced by the following aspects:

- Multicomponent systems consisting of more than three elements improve the glass forming ability since a larger number of elements destabilises competing crystalline phases.
- A significant difference in atomic size ratios above about 12 leads to complex structures that crystallises less easily.
- Negative heat of mixing of the main constituent elements leads to a preferred binding between unlike elements.

Most of the criteria in these approaches are difficult to quantify in practice. Therefore, several simple parameters were constructed for various metallic systems, which should serve as a qualitative description of the glass forming ability (GFA). Turnbull proposed the reduced glass transition temperature, the ratio of the glass transition temperature, and the liquidus temperature, as being a representative indicator for the GFA. It includes the assumption that the nucleation frequency of a melt scales inversely with the liquid's viscosity. Since this idea was based on a monoatomic system, the supercooled liquid region, especially its range given by the temperature difference between the onset crystallisation temperature and the glass transition temperature, has been proposed as a new GFA indicator by Inoue. The idea was that the supercooled liquid stability prevents crystallisation. Fang et al. observed a correlation between both the atomic size difference and the electronegativity difference with the supercooled liquid region in bulk metallic glasses. The $\gamma$ indicator was presented as the most reliable indicator of the ease by which a liquid can be obtained as amorphous material by cooling. In order to form an amorphous solid material, the liquid has to be cooled without intersecting the time-temperature curve which is shown fig. 2.2a. To bypass the curve, a minimum cooling rate is required. The arithmetic average of glass transition and liquidus temperature is then correlated to the ability of glass formation. The diagram in fig. 2.2b shows the concept for how the $\gamma$ parameter is related to the liquidus and crystallisation temperature ($T_l$ and $T_x$) as well as the glass transition temperature $T_g$. The expression for $\gamma$ is then given by

$$\gamma \propto \frac{T_x}{T_l + T_g} \tag{2.2}$$

(chapter 4 in [5])

Various methods have been developed to obtain adequate cooling rates for the production of metallic glasses. For bulk metallic glasses suction casting has proven to be a successful method to produce amorphous metal samples in dimensions of a few millimeter with cooling rates of up to $10^3 Ks^{-1}$. For melting an arc is generated between two electrodes, of which is one formed by the alloy, the other one by a water-cooled tungsten electrode. The arc is carried by ionised gas. For this purpose argon is used, which also serves as a protective gas to prevent oxidative reactions. During the suction process, the liquid melt is transported from the pouring funnel of the crucible into a water-cooled hollow mould of the crucible by evacuating from the end face opposite the inlet funnel. Numerical simulations provided evidence that the

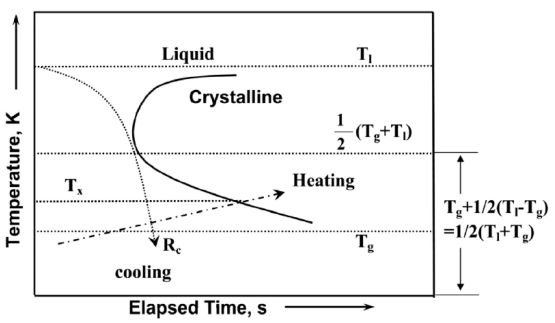


(a) Time-Temperature graph of an alloy undergoing crystallisation by high cooling rate.

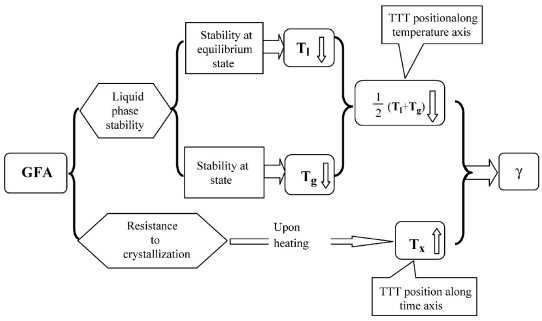


(b) Schematics of the concept of the $\gamma$ parameter as reliable indicator for GFA.

Figure 2.2: Concept of discussing the glass forming ability in terms of thermodynamical processes. a) from [5], b) from [23].

cooling rate is highest at the surface of the melt, especially at the transition between melt and crucible material. A large ratio between surface area and volume of the sample favors the formation of a completely amorphous sample. A sufficiently long cooling phase is necessary, since a short cooling period has a negative effect on the overall cooling rate due to residual heat, released from the center of the specimen. These results were obtained by the simulation of a horizontal continuous casting process, but were considered to be applicable on the suction casting process.[24] Similar results have been obtained by Li et. al. who found crystalline phases in the center of the bulk material after a suction casting process of Zr-based metallic glass.[25]

**Preparation of $Zr_{60}Cu_{30}Al_{10}$ bulk metallic glass by suction casting**

At first the high purity metals Zr, Cu, and Al were weighed by means of a laboratory scale with a precise of $3 \cdot 10^{-4}$g and cleaned in an ultrasonic bath, first with acetone, then with ethanol. The material was then placed in a crucible plate of an arc melting furnace together with getter material, consisting of two pieces of titanium, in a separate crucible. After the oven was vacuum sealed, the interior was evacuated to below $5 \cdot 10^{-2}$mbar and then flooded with argon to 0,5 bar. This procedure was repeated five times to produce a pure argon atmosphere. Finally, the furnace interior was evacuated to below $1 \cdot 10^{-4}$mbar and immediately flooded to 0,5 bar with argon. Then, the water cooling of the electrode and crucible plate was switched on. Before each melting of sample material, the getter material was melted in order to free the interior of the furnace from residual oxygen molecules. After the sample was melted and cooled three times to obtain a homogeneous alloy, the argon pressure was increased by a few tenths of a bar to allow an optimal extraction process into the

hollow suction crucible. Then, the sample material was transferred into the cooled suction crucible. Immediately after the suction process, the electrode was switched off and after a cooling time of at least five minutes, the interior of the furnace was brought to normal pressure by means of argon supply. The furnace was opened and the solidified sample was removed. Before and after each use, the furnace, in particular crucible and crucible plate, electrode, and getter material were thoroughly cleaned. Depending on the suction crucible, specimens of different geometries were produced. The furnace, different crucibles, and an illustration of the melting and suction process are presented in fig. 2.3.

## 2.2 Macroscopic characterisation

The amorphous structure of the samples was verified by X-Ray Diffraction (XRD). This technique was also applied to identify crystalline phases in order to improve the preparation process. The determination of the glass transition temperature and crystallisation temperature by Differential Scanning Calorimetry (DSC) allowed the planning of oxidation treatments of the sample surfaces. Reproducible friction experiments require the reproducibility of the mechanical properties of the amorphous metals. Crystallite particles, oxygen, and hydrogen embrittlements as well as structural relaxation contribute to the degeneration of mechanical properties. While all these factors can be influenced by the production process, the structural relaxation is an unavoidable intrinsic phenomenon of large sized metallic glasses.[26] Therefore, additional thermal analyses by means of DSC were carried out to identify any enthalpic relaxation caused by annealing treatment.

### 2.2.1 Structural analysis

X-Ray Diffraction is a non-destructive analytical technique based on elastic scattering of X-ray photons in matter, revealing structural information of the material. When a monochromatic beam of X-rays hit an atom either coherent scattering or incoherent scattering of photons occur. Coherent scattering happens if bound electrons are set into oscillation and radiate X-rays of the same wavelength as that of the incident beam. If the energy and the moment of both collision partners are changed during the collision, it is called incoherent scattering. For different electrons coherent radiation waves are phase shifted because the electrons of an atom are situated at different points in space. The efficiency of scattering of a given atom in a given direction is represented by the atomic scattering factor $f$. It is the ration between the wave scattered by an atom to the amplitude of the wave amplitude, scattered

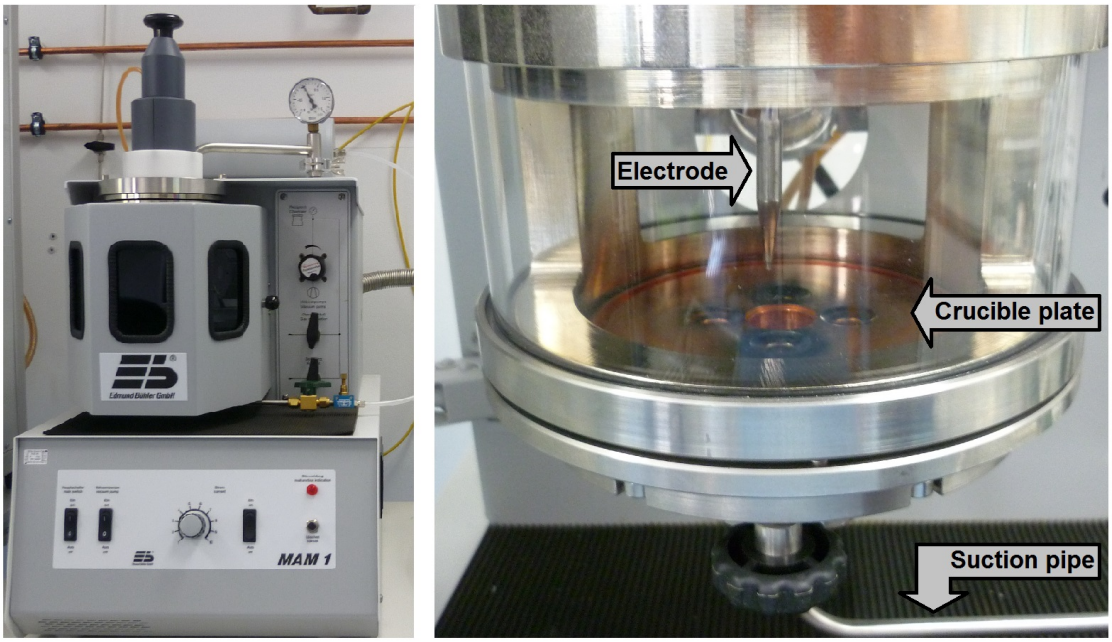


(a) left: Melting furnace of type Edmund Bühler MAM-1 with equipment for suction casting. The pump assembly, consisting of roughing pump and turbo pump, is not shown here. right: melting chamber with tungsten electrode and crucible plate. The hole in the center of the plate is where a crucible, as shown in b), is placed.

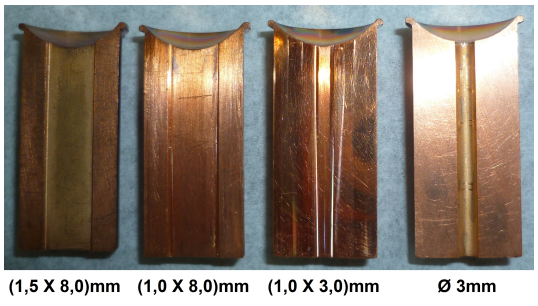


(b) Copper crucibles for suction casting with different sample geometries. Length is always 30mm, whereas cross sectional dimensions are given in the image.

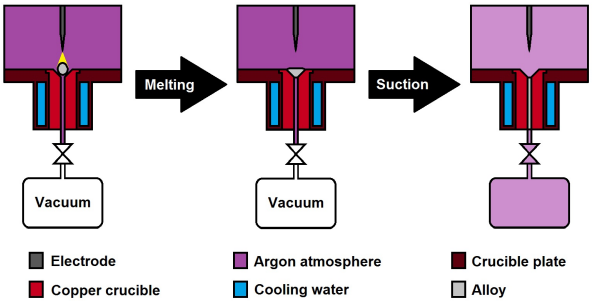


(c) Schematics of the melting procedure with subsequential suction casting.

Figure 2.3: Illustration of the production process of metallic glass including presentation of melting furnace and equipment for suction casting

by one electron. If the atom is part of a group of atoms, their arrangement affects the intensity of diffracted radiation. The resulting wave, scattered by all the atoms of the unit cell, is represented by the structure factor $F$ by taking into account the different phases of each wave scattered at an atom:

$$F_{hkl} = \sum f_n e^{2\pi i[hu_n + kv_n + lw_n]} \tag{2.3}$$

with coordinates of atoms $u$, $v$, $w$, and Miller indices $h$, $k$, $l$ whereby the summation expands over all atoms of the unit cell. The structure factor gives the ratio between the amplitude of the wave, scattered by all the atoms of a unit cell, to the amplitude of the wave scattered by one electron. Since $F$ is the Fourier transform of the electron density, the methods of X-ray diffraction give an image of the electron density distribution within the sample material at high resolution. For a perfect crystalline solid the intensity of a scattered X-ray beam versus the diffraction angle $2\theta$ is almost zero at every measured angle, except at certain angles of diffracted beams. Amorphous structures only show a statistical preference for a particular interatomic distance which results in a X-ray scattering curve with one or two broad maxima. From X-ray diffraction one obtains three information, such as the diffraction angle, the intensity of the diffracted radiation as well as the line form. From the diffraction angles $2\theta$, lattice parameters can be calculated, and by indexing methods the dimensions and symmetry of the elementary cell can be determined. From the reflex intensities and a crystal structure analysis it is possible to make statements about the three-dimensional arrangement of the atoms in the crystalline material. The line shape of the diffraction interferences allows the investigation of the grain size and the crystallisation state.[27]

**Structural characterisation by XRD**

For a structural characterisation by XRD the surfaces of the specimens were ground 250$\mu$m with SiC paper with an average grain size of 26$\mu$m and water supply. The surfaces were cleaned with ethanol after which the measurements were carried out by a Bruker axs D8 Advance by the use of the CuK($\alpha$) line ($\lambda$ = 0,15418nm). The plots in fig. 2.4 showing the results of measurements of $Zr_{60}Cu_{30}Al_{10}$-samples. The upper plot of fig. 2.4 shows a graph obtained after suction casting with a crucible of 1,5mm sample thickness. The short-range order of an amorphous phase is clearly visible between 30° and 45°, whereas it is superimposed by refraction peaks of two crystalline phases. The refraction peaks indicated by grey arrows correspond to tetragonal $CuZr_2$ and the peaks indicated by black arrows correspond to rhombohedral $CuAlO_2$. A graph of a fully amorphous sample material can be

seen in the center plot of fig. 2.4. This specimen was obtained by using a crucible with a sample thickness of 1,0mm. Only the effect of the short range order is visible between 30° and 45° and the next higher order between 55° and 80°. The bottom XRD-graph in fig. 2.4 was obtained after the annealing of the sample for 30min at a temperature of 573K in argon atmosphere. As can be seen, no refraction peaks can be found which indicates an amorphous structure, at least in the surface near region, after the thermal treatment. In all graphs the intensity of the primary X-ray beam can be seen as decaying signal at small angles. Further experiments regarding the production process were performed by the attempt to produce amorphous alloy of different compositions. Table 1.1 shows the number of successful attempts to produce different alloys cast with different crucibles, which were identified as amorphous by means of XRD. Amorphous binary systems based on zirconium are hard to produce.

| | (1,5 X 8,0)mm | (1,0 X 8,0)mm | (1,0 X 3,0)mm | Ø 3,0mm |
|---|---|---|---|---|
| Surface to Volume ratio [$mm^{-1}$] | 1,7 | 2,3 | 2,7 | 1,4 |
| $Zr_{60}Cu_{30}Al_{10}$ | 0/2 | 7/8 | n.t. | 1/1 |
| $Zr_{50}Cu_{50}$ | 0/1 | 0/1 | 0/3 | 0/1 |
| $Zr_{42}Al_{58}$ | n.t. | 0/1 | n.t. | n.t. |
| $Ni_{60}Nb_{40}$ | n.t. | 0/3 | 0/3 | n.t. |
| $Ni_{62}Nb_{38}$ | n.t. | n.t. | 2/5 | n.t. |
| $Ni_{50}Nb_{50}$ | n.t. | n.t. | 0/1 | n.t. |
| $Zr_{60}Cu_{17,5}Al_{13,5}Ni_{8,5}Nb_{0,5}$ | n.t. | n.t. | 1/2 | n.t. |

Table 1.1: Probability, to produce fully amorphous sample material with a given crucible. n.t.: not tested.

Sample material which was produced by using the crucible for 1,5mm thick specimen were not fully amorphous according to XRD. After increasing the ratio between specimen surface and its volume by a factor of about 1,4, which was provided by the small crucible for 1mm specimen thickness, amorphous alloys could be produced. Impurities such as oxygen which may initialise nucleation of crystallisation, may lead not only to the formation of crystalline oxides but also may give rise to the nucleation of metallic nanocrystalline phases. Gebert et. al. [28] found a strong effect of even low oxygen concentrations on the GFA of a Zr based metallic glass, prepared by die casting into a copper mould. Oxygen also affects the crystallisation behavior and the thermal stability of the material by triggering the nucleation of metastable nanocrystalline phases during annealing. In our case, the change of crucible was the only change, whereas the atmosphere during the melting process was prepared the same way as before. It can be concluded that the higher cooling rate, provided by the small crucible, was the significant factor in suppressing crystallisation. However,

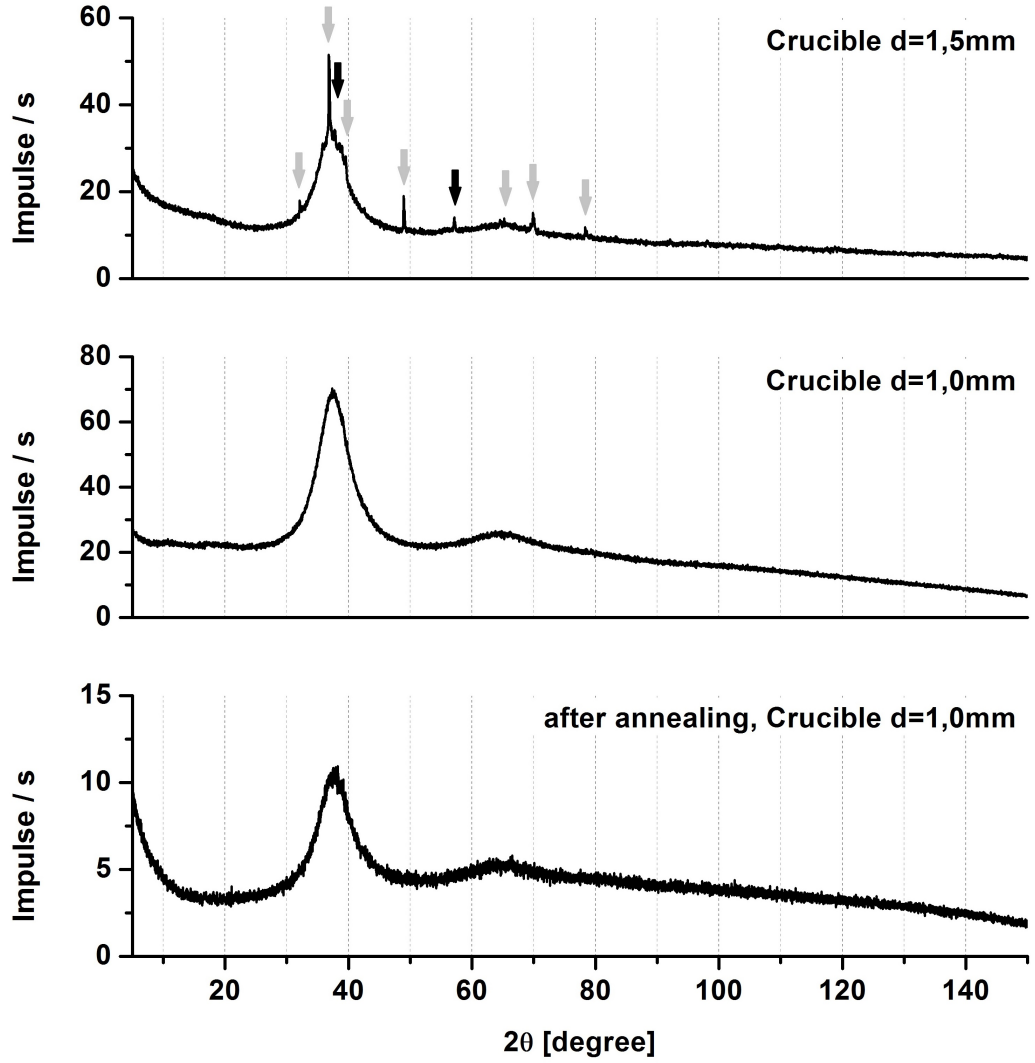


Figure 2.4: XRD-Plots of $Zr_{60}Cu_{30}Al_{10}$ obtained from suction casting. First graph corresponds to the as-cast sample casted in crucible for sample thickness of 1,5mm. Refraction peaks corresponding to $CuZr_2$ (grey arrows) and $CuAlO_2$ (black arrows). Center graph corresponds to the as-cast sample casted in crucible for sample thickness of 1,0mm. Bottom graph corresponds to the sample casted in crucible for sample thickness of 1,0mm, and annealed at 573K for 30min in argon atmosphere.

the purity of atmosphere is difficult to estimate, so it is still possible that there was a certain influence of oxygen, which was suppressed by the high cooling rate.
The production process was tested for different alloys and it was shown that in case of binary Ni-based alloys a variation in the ratio of the composition can increase the probability to obtain a metallic glass. Depending on the temperature of the molten material shortly before the suction process, the melt became sticky during the casting which is why the melting pot was not fully filled.

### 2.2.2 Thermal analysis

A DSC provides information about the heat flow inside or outside a sample's surface when it's heated, cooled, or held isothermally together with the temperature at which these changes occur. The sample material is sealed in a pan which is placed in a furnace next to a reference sample, and heated according to a pre-programmed temperature profile. If the sample material undergoes a transition while heating, a temperature difference is created between sample and the reference which is proportional to the heat flow in between. The total heat flow, represented by $\frac{dQ}{dt}$, comprise contributions from two sources, heat capacity ($C_p$) effects and any other processes, like phase transformations or chemical reactions represented by $f(T,t)$:

$$\frac{dQ}{dt} = C_p \frac{dT}{dt} + f(T,t) \tag{2.4}$$

where $t$ is the time, and $T$ is the temperature. After a baseline correction several parameters may be determined from the DSC data, such as the onset temperature of a thermodynamical transition or the enthalpy in an isobaric process by the integration of the heat flow with respect to the time. DSC measurements usually take place under a continuous flow of inert gas to prevent oxidation during the thermal treatment.(chapter 1 in [22])
According to Kissinger [29], a non-isothermal crystallisation occurs at the temperature where the reaction rate is a maximum. With respect to Arhenius' laws of reaction kinetics a first-order reaction of amorphous to crystalline transformation is described by:

$$ln\left(\frac{\beta}{T_x^2}\right) = -\frac{E_A}{RT_x} + const. \tag{2.5}$$

with the gas constant $R$, the activation energy for crystallisation $E_A$, and the heating rate $\beta$. Moynihan et. al. [30] interpreted the glass transition in terms of thermal relaxation and stated that the activation energy can be related to the glass transition

and $\beta$ by

$$ln\,(\beta) = -\frac{E_A}{RT_g} + const. \tag{2.6}$$

The glass transition of a material is not a fixed thermodynamic event, but depends to some extent upon how it has been cooled. The mechanically induced stresses, resulting from the production of the sample, may relax if the metallic glass is cooled slowly through $T_g$ or held just below the glass transition for a period of time. This process can be described by the transition into a lower enthalpy state. A slight overshoot of the heat flow at the glass transition of an annealed material can be observed, because at this point the material will pass into an energy state which is below its equilibrium energy state. When the material passes through $T_g$ and the materials structure becomes mobile they will also absorb energy in order to regain equilibrium, giving rise to a small endotherm.(chapter 4 in [22])[31]

**Thermal analyses by DSC**

The samples used for the thermal analyses had masses of about 20mg. Each specimen was put into a perforated aluminium crucible, with a mass of about 50mg. The samples were then treated in a DSC of type Metler Toledo DSC1 Star System under argon flux. The treatments consisted of heating up from 25°C to a temperature above the estimated crystallisation with a given heating rate and then cooling from 550°C to 25°C with the same rate. As heating rate 20Kmin$^{-1}$, 30Kmin$^{-1}$, 40Kmin$^{-1}$, 50Kmin$^{-1}$ and 60Kmin$^{-1}$ were chosen.

The graph in fig. 2.5a shows the heat flow of the sample to the reference sample as a function of the temperature at a heating rate of 20Kmin$^{-1}$. A baseline correction was performed by subtracting the curve of the cooling process from that of the heating process. The glass transition between 650K and 700K as well as the crystallisation peak just behind 700K are visible. The glass transition temperature $T_g$ and the crystallisation temperature $T_x$ were determined as the respective intersection points of the linear regressions of the heat flow curve shortly before and shortly after the corresponding transition. For a heating rate of 20Kmin$^{-1}$ the glass transition temperature was found to be $T_g = (668 \pm 4)$K and the crystallisation temperature was $T_x = (745 \pm 30)$K. The crystallisation enthalpy at a heating rate of 20Kmin$^{-1}$ was $H_x = (3{,}5 \pm 0{,}3)\text{kJ} \cdot \text{mol}^{-1}$.
A comparative measurement was performed with a sample previously annealed at about $573K$ for 30min in an argon flux. According to DSC measurements, no significant overshoot of the heat flow at the glass transition was observed, as can be seen in the zoom-in of fig. 2.5a which suggests that there occurred no enthalpic

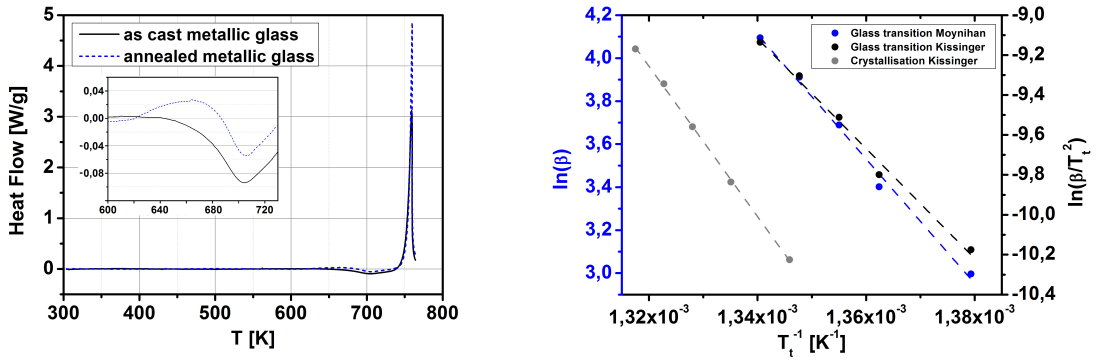


(a) Heat flow as function of temperature for an as-cast and an annealed sample of metallic glass. The heating rate was 20Kmin$^{-1}$. The inset represents a zoom-in of the glass transition region.

(b) Analysis of the glass transition and the crystallisation of the as-cast sample according to Kissinger and Moynihan. Depending on the kind of transition $T_t$ refers to $T_g$ or $T_x$.

Figure 2.5: Thermal analysis of $Zr_{60}Cu_{30}Al_{10}$ bulk metallic glass samples after measurements and thermal treatments in DSC. Physical units in the logarithm were neglected in accordance to [29] and [30].

relaxation within the material after annealing. Because of this finding no annealing of the sample material after suction casting and before further preparations was performed.

Fig. 2.5b shows Kissinger plots for the glass transition and for the crystallisation. Additionally, a Moynihan graph is plotted for the glass transition. The activation energy for the corresponding transition could be determined by linear regression. For the crystallisation the activation energy was found to be $E_a = (313 \pm 5)\text{kJ}\cdot\text{mol}^{-1}$. For the glass transition $E_a = (229 \pm 12)\text{kJ} \cdot \text{mol}^{-1}$ was determined as activation energy according to Kissinger's method. The Moynihan plot for the glass transition leads to an activation energy of $E_a = (241 \pm 11)\text{kJ} \cdot \text{mol}^{-1}$, which is in agreement with the value obtained from the Kissinger plot within the error.

Temperatures of glass transition and crystallisation achieved by DSC are in agreement to data found in literature, such as [32]. Compared to alloys of same chemistry but different stoichiometry the supercooled liquid region with a width of about 77K indicates a thermally very stable metallic glass.

The thermal analysis of the material showed no indication of thermal relaxation of the glassy structure as well as internal stresses for a sample which was annealed for 30 minutes at a temperature of about 172K below the glass transition. This conclusion is consistent with the outcomes of researches carried out by [26] and [33]. The authors compared Zr based alloys consisting of the same elements but different ratios. The system of $Zr_{60}Cu_{30}Al_{10}$ exhibited no effect of the annealing treatment on several mechanical properties such as tensile strength, Vickers hardness, fatigue

strength, and relaxation induced embrittlement. Only the Charpy impact value was found to increase due to annealing. The experiments were performed below the glass transition temperature in a temperature range of 75K with annealing times between several seconds and about one week. It is possible that the low cooling rate during sample production leaves the temperature of the specimen, especially in its center, elevated for longer time which then leads to structural relaxation, fed by its own heat reservoir. We suggest that in addition, a dense structure of Zr based metallic glasses causes less effect of thermal treatment on the internal structure.
After the evaluation of thermal analysis we find a good agreement between the activation energies of the glass transition calculated by Kissinger's method and the method of Moyahen. Mehta et. al. found that the structural relaxation phenomena during the glass transition can be described by crystallisation kinetics in several calcogenic metallic glasses. The author attributed this phenomenon to a pre-crystallisation process, related to the glass transition, within the material.[34] We assume that this argument is also valid for our Zr based metallic glass and would explain the findings presented here.

## 2.3 Surface Preparation

The most important task of the surface preparation is to obtain surfaces which reflect the actual properties of the substrates as well as the ones of the oxide layers growing thereon. At the same time the preparations must provide a topography which is smooth enough to be investigated by a scanning tip of an Atomic Force Microscope. In addition, a homogeneous distribution of surface properties is preferred for representative tribological measurements. A chemical and structural change of the surface during the pre-oxidation treatments can not always be prevented. Therefore, a proper documentation of the processing steps as well as cleanest preparations are necessary, so that these can later be correlated with the results obtained by surface sensitive examination methods.

### 2.3.1 Mechanical surface treatment

Grinding and polishing are carried out in several stages. In the case of mechanical grinding and polishing, the material to be removed is cut out of the surface in the form of chips and, to a small extent, removed by adhesive forces. The polishing usually follows the grinding procedure. The process is called grinding if the grains are fixed to the support, whereas it is described as polishing if the grains are loose, and usually are applied as a paste to the surface. The resulting surface roughness is

between 10$\mu$m and 100$\mu$m when grinding roughly, and between 1$\mu$m and 10$\mu$m for fine grinding. The fine grinding stages overlap with polishing stages with respect to the surface quality. A specific roughness, deformations below the surface, and other surface defects remain after these processes. The grain size is always reduced from one step to the next, which reduces the amount of surface defects in each processing step compared to the previous one. The total depth of the disturbed surface layer is formed by the sum of the scratch depth and the depth of deformation.
In order to obtain a high ablation rate and low depth of deformation and lubrication, the polishing agent should be as sharp and hard as possible as well as a rigid bound to the support. Therefore, diamond usually meets the requirements for the preparation of metallic surfaces. Often, polishing agents based on silicon carbide are also suitable, since their grains can split under pressure and thus produce new sharp-edged cutting surfaces. With silicon dioxide in a basic suspension, scratch-free surfaces can also be produced on ductile materials. Also important is the choice of the underlying support. The more elastic the support, the lower the depth of deformation and the roughness. Hard substrates lead to plane, but not always scratch-free surfaces. On the other hand, soft substrates lead to well-polished surfaces, but they can cause edges and reliefs. As support, often metal plates are used, while polishing pads are usually made of cloth. In order to provide cooling and removal of the ablated material, grinding on silicon carbide is usually carried out under running water, which results in a greater deformation depth. Excessive pressure can cause heating or deformation of the surface, and too long polishing times can cause reliefs. The heat production also increases with increasing grinding and polishing speed, hence low speeds are preferred in brittle, easily deformable, or recrystallisation-prone materials.(chapter 1 in [35])
On metallic glasses the dissipated energy because of mechanical stresses due to mechanical surface treatment can cause relaxation and even crystallisation, especially by methods such as sawing, grinding, and polishing. The effect of heat production and high strain-rate deformation during mechanical processing of zirconium based bulk metallic glasses was investigated by Bakkal et. al. [36]. In their experiments, they cut the material in such a way that they activated chipping of the metallic glass. Above a certain cutting speed the chips had undergone a crystallisation and an oxidation of their surfaces. The sample temperature during chipping process was measured with a near infrared spectrometer, so the temperature could be estimated being in a range between 2400K and 2700K. Additionally, the surface finishing may affect the corrosion behavior of the surface of the metallic glass. Gebert et. al. found that on zirconium based metallic glasses, which contained 20at% copper, a surface

finishing with a water-based $SiO_2$ solution leads to a smooth but also to a copper enriched surface consisting of copper enriched island embedded in a natively grown oxide film. This effect was explained by an ease of a copper segregation process on the fine polished surface, due to energetically most favorable surface state. In contrast, a surface finishing with diamond paste resulted in a rougher surface, due to a more coarse-grained particle structure, but no copper enrichment was observed.[37] Ion milling is the erosion of the surface by ionic particle bombardment. While at high incident energies electronic processes, such as excitation, ionisation and charge transfer, tend to dominate, at lower energies mainly elastic interactions occur between projectile ions and target atoms. In this regime an incident ion generates a series of primary and higher-order recoiling atoms. This process is called a collision cascade in which a certain amount of recoiled atoms may leave the material by backscattering through the surface as a result of cascade development. The overall dimensions of a cascade below the surface are characterised by the average pathlength of the ion, which depends on the atomic masses of the interaction partners and on the beam energy. The average number of atoms emitted per incident ion is given by the sputter yield $Y(E,\theta)$, which depends on a material constant $\Lambda$, including a cross section for target atoms colliding with each other at low energies, and the surface binding energy:

$$Y(E,\theta) = \Lambda F_D(E,\theta,0) \tag{2.7}$$

$F_D(E,\theta,0)dx$ is the average energy deposited in a surface layer $(x,dx)$ by an ion impinging with an initial energy $E$ with an angle $\theta$ to the inward surface normal. In case of an isotropic cascade, the mean number of atoms $dY(\vec{r})$ sputtered from an area $d^2\vec{r}$ on the surface is given by

$$dY(\vec{r}) = \Lambda f_D(\vec{r}) d^2\vec{r}, \tag{2.8}$$

where $f_D(\vec{r})$ is the average deposited energy per volume in $\vec{r}$.[38] For amorphous targets $\Lambda$ equals $\frac{\Delta x}{\pi^2 U_0}$, with the average depth of origin of the sputtered atoms $\Delta x$ and the surface binding energy $U_0$. The energy loss along $\Delta x$ was neglected.[39] According to [40] a dependency of the sputtering yield on the incident angle $\theta$ is given by

$$\frac{Y(E,\theta)}{Y(E,\theta=0)} = cos(\theta) exp\left(\frac{a^2 sin^2(\theta)}{2\alpha^2}\right), \tag{2.9}$$

with $a$ representing the average pathlength of impinging ions and $\alpha$ is its longitudinal straggling.

**Grinding, polishing, and ion-milling of surfaces**

The $Zr_{60}Cu_{30}Al_{10}$ samples were cut into square pieces with an edge length of about 2mm by a diamond coated metal disc at low speed and oil supply. The specimens designed for Atomic Force Microscopy measurements were glued to a holding fixture at a temperature of 130°C by means of a synthetic resin which made it possible to grind all specimens from all sides in the most similar way. This was done with a sanding machine and SiC grinding paper with an average grain size of 26$\mu$m under water supply. Subsequently, the specimens were fixed on the holding device in such a way that the surfaces to be examined could first be processed by the grinding machine with fine grained paper of decreasing grain size, at last with an average grain size of 5,5$\mu$m. This was followed by polishing with diamond based polishing pastes as well as polishing suspensions with grains of 1$\mu$m to 250nm. After each change of the abrasive paper or the polishing agent, the specimens were cleaned with ethanol in order not to contaminate the surfaces in the following process. Then, they were examined with a light microscope to identify grinding mistakes. Thereafter, the specimens were removed from the fixture and cleaned in ultrasonic bath first with acetone, then ethanol, to remove all resin residues. This was followed by an ion polishing of all sample surfaces with argon ions at an acceleration voltage of 3kV for 10min in a flat-milling method. The angle of the incident ions was about 80° to the surface normal. In order to protect the ion-polished surfaces from contamination, in particular oxidation, the samples were further transported in an argon-filled glass container together with silica gel. The storage of the samples, if not within ultra-high vacuum, took place in a glove box under a pure nitrogen atmosphere with a water or oxygen content of less than 0,1ppm.

### 2.3.2 Thermal surface treatment and oxidation

Corrosion is the deterioration of materials due to reactions with their environment. A special kind of corrosion is oxidation, in which the material acts as an anode and emits electrons in a physical, chemical or electrochemical reaction.(chapter 8 in [5]) Oxidation depends on a variety of factors and the oxidation mechanism can be quite complex. An oxidation reaction begins with the adsorption of oxygen molecules on the surface and proceeds with the nucleation of oxides forming a thin oxide layer. This is followed by its growth to a thicker scale. In the simplest form the reaction of a metal $M$ with oxygen $O$ takes place according to:

$$M(s) + O_2(g) \rightarrow MO_2(s) \tag{2.10}$$

Thermodynamically, one reason for an oxidation is a greater oxygen potential in the environment than the partial pressure in equilibrium with the oxide, also called the dissociation pressure $p_{O_2}$. If the dependence of the chemical potential on the pressure is negligible, the change of Gibbs free energy $G$ of the oxidation reaction is

$$\Delta G\left(T, p_{O_2}\right) = \Delta G^0\left(T\right) - kT \cdot ln\left(\frac{p_{O_2}}{p_0}\right) \tag{2.11}$$

where $\Delta G^0$ is the free energy of the system at standard pressure $p_0$, and $k$ is the Boltzmann constant. If the Gibbs free energy is less than zero, an oxidation takes place. Depending on the stability of the oxides, their formation is thermodynamically favored under vacuum conditions. In the oxidation of alloys, the different affinity of the alloys to take up oxygen must be taken into account, as well as the differences in concentrations, activities, and diffusion rates of the elements in the alloy.

For the growth of oxide layers oxygen anions or metal ions must diffuse through the initially thin oxide layer. Most of diffusion phenomena in metals are based on thermally activated jump events which are mediated by vacancies within the material and can be described by Fick's laws. According to Fick's first law, the particle flux $J$ is proportional to the concentration gradient $\frac{\partial c}{\partial x}$:

$$J = -D\frac{\partial c}{\partial x} \tag{2.12}$$

$D$ is the diffusion coefficient. Fick's second law forms a relationship between temporal and local concentration differences. In three dimensions it is given by:

$$\frac{dc}{dt} = D\nabla c \tag{2.13}$$

If the formation of more than one oxide is possible, the oxidation kinetics of the different constituents need to be considered. Therefore, the knowledge of the different oxidation rates is important which depend on various factors such as temperature, oxygen pressure, surface preparation, and pre-treatment of the metal.

Oxidation in thin layer regime is usually represented by logarithmic rate laws which are based on the transport of either ions or electrons:

$$x = k \cdot log(t) + A \text{ and } \frac{1}{x} = k' \cdot log(t) + B \tag{2.14}$$

Here $x$ represents the rate of weight, thickness or amount of oxygen, consumed per unit area, or amount of oxygen transformed into oxide. $k$ and $k'$ are rate constants,

$A$ and $B$ are integration constants, and $t$ is the time. If the reaction rate is inversely proportional to the scale thickness, the oxidation occurs with a decreasing oxidation rate, and is described by:

$$\frac{dx}{dt} = \frac{k_p}{x} \text{ resulting in } x^2 = 2k_p t + C \tag{2.15}$$

Here, $k_p$ is called parabolic rate constant and $C$ is a integration constant. Most metals follow this kind of parabolic kinetics at elevated temperatures when the oxide growth is governed by diffusion of ions or electrons through the initially formed oxide scale. During oxidation of certain metals the oxidation rate is independent of the amount of oxide grown before, so that the oxidation remains constant with time. Then, the reaction rate is directly proportional to the time:

$$\frac{dx}{dt} = k_l t \text{ resulting in } x = k_l t + E \tag{2.16}$$

The linear rate constant of the reaction is given by $k_l$, and $E$ is a integration constant. Often, a linear kinetic takes place if surface reactions are the governing factors. It has been found that in reality oxidation kinetics are characterised by a combination of these rules. At low temperatures, for example, the oxidation usually follows first a logarithmic, then a parabolic law. At higher temperatures the oxidation may start linearly, indicating an interface controlled reaction, and turns into the parabolic law of a diffusion controlled oxidation. If the layer cracks during oxidation, a direct access of the metal to oxygen is provided, which results in a fast oxidation reaction. Here, the oxidation kinetics would be represented first by a parabolic, then by a linear behavior. All diffusion based oxidation mechanisms are influenced by defect structures within oxide layer and metal. Defect structures can be found in almost all solids at temperatures above absolute zero. These are point defects like vacancies, interstitials, and impurities or other types of imperfections, such as line defects or surface defects. In addition, there are electronic defects, quasi free electrons and electron holes which may compensate the charge balance due to formation of point defects.(chapter 1 in [41])

**Oxidation treatment by TGA**

For the oxidation treatments the samples were placed in a Thermogravimetric Analyser (TGA) of type Netzsch STA443 Jupiter immediately after the ion polishing and were oxidised in synthetic air, consisting of 80% $N_2$ and 20% $O_2$. The oxidation times were 30min, 60min and 90min, and the oxidation temperatures were 450K, 550K, 650K and 720K. A heating rate of 20Kmin$^{-1}$ was chosen.

The small surfaces of the samples resulted in a small mass gain upon oxidation which prevented any further investigations of oxidation kinetics by TGA. Samples which were oxidised at 650K showed a small increase of mass. After necessary baseline corrections a classification of the oxidation mechanism according to a previously presented oxidation kinetic was not possible.

## 2.4 Preparation results

In this chapter the successful preparation of $Zr_{60}Cu_{30}Al_{10}$ bulk metallic glass and its structural and thermal characterisation was presented. After the optimisation of the production process, the amorphous structures of the alloys could be verified by XRD, and the samples were thermally characterised by DSC. The surfaces were smoothed by mechanical grinding and polishing, followed by ion milling. Finally, the controlled oxidation of surfaces by TGA was performed.
Due to the small sample surfaces the mass gain during oxidation was to low to be detected by TGA. To succeed in such experiments, a grinding of the sample material into powder would be necessary in order to obtain a large ratio of surface area to volume. Since such a treatment certainly would influence the microstructure of the sample material up to crystallisation, such experiments were not carried out.

In the next chapter the surface sensitive XPS method was employed and for more topographical investigations electron microscopy was used. The findings of these observations were correlated to the surface treatments before and after surface oxidation of the metallic glass.

# 3 Surface Characterisation

The tribological investigations presented in this work do not only concern the surface but the entire layer system of the oxidised sample. To understand the interaction between AFM tip and material surface, knowledge about the structure and the chemical composition of the oxide layers is crucial. This chapter is dedicated to the investigation of the surface and near surface regions of the $Zr_{60}Cu_{30}Al_{10}$ bulk metallic glass, and its surface oxide, prepared as described in the previous chapter. Images of the surfaces topography were recorded by Atomic Force Microscopy and Scanning Electron Microscopy. For qualitative estimations of the stoichiometry below the surface Energy Dispersive X-ray analyses were performed. X-ray Photoelectron Spectroscopy measurements provided insights into the cross sections of the oxide layers by means of sequential Argon etching technique. The vertical structures of the layers were examined by crosssectioning Transmission Electron Microscopy after preparation supported by Focused Ion Beam technique.
According to studies presented in [42] and [43], regarding $Cu_{60}Zr_{30}Ti_{10}$ bulk metallic glass, and findings in [44] referring Zr-based metallic glass, oxide layers grown for 30 minutes at 450K, 550K and 650K are expected to exhibit a reasonable variation in thickness to be explored with methods presented in this chapter. In addition, different structural growing mechanisms due to thermal activation are considered.

## 3.1 Microscopic surface examinations

The electron gun of a Scanning Electron Microscope (SEM) operates with an accelerating voltage of about 0,1-30kV. An electromagnetic condenser lens produces a demagnified image of the electron source, which is then projected by the objective lens onto the specimen. The electron beam is deflected by scanning coils into a rectangular raster onto the samples surface. Positively charged detectors collect the emitted electrons from the specimen. The spacial resolution of an SEM is determined by the minimum probe size.
The interaction between impinging electrons and matter include their scattering and the loss of energy. At low kinetic energies the interaction of the electron beam with the nuclei of target atoms is negligible and only interactions with the electrons of the shell have to be considered. The energy loss of incident electrons in matter can be described by the Bethe formula, from which in good approximation their path length $s$ can be derived if the energy range is between 10keV and 100keV:

$$s = \frac{4\pi\epsilon_0^2}{e_0^4} \frac{E_0^2 - E^2}{NZ \cdot ln\left(\sqrt{\frac{e}{2}}\frac{E_0}{J}\right)} \tag{3.1}$$

Here, $e_0$ and $\epsilon_0$ are the elementary electric charge and the dielectric constant of vacuum. $N$ is the number of atoms per volume unit with nuclear charge $Z$. The energy of the impinging electron is given by $E_0$, its residual energy is $E$, and $J$ is the atom's average excitation energy. For cross sectional analysis the penetration depth $x_{e^-}$ of the electrons into the material is of interest and can be estimated with an empirical law:

$$x_{e^-}[\mu m] = \begin{cases} 0{,}090\left(\rho[g/cm^3]\right)^{-0,8}(E_0[keV])^{1,3} \; for \; E_0<10keV \\ 0{,}045\left(\rho[g/cm^3]\right)^{-0,9}(E_0[keV])^{1,7} \; for \; E_0>10keV \end{cases} \tag{3.2}$$

where $\rho$ is the materials mass density. The scattering of incident electrons in the Coulomb field of a nucleus, taking into account the shielding effect of the electron shell, can be described by the corrected Rutherford cross section $q(\vartheta)$:

$$q(\vartheta) = \frac{d\sigma}{d\Omega} = \frac{e_0^4}{(16\pi\epsilon_0)^2}\frac{Z^2}{E^2}\frac{1}{\left[sin^2\frac{\vartheta}{2} + \left(\frac{\vartheta_0}{2}\right)^2\right]^2} \tag{3.3}$$

In this relation $q$ is the differential and $\sigma$ is the integral cross section. The scattering angle is $\vartheta$ and $\Omega$ is the solid angle. The shielding angle $\vartheta_0$ describes the influence of the atoms electron shell on the scattering process. The relation between $q(\vartheta)$ and $Z$ exhibits a higher probability for a backscatter process and therefore a increasing number of backscattered electrons at constant beam current with increasing nuclear mass. This leads to a contrast in backscatter electron imaging. Impinging primary electrons loose most of their energy by excitation and ionisation of target atoms. Secondary electrons, generated by ionisation of near surface atoms, can leave the material by diffusion with energies of up to 20eV. The secondary electron yield per primary electron increases in proportion to $1/cos(\Phi)$, where $\Phi$ is the angle between surface normal and electron beam. This relation provides a correlation between the contrast in a secondary electron image and the surfaces topography. Backscattered primary electrons origin from a region surrounding the incident probe and can be deflected through large angles from the surface by generating additional secondary electrons, especially at sharp edges.

The Energy Dispersive X-ray analysis (EDX) is based on the interaction of the incident electron beam with the specimen which generates X-rays. For cross sectional analysis the range of electrons within $x_{e^-}$ which have enough energy to produce X-rays can be approximated numerically by the Anderson-Hasler equation:

$$x_\gamma[\mu m] = \frac{0,064}{\rho[g/cm^3]}\left[(E_0[keV])^{1,68} - (E_C[keV])^{1,68}\right] \tag{3.4}$$

where $\rho$ is the materials mass density, $E_0$ is the incident electron energy and $E_C$ is the critical ionisation energy of the electronic subshell of the characteristic line.[45] If the X-ray range is larger than the photon mean free path, the volume of X-rays that can be detected is even smaller than $x_\gamma$.[46] Characteristic energy peaks of the elements within that volume can be identified, the concentrations of the elements can be calculated and the bulk composition of the sample can be determined.(chapter 3 in [47])

### 3.1.1 Examination of surface oxide by SEM

Surface examinations in terms of topography, morphology and qualitative chemical composition were performed by a Scanning Electron Microscope of type FEI Quanta 400 FEG ESEM. This device was equipped with an additional backscatter detector and an EDX system of type EDAX Genesis V6.04.
Secondary electron images and backscatter electron images of a not oxidised surface of $Zr_{60}Cu_{30}Al_{10}$ bulk metallic glass are shown in fig. 3.1. As described in the preparation procedures in chapter 2, the as-cast metallic glass was ground, polished and ion milled. The sample was stored under inert gas atmosphere and its surface was exposed to ambient atmosphere only for a few seconds. SEM images show a smooth surface which is sparsely populated by irregularly distributed spherical structures of sizes between 10nm and 50nm. The electron backscatter image indicates a higher average nuclear mass for these structures. The spectrum of EDX analysis presented in c) reveals a higher amount of Cu within the spherical structures compared to other parts of the surface. Electron backscatter images of larger scale exhibit a inhomogeneity of average nuclear mass below the surface. Round regions with diameters of about $1\mu$m and less average nuclear mass are visible in d). These regions appear to be distributed along specific tracks below the surface, as visible on larger scale in e). Scanning electron images and backscatter electron images of surfaces of bulk metallic glass oxidised for 30 minutes are shown in fig. 3.2.

The secondary electron images of the surface treated at 450K exhibits two different structures. One structure appears smooth, the other one is determined by spherical particles with diameters between 10nm and 30nm. The corresponding backscatter electron image shows two regions of different contrast, caused by a difference in the average nuclear mass. By comparing the secondary electron image with the backscatter electron image the smooth areas can be correlated with regions of less average nuclear mass below the surface than the regions below the spherical particles. EDX measurement were performed in both regions with electron energies of 5keV and 10keV. According to estimations, based on equation 3.4, the signal

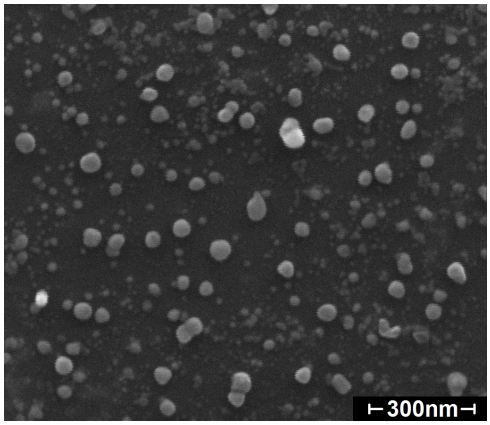


(a) Secondary electron image of the not oxidised surface.

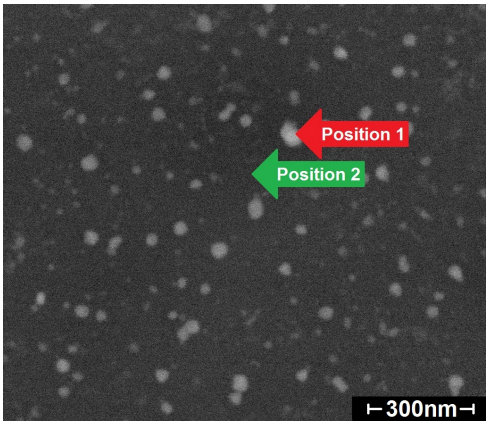


(b) Backscatter electron image of the not oxidised surface.

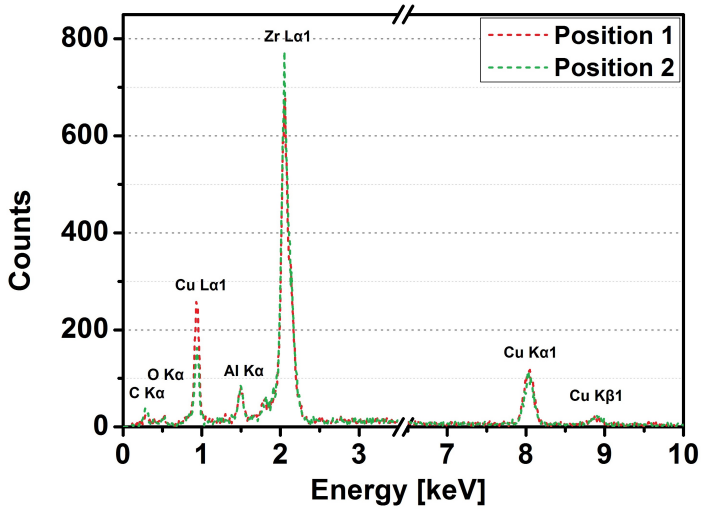


(c) EDX spectrum measured at both marks on the not oxidised surface shown in a) and b).

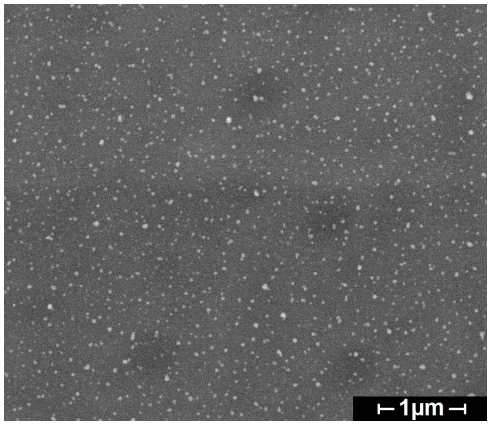


(d) Backscatter electron image of the not oxidised surface.

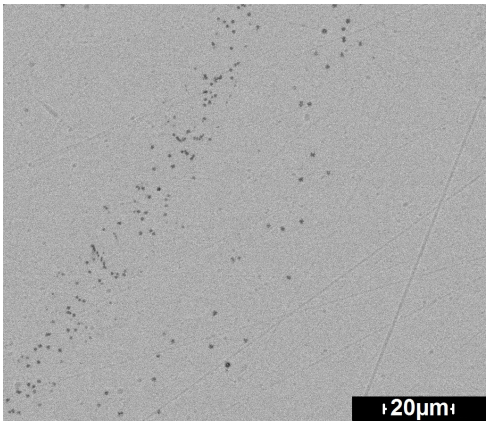


(e) Backscatter electron image of the not oxidised surface.

Figure 3.1: Electron microscopy and EDX analysis on not oxidised surfaces of $Zr_{60}Cu_{30}Al_{10}$ bulk metallic glass. Acceleration voltage was 20kV while imaging.

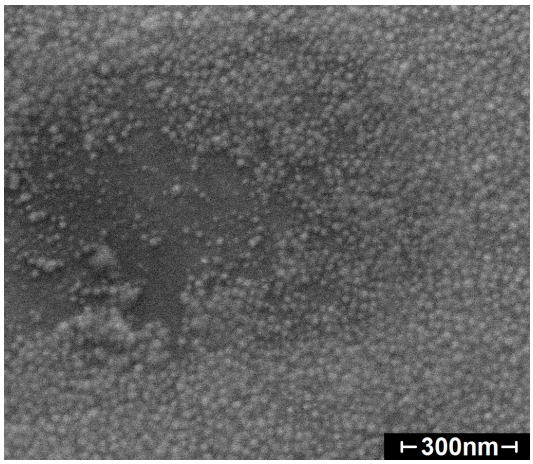


(a) Secondary electron image of surface oxidised at 450K.

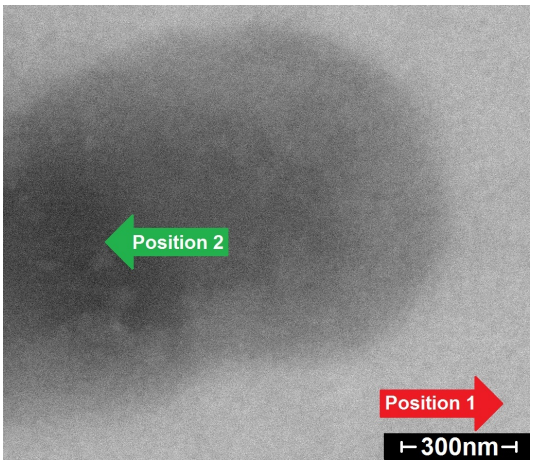


(b) Backscatter electron image of surface oxidised at 450K.

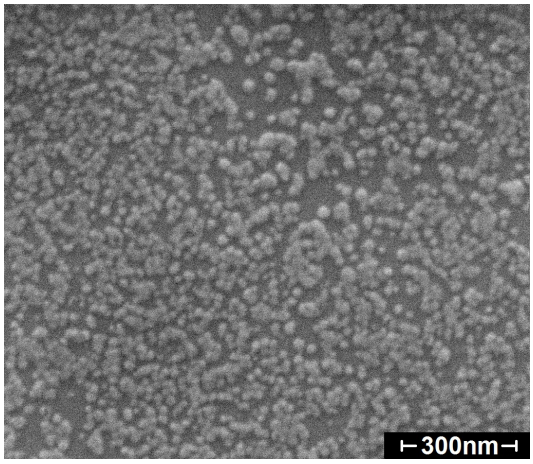


(c) Secondary electron image of surface oxidised at 550K.

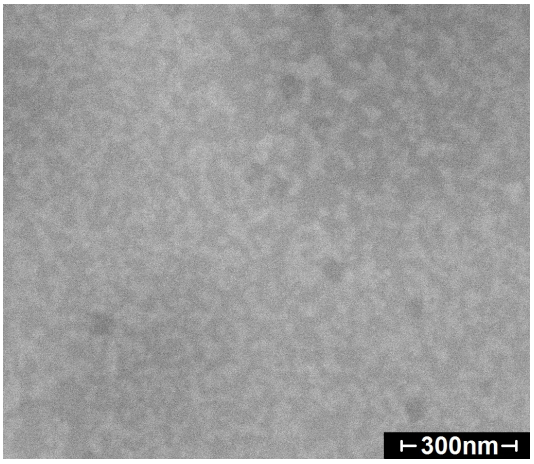


(d) Backscatter electron image of surface oxidised at 550K.

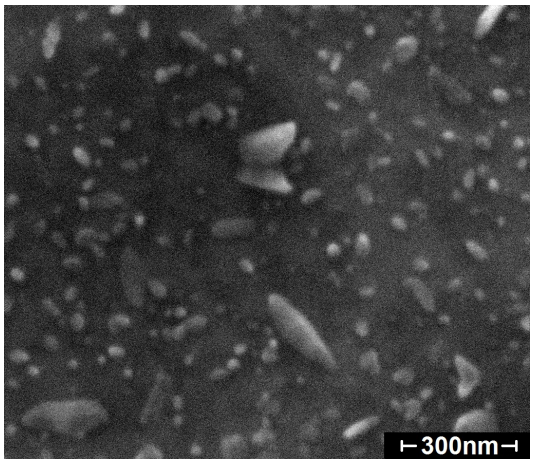


(e) Secondary electron image of surface oxidised at 650K.

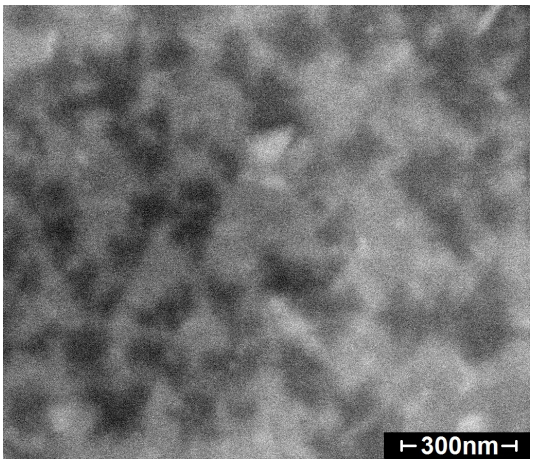


(f) Backscatter electron image of surface oxidised at 650K.

Figure 3.2: Electron microscopy on surfaces of $Zr_{60}Cu_{30}Al_{10}$ bulk metallic glass oxidised for 30 minutes at different temperatures and. Acceleration voltage was 20kV.

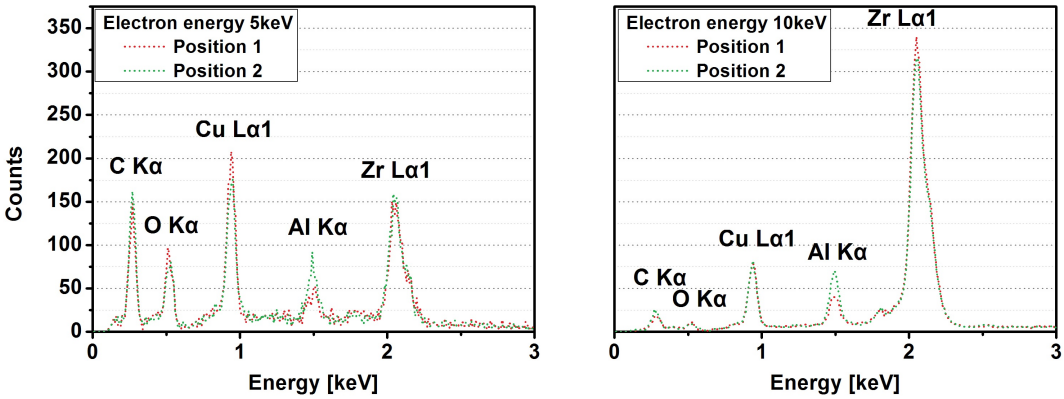


Figure 3.3: Spectra of EDX measurements performed with incident electron energies of 5keV (left) and 10keV (right) on positions marked in fig. 3.2 b) on oxidised surface of $Zr_{60}Cu_{30}Al_{10}$ at 450K for 30 minutes.

depths for 5keV was about 100nm and for 10keV the signal depth was roughly 400nm. All spectra are shown in fig. 3.3. On the smooth areas of the top surface we found a higher Al concentration compared to the regions determined by spherical particles. The concentrations of Cu and O are higher at the top surface, whereby they are lower in the regions of increased Al concentration.

The surface treated at 550K reveals a smooth surface which is covered partially with carpet like structures. According to backscatter electron imaging the material of these structures is of higher average mass than the material of the smooth regions of the surface. In both areas oxygen is detected. On the surface treated at 650K the secondary electron image shows edged structures which cover a small fraction of the surface. The topography in between appears smooth. The backscatter image revealed a heterogeneous distribution of chemical composition of the top surface material. The highest average nuclear mass is related to the edged structures which can be observed in the secondary electron image.
Secondary electron images and backscatter electron images of surfaces of bulk metallic glass oxidised for 60 minutes are shown in fig. 3.4.

The topographical structures of these surfaces are similar to those prepared for 30 minutes under heat treatment. The secondary electron image of the surface treated at a temperature of 450K for 60 minutes showing a smooth surface, partially covered with spherical structures of diameters between roughly 20nm and 90nm. According to the contrast in the backscatter electron image, their average nuclear mass is higher compared to the one of the underlying surface material. On the surface treated at 550K for 60 minutes the degree of coverage of carpet like structures is higher than on the surface treated for 30 minutes at the same temperature. The backscatter

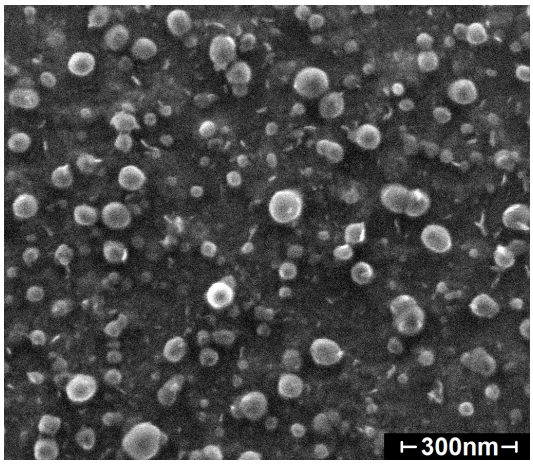


(a) Secondary electron image of surface oxidised at 450K.

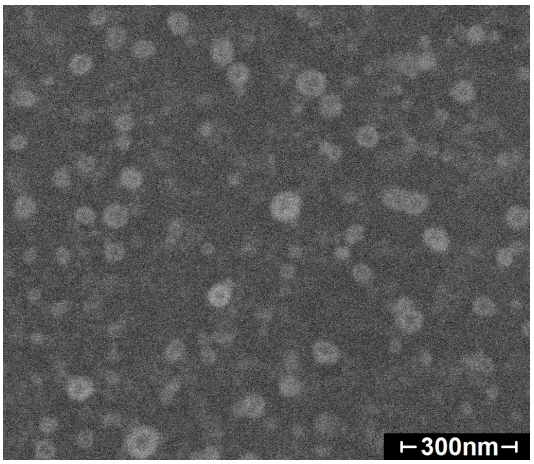


(b) Backscatter electron image of surface oxidised at 450K.

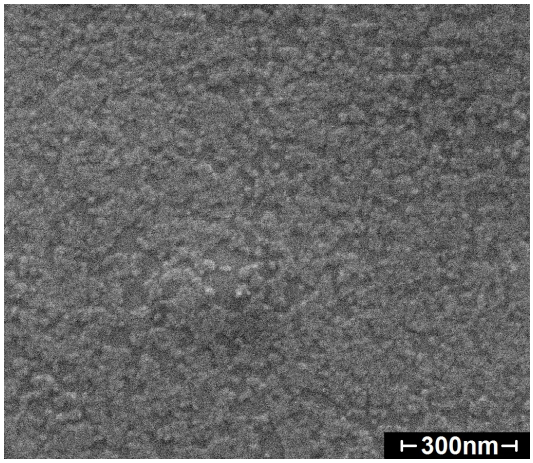


(c) Secondary electron image of surface oxidised at 550K.

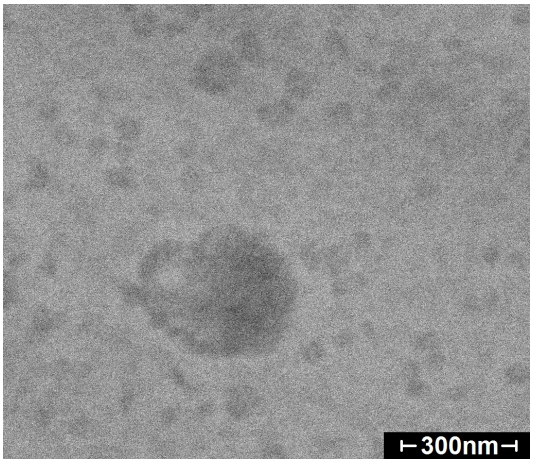


(d) Backscatter electron image of surface oxidised at 550K.

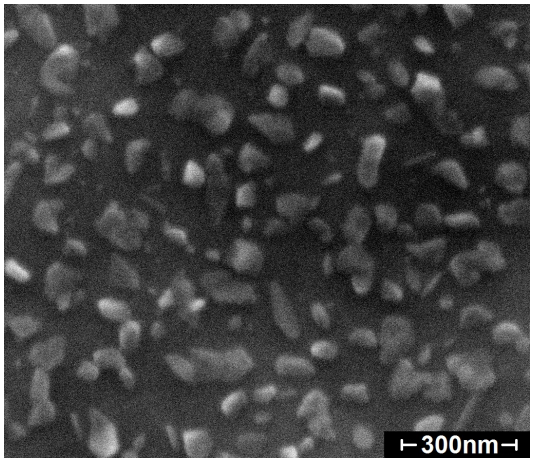


(e) Secondary electron image of surface oxidised at 650K.

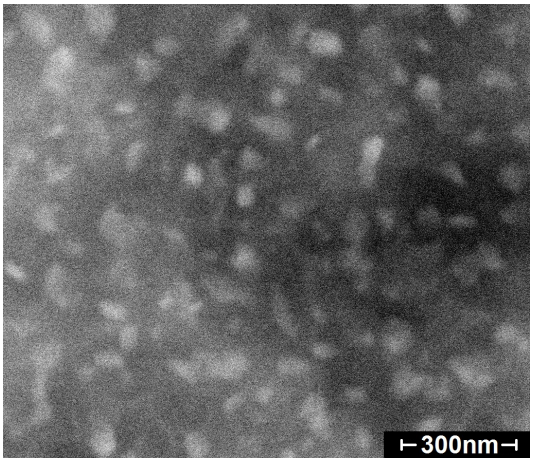


(f) Backscatter electron image of surface oxidised at 650K.

Figure 3.4: Electron microscopy on surfaces of $Zr_{60}Cu_{30}Al_{10}$ bulk metallic glass oxidised for 60 minutes at different temperatures. Acceleration voltage was 20kV.

electron image shows a contrast which suggests an inhomogeneity in the average nuclear masses which can hardly be correlated to the surfaces topography. A region of about 300nm exhibits a lower average nuclear mass than the residual surface material and creates a bulge on the surface below the carpet like structure. The topography of the surface treated at 650K for 60 minutes shows higher degree of coverage of edged structures on the smooth surface compared to the one treated for 30 minutes at a temperature of 650K. According to the contrast in backscatter images the edged structures appear as being of higher average mass density compared to the embedding material.

### 3.1.2 Examination of surface oxide by AFM

The prepared surfaces were imaged with an Atomic Force Microscope in non-contact mode. The instrument used in this work, its working principle and the physical background regarding the interpretation of obtained data are presented in chapter 4. Fig. 3.5 shows the topography of the oxidised surfaces.

The topographies of the surfaces oxidised for 30 minutes at 450K and 550K are defined by spherical structures. In the AFM images the shape of the spheres is convoluted with the one of the scanning tip and reveals average diameters of about 20nm for both temperatures. Higher oxidation times increase the roughness on the surface oxidised at 450K by growing of the spheres to diameters of up to 90nm. The surface oxidised at 550K for 30 minutes exhibits a higher roughness than the surface oxidised at 450K for 30 minutes and shows particles with diameters of about 30nm. On the surface after 60 minutes at 550K no particles can be observed and it appears much smoother than after 30 minutes. The surfaces oxidised at 650K reveal a similar topography after 30 minutes and 60 minutes oxidation time. The surfaces are showing single structures with sizes of several hundred nanometer. The structures appear to be edged and in case of the surface treated for 30 minutes the structure has a height of roughly 50nm.

For comparison, fig. 3.6a presents the topography of a not oxidised surface of bulk metallic glass. The surface appears smooth with exception of single spherical structures with diameters between 5nm and 30nm.
The edged structures found on the surfaces oxidised at 650K suggest a crystallisation either within the oxide or at the interface between metallic glass and oxide layer. The former possibility may be the result of a crystallisation temperature of at least a part of the oxide which is lower than that of the metallic glass at the interface. To investigate the possibility of a surface crystallisation during heat treatment, the metallic glass was held at a temperature of 650K for about 60 minutes in ultra-high

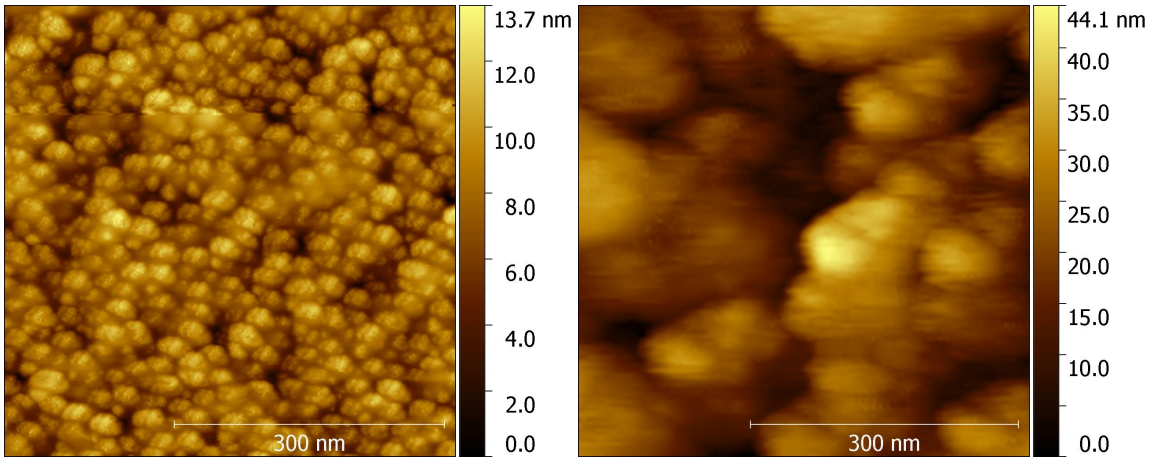


(a) Surface oxidised at 450K for 30 minutes. RMS = 1,84nm.

(b) Surface oxidised at 450K for 60 minutes. RMS = 6,84nm.

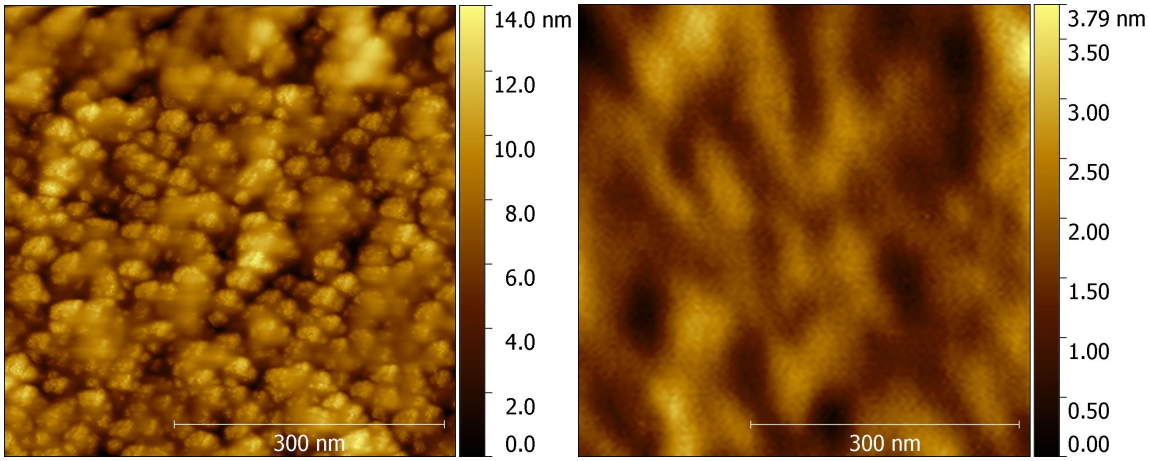


(c) Surface oxidised at 550K for 30 minutes. RMS = 2,18nm.

(d) Surface oxidised at 550K for 60 minutes. RMS = 0,88nm.

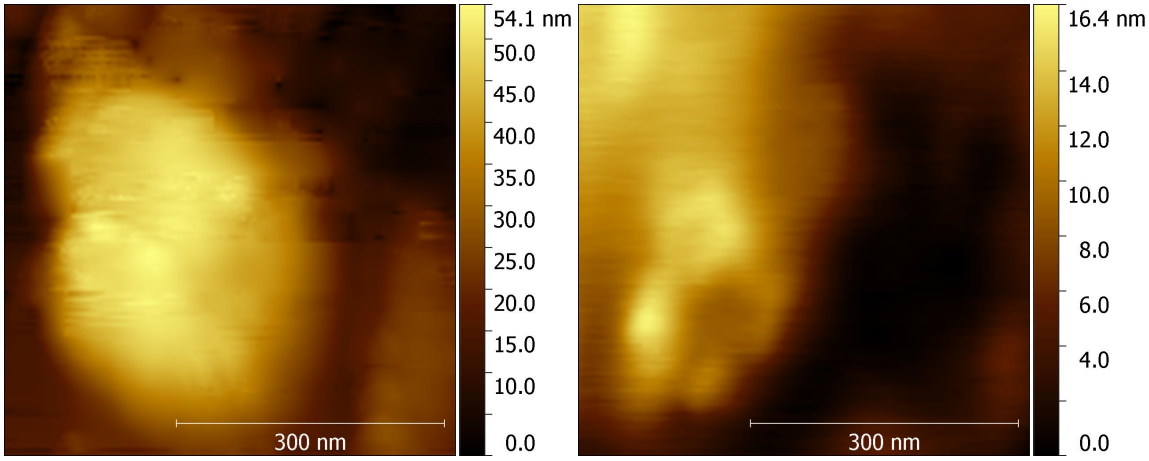


(e) Surface oxidised at 650K for 30 minutes.

(f) Surface oxidised at 650K for 60 minutes.

Figure 3.5: Atomic Force Microscope non-contact imaging on surfaces of $Zr_{60}Cu_{30}Al_{10}$ bulk metallic glass oxidised at different temperatures and for different times.

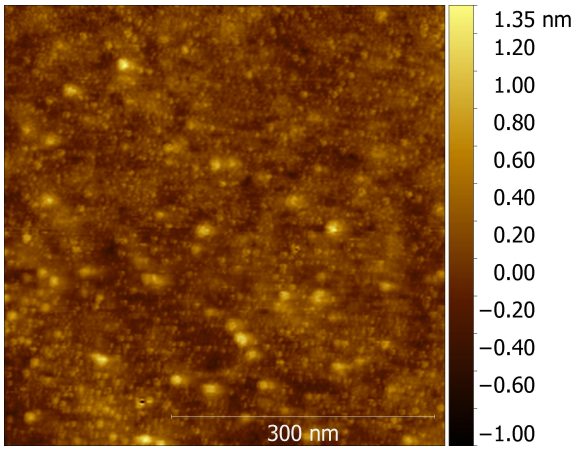


(a) Surface not oxidised. RMS = 0,19nm.

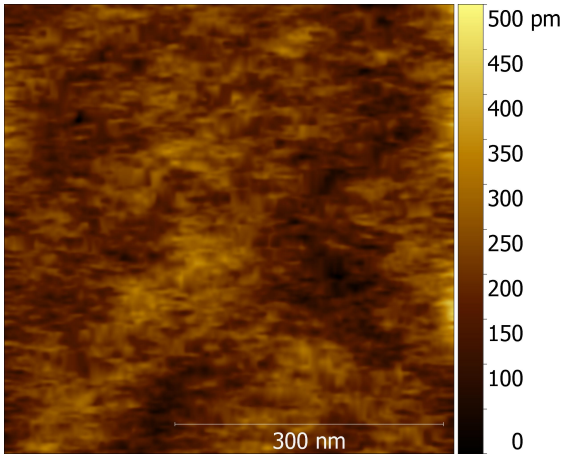


(b) Surface after $Ar^+$ sputter treatment and before heating treatment. RMS = 0,05nm.

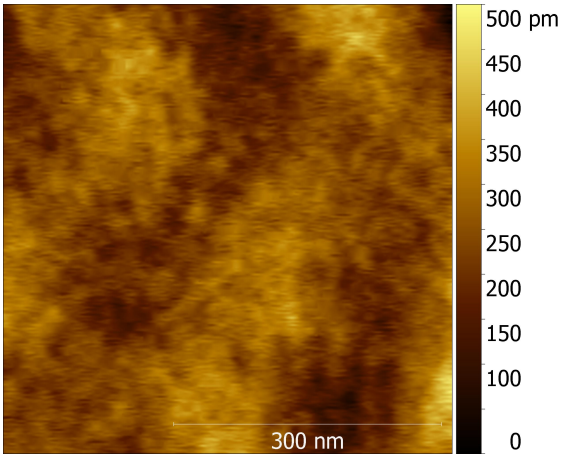


(c) Surface after $Ar^+$ sputter treatment and heating treatment. RMS = 0,06nm.

Figure 3.6: Not oxidised surface of $Zr_{60}Cu_{30}Al_{10}$ (surface in contact with ambient atmosphere for a few seconds) and $Ar^+$ sputtered surfaces of bulk metallic glass before and after heating treatment in ultra-high vacuum at a temperature of 650K for about 60 minutes.

vacuum. The experiment was performed in ultra-high vacuum to prevent any oxidation. After annealing the surface was subsequently imaged by AFM in non-contact mode. No significant change of topography was observed after heat treatment (fig. 3.6b and c). It is unclear if a crystallisation within the oxide or at the interface between metallic glass and oxide layer took place, possibly due to oxidation induced crystallisation.

### 3.1.3 Discussion of analyses

The surface topography depends strongly on the type of heat treatment. At an oxidation temperature of 450K, the surface is covered by spherical structures which are less likely to be found on the not oxidised surface, only exposed to ambient atmosphere for a few seconds. This structure could be assigned to the Cu-enriched areas of the surface in the SEM image of fig. 3.2a. Cu appears to segregate due to oxidation and mainly contributes to the composition of the top layer of the oxide by forming spherical particles. After oxidation at 550K, the coverage seems to be reduced due to accumulation to a more carpet-like structure. The surface exposed below these structures is apparently smooth. On the surfaces oxidised at 450K, on the phases with higher Al concentration, the spherical structures are less in diameter than on the surrounding surface which is indicating for a obstruction of Cu segregation within these regions.
In their work Tam et.al. [48] analysed the composition and the morphology of surfaces of $Cu_{60}Zr_{30}Ti_{10}$ bulk metallic glass after heat treatment in oxygen atmosphere. After oxidation for one minute they observed uniformly distributed particles on the surface. After ten minutes the particles were of larger size than after one minute of treatment and were assumed to be either $ZrO_2$ or Cu agglomerates. While the structure of CuO is described as being whisker like shaped in [49], the morphology of $Cu_2O$ is dominated by particles of diameters between 50nm and 100nm if oxidised in air for 10 minutes at 473K as reported in [50]. After further 110 minutes of oxidation treatment the structure remains unchanged. Regarding the morphology, these results are in agreement with our findings. According to EDX analysis on the surfaces which are not oxidised at elevated temperatures but were in contact to ambient atmosphere for several seconds, the spherical structures, observed on the not oxidised surface, revealed an increased Cu concentration. On the surface oxidised at 450K for 30 minutes, which was mostly covered by spherical particles, EDX analysis revealed a higher concentration of Cu at the top surface than in the bulk material. Thus, we conclude that the particles on the not oxidised surface and on the surface oxidised at 450K consist mainly of Cu.

For further investigations of the structure and elemental composition of the oxide layers cross sections, surfaces prepared by a heat treatment for 60 minutes were excluded, since they tend to form topographies, to rough for tribological examinations by AFM.

## 3.2 Depth analysis of surface oxide layers

In a Transmission Electron Microscope (TEM) the acceleration voltage for the electrons is usually between 100kV and 200kV. The electron source is magnified by two condenser lenses to provide a uniform illumination of the specimen over the area of interest. The objective lens determines the obtainable resolution. After the specimen is transmitted by the electron beam, the final image is projected onto a screen through several projection lenses. Defocussing of the objective lens gives phase contrast through interference between adjacent parts of the wave due to Fresnel diffraction. An aperture at the level of the back focal plane of the objective lens removes some fraction of the diffracted electrons from the image which supports reasonable contrast in TEM images. If only the not scattered electrons are permitted to pass through a small aperture centred about the optical axis, a bright field image is formed. A dark-field image may be recorded if the incident illumination is tilted, so that one of the diffracted beams is aligned along the optical axis and passes the objective aperture.
Electrons, incident on a thin sample, generate diffraction patterns on the back focal plane of the objective lens. Corresponding to Bragg diffraction, crystalline materials show sharp spots from which the degree of crystallinity, the orientation and the crystal structure can be deduced. An amorphous material shows broad rings in its diffraction pattern from which the most probable interatomic spacings can be determined.
A surface sensitive analysis method is provided by X-ray Photoelectron Spectroscopy (XPS). XPS involves the irradiation of the sample by X-rays of known energy $h\nu$. Owing to the photoelectric effect single core electrons of binding energy $E_b < h\nu$ are ejected whose kinetic energy $E_k$ is measured by a spectrometer and is given by

$$E_k = h\nu – E_b - \Phi_{sp} \tag{3.5}$$

where $\Phi_{sp}$ is the spectrometer work function which is a combination of the sample work function and the work function of the analyser. The measurement of the kinetic energy of the electrons provides information about their binding energy. For electron energies from 100eV to 1200eV the inelastic free path $\lambda_m$ is 0,5nm to 2,0nm

within the sample. The actual escape depth $\lambda$ of the photoelectrons depends on the angle $\theta$ of emission to the surface normal such that $\lambda = \lambda_m cos(\theta)$. Assuming a constant photon flux and fixed geometry, for a homogeneous sample the number of photoelectrons per second in a given energy peak is

$$I = KN\sigma\lambda_m AT \tag{3.6}$$

Here, $K$ is a constant, $N$ is the number of atoms per $cm^3$, $\sigma$ is the photoionisation cross section for the element, $A$ is the area of the sample from which the photoelectrons emanate and $T$ is the analyser transmission function. Spin-orbit coupling, result of an unpaired electron in a degenerate orbital, causes a splitting of the corresponding peak in the spectrum. Examples for other possible characteristic effects are chemical shifts, X-ray line satellites, and plasmon loss lines. Therefore, in addition to the binding energy, a XP spectrum provides further information about the specimen's elements and their electronic configuration. The main components of a XPS system are a X-ray source, an electron analyser and an electron detector, all maintained under ultra-high vacuum. The electron analyser separates the photoelectrons according to their energy. After reaching a electron multiplier, the electron signal is finally processed by a rate-meter.(chapter 7 in [47])

### 3.2.1 Depth analysis of surface oxide by TEM

The inner structure of the oxide was explored by a TEM of type JEOL JEM-2100(HR) $LaB_6$. For imaging the cross sections of a layer, a lamella was prepared which was cut from the surface, oxidised at 450K for 30 minutes, by focused ion beam technique. A part of the oxidised surface was coated with platinum, first by an electron beam, and after this by using a gallium ion beam. Subsequently, the selected area was cut out vertically by the ion beam and then was lifted and moved away using a micro-manipulator. The device used for these preparations was a FEI Versa 3D FIB. The lamella then was attached to a TEM holder and thinned with an ion beam and nano-milling technique. The cross section of a sample surface oxidised at 450K for 30 minutes can be seen in Fig. 3.7.

In a) the transition from the metallic glass to the oxide layer is clearly visible by its higher electron transmission. The thickness of the layer is approximately 16nm. The oxide appears as a homogeneous and amorphous material system. Diffraction patterns show an amorphous structure in the region of the metallic glass close to the surface. Within the oxide layer, there are some minor maxima in the diffraction pattern but no clearly recognisable crystal structures.

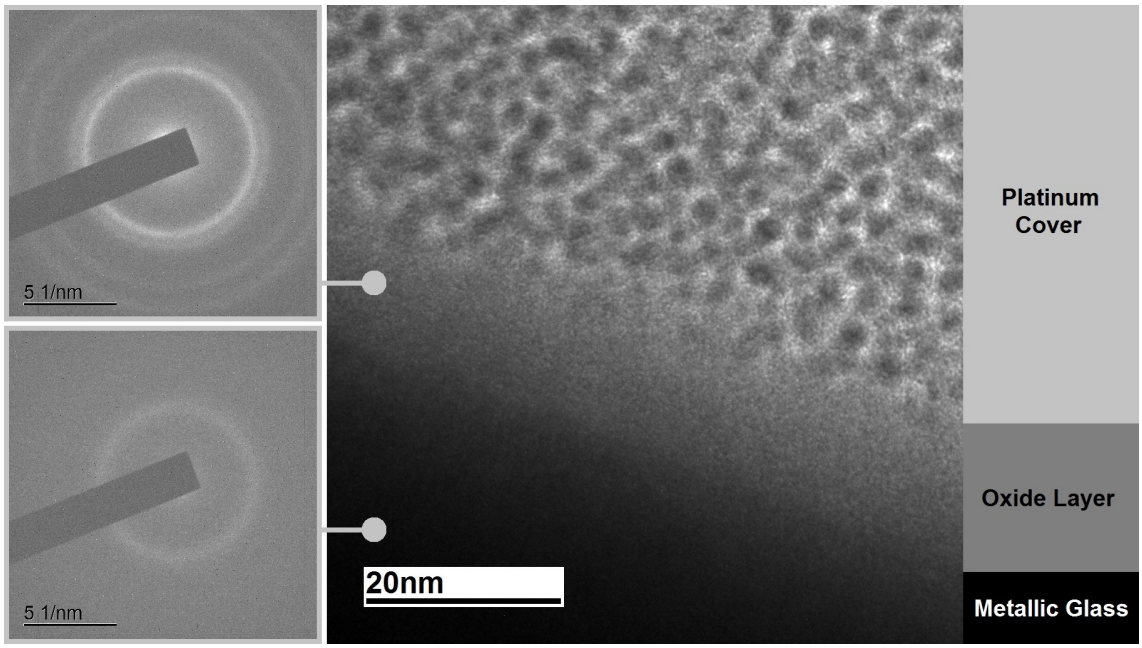


(a) Cross sectional TEM image of the oxide layer and underlying metallic glass. Corresponding diffraction patterns are presented on the left.

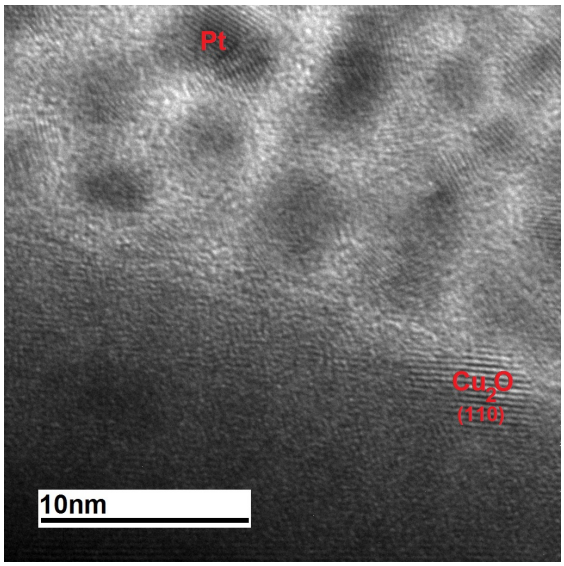


(b) Cross sectional TEM image of crystalline structures corresponding to Pt and $Cu_2O$ (110).

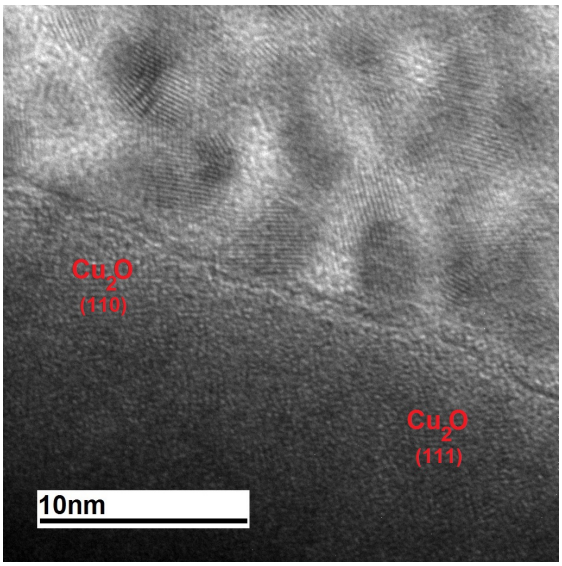


(c) Cross sectional TEM image of crystalline structures corresponding to $Cu_2O$ (110) and $Cu_2O$ (111) at the interface.

Figure 3.7: Cross sectional analysis of an oxide layer prepared at a temperature of 450K for 30 minutes.

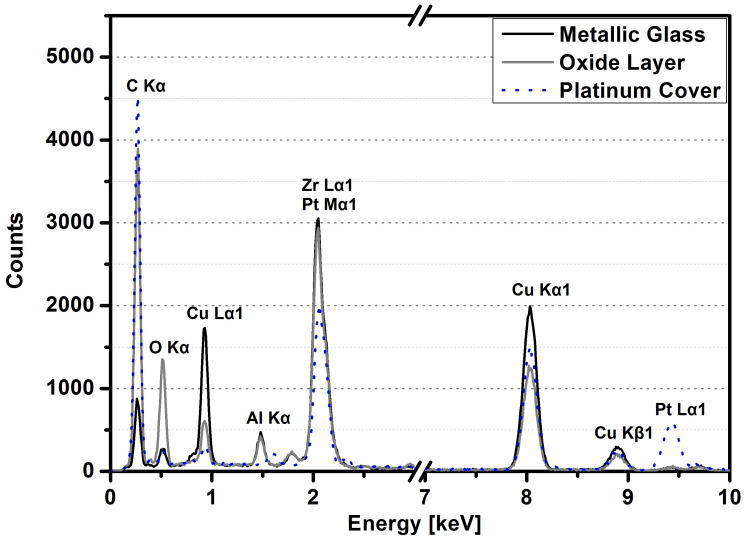


Figure 3.8: EDX spectra obtained from different regions within the layer system shown in fig. 3.7.

Images of higher magnifications b) and c) reveal crystalline structures which are embedded in the amorphous oxide matrix. Some crystalline domains with sizes between 5nm and 10nm could be assigned to $Cu_2O$. Also some other periodic structures are visible which seem to result in Moiré patterns. It is unclear if platinum, which has been implanted in the oxide layer during vapour deposition, is the origin of some of the diffraction phenomena. The platinum layer is recognisable by the granular structure and can be identified by its lattice constant above the oxide layer. The formation of nanocrystalline platinum is presumably due to the evaporation process. Because of the weak transmission contrast at the interface between oxide layer and platinum layer it can not be clearly determined to what extent the deposition process of platinum on the sample surface has influenced the oxide layer, in particular its thickness.

EDX measurements were performed in the region of metallic glass, at a distance of about 20nm below the transition to the oxide layer and approximately in the middle of oxide layer between the crystalline structures, identified as $Cu_2O$. Another measurement within the platinum was chosen for comparison. The corresponding EDX Spectra in Fig. 3.8 show the variation of elements in the corresponding surface zones. The regions between the $Cu_2O$ appear as being Cu depleted and oxygen enriched, compared to the composition of metallic glass. In the spectra it is not possible to distinguish between the peaks of Zr L$\alpha$1 and Pt M$\alpha$1. Since the sample holder for TEM consists of copper, it is possible that a part of the copper signal is assigned to the holder. This contribution should approximately be the same for all

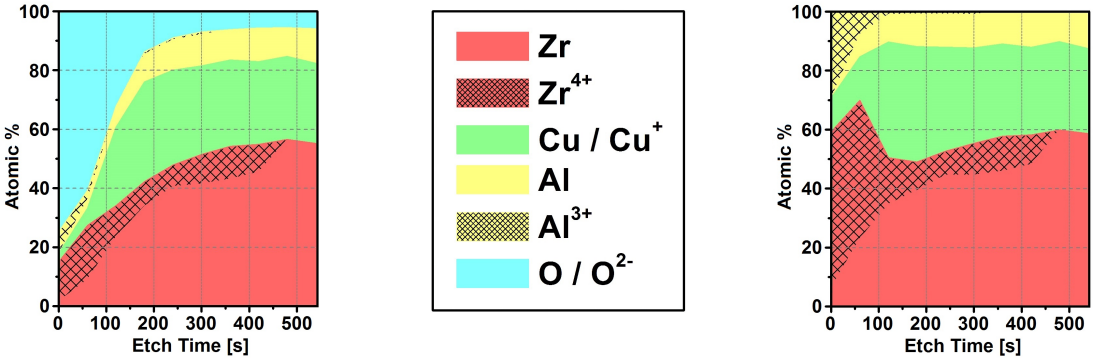


Figure 3.9: XPS depth profiling of $Zr_{60}Cu_{30}Al_{10}$ not oxidised. Plot with oxygen content is on the left and without oxygen content is on the right.

spectra since the different layers are approximately equidistant from the holder.

### 3.2.2 Depth analysis of surface oxide by XPS

X-ray photoelectron spectroscopic depth profiling was performed with a K-alpha XPS device from Thermo Fisher on surfaces oxidised for 30min at temperatures of 450K, 550K and 650K. Additionally, reference samples were analysed which were not oxidised in TGA. After gluing the specimen on a sample holder with carbon tape, they were brought into ultra-high vacuum. Here, an argon ion beam with a beam energy of 2keV abraded the surfaces in vertical direction by means of stepwise etching with periods of 60 seconds for each step. XPS measurements were conducted with an Al-K$\alpha$ X-ray source (Energy 1486,6eV) and the size of the X-ray spot was 400$\mu$m. Fig. 3.9 shows the results for the not oxidised surface. The atomic fraction of zirconium, copper and aluminium in their corresponding oxidation states are plotted against the etch time after which the individual XPS measurements took place. Because of the small difference in the signals of Cu and $Cu_2O$ in XP spectra, both constituents were only scarcely distinguishable. For this reason, the legend shows the same color code for both, Cu and $Cu^+$. Other oxidation states of copper were not found in the XPS signals. For comparison, the graphs are showing the fractions of metals with oxygen (left graph) and without oxygen content (right graph).

According to the left graph of fig. 3.9, oxygen contributes the largest atomic fraction to the top surface region. It is bound to the metals zirconium as $ZrO_2$ and aluminium as $Al_2O_3$ and forms an initial oxide layer which covers the surface. Copper is also detected, but it is unclear which portion is oxidised to $Cu^+$. With increasing depth the signals of oxygen and oxidised metals decay and the material shows more and more pure metallic character. The graphs reveal a constant fraction

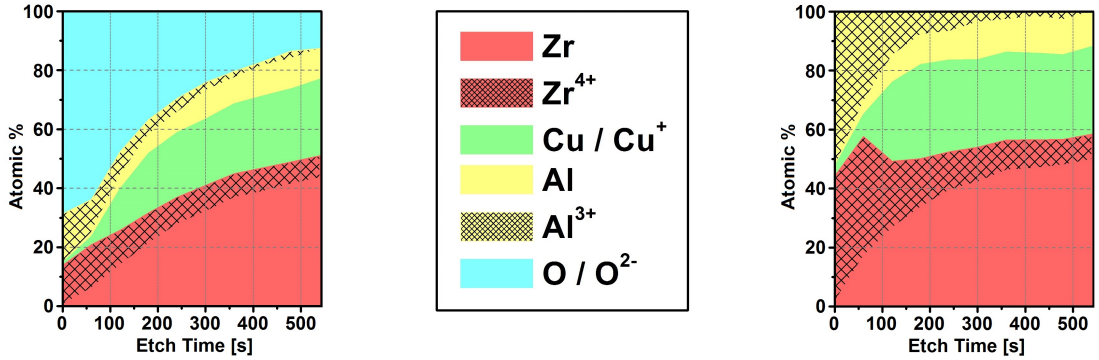


Figure 3.10: XPS depth profiling of $Zr_{60}Cu_{30}Al_{10}$ not oxidised without almost any previous surface treatments. Plot with oxygen content is on the left and without oxygen content is on the right.

of all components at an etch time of about 180s, except $ZrO_2$ which is detected until 480s. The transition between oxide and bulk metallic glass is reached after 180s of etch time, since the concentrations of metals are about the ones expected from the preparation. Only $ZrO_2$ seems to grow deeper into the surface. Noticeably, the atomic concentration of copper is at largest between the metallic glass and the outer oxide layer where its amount is the least.

The atomic concentration of oxygen within the surface layers can either be determined by measurement or it can be obtained due to stoichiometric calculations from the detected amount of oxidised metals. A large difference was found between reduced oxygen according to stoichiometric calculations, and the oxygen detected in measurements. Even after inclusion of eventually $Cu^+$ in the calculations the oxygen concentration cannot be consistently interpreted. Possible reasons for this difference are residual oxygen in the analysis chamber of the XPS device and inaccuracies of both the instrument and the data evaluation. Such inaccuracies could also be the origin of the oxygen detected in the bulk material.

To estimate to which extent the preparation methods influence the surfaces in terms of chemical composition, the effect of different surface treatments, as discussed in chapter 2, on the surfaces of specimen are investigated in the following. The graphs in fig. 3.10 show the distribution of elemental fractions of the surface region within a $Zr_{60}Cu_{30}Al_{10}$ bulk metallic glass which was ground with SiC paper with an average grain size of 26$\mu$m under water supply. The surface was in ambient atmosphere for a few seconds and no further preparations were performed. According to XPS analysis the surface shows a similar profile as the surface which was ground, paste polished and ion milled (compare fig. 3.9). The only difference is a slightly stretched, more continuous, transition from the thin oxide layer to the composition of the bulk ma-

terial. This difference could be an effect of the rough surface which results in non uniform orientations of individual surface areas and with respect to equation 2.9, chapter 2, to a decrease of the overall sputtering yield.
The atomic compositions of oxide layers grown in synthetic air at temperatures of 450K, 550K, and 650K for 30min are shown in fig. 3.11 in dependence of the ion etch time. Graphs a) and b) are showing depth profiles for the oxidation temperatures of 450K and 550K with inclusion of the oxygen content (left) and without (right), whereas graphs c) illustrates the depth profile for an oxidation temperature of 650K with inclusion of the oxygen content (top) and without (bottom). The profiles of the samples which were oxidised at 450K and 550K show a similar chemical composition, although the thickness of the oxide layer grown at higher temperature seems to be larger. The XPS analysis revealed a high atomic concentration of Cu in the top region of both oxidised surfaces. Measurements of the underlying region exhibit a strong depletion of Cu, giving rise to a increasing atomic fraction of $ZrO_2$, $Al_2O_3$, and Al. With increasing time of ion etching, the graphs are showing nearly the same compositions as the ones of the not oxidised samples. There is a slight increase of the Cu fraction again and a continuously decreasing concentration of identifiable oxides after which the relative amount of all constituents stabilises as the bulk of metallic glass is reached. This happens after about 420s on the surface oxidised at 450K, and after 660s on the surface oxidised at 550K.
The surface of samples oxidised at 650K are covered with $ZrO_2$, $Al_2O_3$ and a small amount of Cu. The contents of Al and $Al_2O_3$ decrease continuously with increasing etch time. The relative amount of Cu is constant from the top surface to an etch time of 780s. Then, it increases and finally stabilises at 2060s to the fraction expected for the metallic glass. Until 780s the concentration of $ZrO_2$ also remains the same and makes up the largest fraction of all constituents. It then decreases continuously, and, together with the metallic Zr, it stabilises at about 60at.% after the last etching process. The Zr content increases rapidly during the first etch steps up to about 30at.%. After 400s of etching time it increases slightly for more 10at.% until the end of the plot, whereas it is unclear if it stabilises or if it would replace the $ZrO_2$ completely after further etching steps. This would be expected, since on the surfaces being not oxidised, or treated at lower temperature, no oxides in the bulk of the metallic glass were clearly detected by XPS.

### 3.2.3 Depth analysis of surface oxide by XRD

To study the structural configuration of the individual constituents in the oxide layer, XRD measurements were performed under grazing incidence on an oxidised

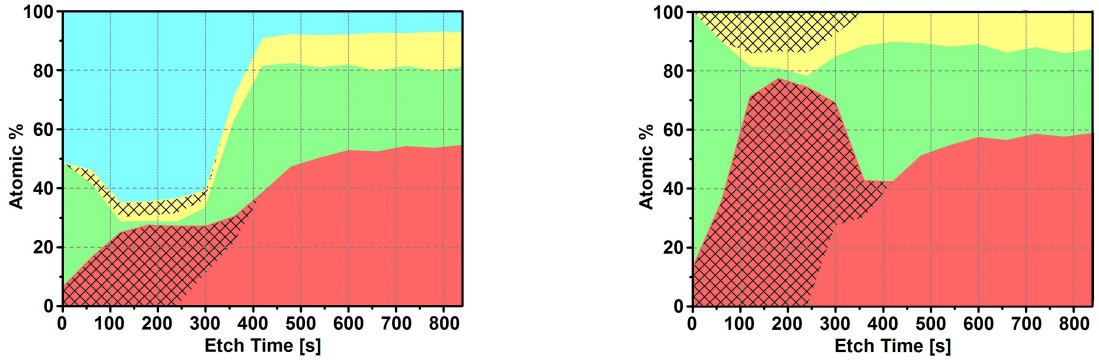


(a) T=450K with oxygen content (left) and without oxygen content (right).

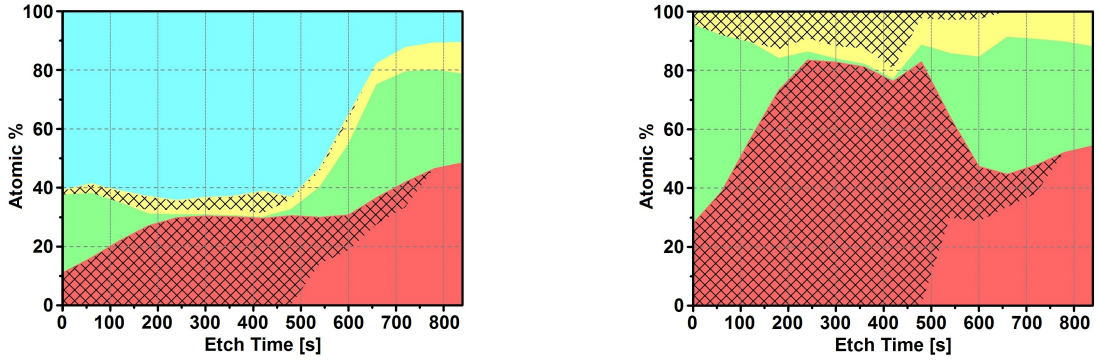


(b) T=550K with oxygen content (left) and without oxygen content (right).

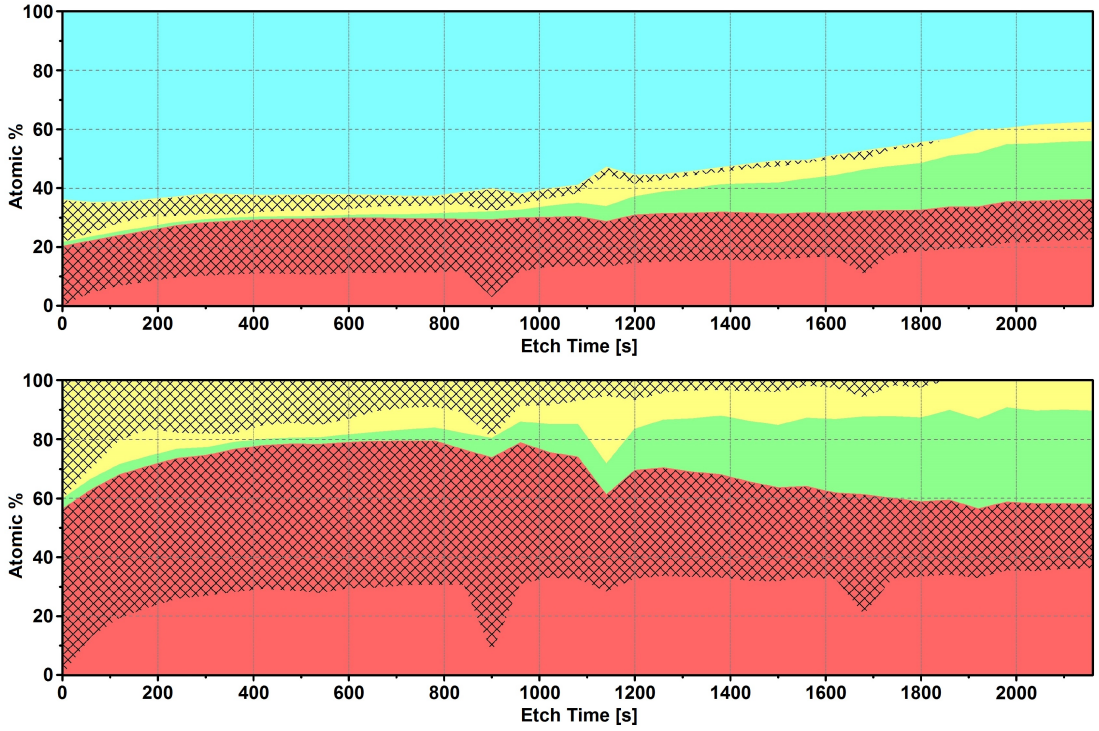


(c) T=650K with oxygen content (top) and without oxygen content (bottom).

Figure 3.11: XPS depth profiling of $Zr_{60}Cu_{30}Al_{10}$ oxidised for 30 minutes at temperature T. Corresponding legend is given in fig. 3.9 and 3.10.

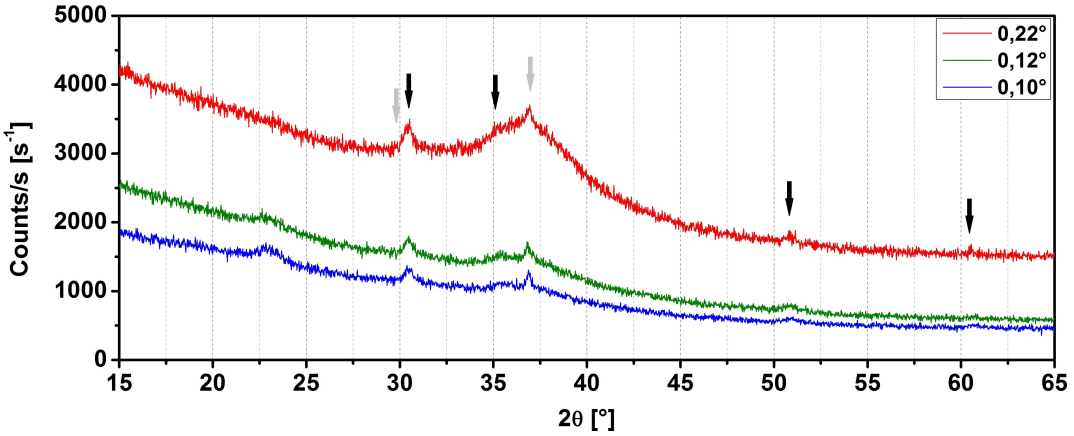


Figure 3.12: XRD-Plots of $Zr_{60}Cu_{30}Al_{10}$ oxidised at 550K for 30min. Refraction peaks correspond to $ZrO_2$ (black arrows) and $Cu_2O$ (grey arrows).

sample surface. By varying the angle of incident X-rays, structural information could be obtained from different depths. For instrumental reasons, the sample surface was exposed to air during the measurement in the XRD device. Since the time of exposure should be as short as possible in order to minimise the reaction time of the surface with the atmosphere, a layer thickness had to be prepared, which generates as many counts per second as possible when the X-ray beam is incident under a grazing angle to the surface plane. In addition, the surface must have a topography that differs as little as possible between surfaces with different oxidation temperature and oxidation time. A continuous measuring time of about one week was estimated for a surface oxidised at 550K for 30 minutes, whereas the thickness of the oxide layer generated at 450K for 30 minutes, which was imaged by TEM, has been estimated to be too small to be measured within an acceptable period.
The measurement was carried out under grazing incidence of the X-ray beam with different angles of 0,10°, 0,12° and 0,22°. The diffracted X-ray beams were detected in steps of 0,02° by counting photons for 240 seconds per step. The area of sample's surface was about (8 X 20)mm, in order to provide a sufficiently large surface for grazing incident XRD. The measurements were carried out with a Philips X'Pert using the CuK($\alpha$) line. Results are shown in fig. 3.12.

The higher the angle, the higher the penetration depth of the incident X-ray beam and the more counts per second were detected. At an angle of incidence of 0,22° the amorphous structure of the bulk metallic glass contributes to the diffraction signal. In all graphs diffraction peaks of cubic $ZrO_2$ (black arrows) and cubic $Cu_2O$ (grey arrows) are observed. The signals for $ZrO_2$ are slightly stronger at an incident angle of 0,22° compared to smaller angles while there is no significant difference in

the signals of $ZrO_2$ for angles of 0,10° and 0,12°. The signals for $Cu_2O$ show no significant dependence on the angle of incidence. Compared to an angle of 0,22° the signal is stronger by a few single counts at smaller angles. According to Scherer method the average crystal size for the cuprides is $(33 \pm 7)$nm and $(13 \pm 1)$nm for the arkelites. The portions of both phases where determined by the Rietveld method. The fraction of the cuprites on all crystalline phases was 18,6at.% and the fraction of arkelites was 81,4at.%. Al could not be detected, which can be explained by its low content both in the bulk of the metallic glass, as well as in the oxide layer.

### 3.2.4 Discussion of analyses

According to XPS measurements, three different regions can be distinguished in oxide layers grown at temperatures of 450K and 550K. An initial surface layer with increased Cu concentration creates the first layer of the oxide, followed by a region of depleted Cu. The top surface layer is characterised by an enrichment of Cu which may take the form of spherical structures at the top surface as observed by SEM and AFM imaging on surface initially oxidised due to contact to ambient atmosphere and oxidised at 450K. Crystalline structures, identified as $Cu_2O$ can be observed in a cross sectional view by TEM. The thickness of oxide layer grown at 450K is about 16nm. The interface between metallic glass and oxide layer can be recognised from the XPS profiles by identifying the metals concentrations of the metallic glass after a certain etch time. By assuming the same sputtering rate, the thickness of the initial oxide layer is about 10nm and oxide layer grown at 550K can be calculated to be roughly 22nm. Findings from XRD measurements under grazing angle are in agreement with the findings regarding the chemical composition. $ZrO_2$ and $Cu_2O$ are distributed within the surface oxide grown at 550K and the interfacial region of metallic glass. The surface treated at a temperature of 650K revealed an oxide layer which is relatively homogeneous in vertical direction and has an estimated thickness of at least 75nm by assuming the same sputtering rate as for surfaces oxidised at 450K and 550K.

A similar distribution of atomic concentrations of copper, as found within oxide layers prepared at 450K and 550K, was reported by Tam et.al. in [48]. Their oxidation treatment of $Cu_{60}Zr_{30}Ti_{10}$ led to a formation of copperoxides in the topmost layer of the surface, while the other constituents were depleted. Below that layer the fraction of all elements was essentially constant and the oxygen was found in high concentration. Within this layer they confirmed the formation of metallic copper and $ZrO_2$ by XRD. This layer was followed by the transition to the metallic glass.

Our observations of nanocrystalline $Cu_2O$ after heat treatments of 450K and 550K

are in agreement with those reported in [51], where nanocrystalline particles of $Cu_2O$ with diameters of about 10nm were identified in an amorphous matrix of $ZrO_2$ in the oxide layer of a $Cu_{47}Zr_{45}Al_8$ bulk metallic glass.

With their studies Stanojevic et. al. demonstrated how atomic partitioning occurs within a bulk metallic glass due to preferential oxidation.[52] As a result the amorphous phase was destabilised by the change in composition which led to partial crystallisation. Since preferential oxidation is to be expected in alloying components with pronounced different electronegativities, we have to consider these effects during oxidation treatments of $Zr_{60}Cu_{30}Al_{10}$. In the course of depth analysis we achieved also insights into the structure and chemical composition of the metallic glass close to the interface to the oxide layer. In the TEM image and the corresponding diffraction pattern in fig. 3.7a we found no indication for crystallisation. We found $ZrO_2$ during XPS measurements, grown into metallic glass, slightly below the interface to the initial oxide (compare fig. 3.9). XRD measurements under grazing incidence on a surface oxidised at 550K for 30 minutes revealed a low significance for a slight increase of $ZrO_2$ with increasing information depth which is challenged by the signal of the amorphous structure (compare fig. 3.12). According to [52] a high thermal stability is characteristic for ternary alloys. The authors found an increased supercooled region after the addition of Sn to a binary alloy consisting of Ni and Nb. We suggest a similar effect on the ternary $Zr_{60}Cu_{30}Al_{10}$ alloy, which is stabilised with respect to equation 2.2 of chapter 2 even after partial oxidation of Zr at the interface. Therefore, we suggest no crystallisation due to preferential oxidation induced atomic partitioning below the oxide layer after heat treatment at 450K for 30 minutes. After oxidation at 550K there is only a weak indication of crystallisation.

## 3.3 Discussion of surface characterisation

In this chapter the topographies as well as the structural and chemical compositions of the surfaces, prepared as presented in chapter 2, were analysed. In the course of the investigations, it was found that the surfaces after heat treatments at a temperature of 650K were too rough to be suitable for friction experiments on the nanometer scale by AFM. The inhomogeneous structure of the surface was caused by irregular crystal growth within the oxide layer.
The results from measurements by TEM, XPS, and XRD collectively provided structural and compositional information about the oxide layers. We will also consider the findings of [48], and [51], and their suggested oxidation kinetics, as presented in

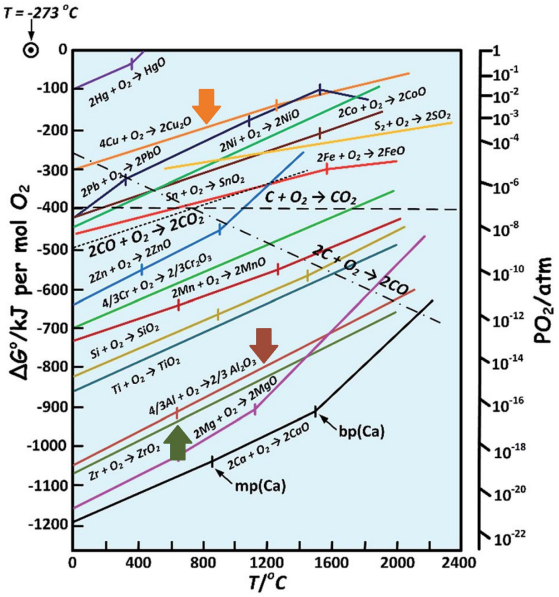


Figure 3.13: Ellingham diagram for the reaction of different elements with oxygen. The curves for Zr, Cu, and Al are indicated by arrows, respectively. From [53].

the following.

At the surface, a phase separation occurred which divides the metallic glass into areas of higher and lower Al concentration. The region of lower concentration forms a matrix in which the regions of higher concentration with sizes of up to 1$\mu$m are embedded. The volume fraction of the matrix appears to be significantly larger than that of the embedded phases.

The affinity for oxidation of a metal as stated in equation 2.11 in chapter 2 is represented by the change of Gibbs free energy which can be plotted in an Ellingham diagram against the temperature. Fig. 3.13 shows an Ellingham diagram for the oxidation of different elements. In the range of oxidation temperatures chosen in this work, the change of Gibbs free energies for the oxidation of Zr to $ZrO_2$ is lowest, followed by the reaction of Al to $Al_2O_3$. This results in preferential oxidations of Zr and Al. Cu is by far the noblest metal of all within the alloy and diffuses through the bulk of the metallic glass separated from the other metals because of preferred mixing of Zr and Al, since the mixing enthalpies between atomic pairs are -44 kJ/mol for Zr-Al, -23 kJ/mol for Cu-Zr and -15 kJ/mol for Cu-Al. As a result, $Cu_2O$ nanoparticles are formed within an amorphous matrix of $ZrO_2$ and $Al_2O_3$. The $Cu_2O$ nanoparticles have sizes between 10nm and 40nm, whereas on the Al rich surface the size is between 5nm and 20nm. This process takes place on the surface of the bulk metallic glass during the exposure to ambient atmosphere for a few seconds. This initial oxide layer has an average thickness of about 10nm and builds

the basis for each further oxidation at elevated temperature in TGA. The metallic glass beneath the initial oxide layer has the expected element concentrations and is amorphous.
From their oxidation experiments with $Zr_{55}Cu_{30}Al_{10}Ni_5$ in dry air, Wang et. al. concluded a simultanously outward diffusion of Zr and an inward diffusion of oxygen. The thermal treatment was performed at a temperature below the glass transition. As oxidation progressed, the diffusion of Zr was suppressed by the ones of Cu and oxygen.[54] The oxidation process of Zr was discussed by Jeurgens et. al. in [55]. The diffusion of Zr through the oxide was found to contribute considerably to the formation of an initially grown layer which was predominantly amorphous.
In our case, the consideration of similar diffusion mechanisms can explain the oxidation at elevated temperature on the basis of the present measurement results, so that the heat treatment at elevated temperature induces the diffusion of metals through the initial oxide. On their way to the top surface Zr and Al oxidise preferentially. At temperatures of 450K $ZrO_2$ stays amorphous. As a result, Cu oxidises at last by forming partially crystalline nanoparticles of $Cu_2O$ at the top surface. The nanoparticles are of similar size as the ones of the initial oxide layer, while they are scarcely covered by $ZrO_2$ and $Al_2O_3$. At 550K diffusion rates are higher compared to 450K and therefore lead to an extension of the overall oxide layer system. After the heat treatment at 450K the overall thickness of the oxide layer is about 16nm, at 550K it is about 22nm. For the initial oxide and the oxide layer after heat treatment at 450K the corresponding formation processes are illustrated in fig. 3.14. Although a small amount of Zr is oxidised within the metallic glass underneath the oxide layer during initial oxidation, no crystallisation of the metallic glass took place.

The preparation techniques presented in chapter 2 confirmed reproducible surfaces of $Zr_{60}Cu_{30}Al_{10}$ bulk metallic glass in terms of topography as well as chemical and structural composition with respect to the characterisation methods applied in this chapter. Final preparatory steps were performed and monitored in ultra-high vacuum. These preparations and methods are presented in chapter 4 followed by the nanotribological examinations.

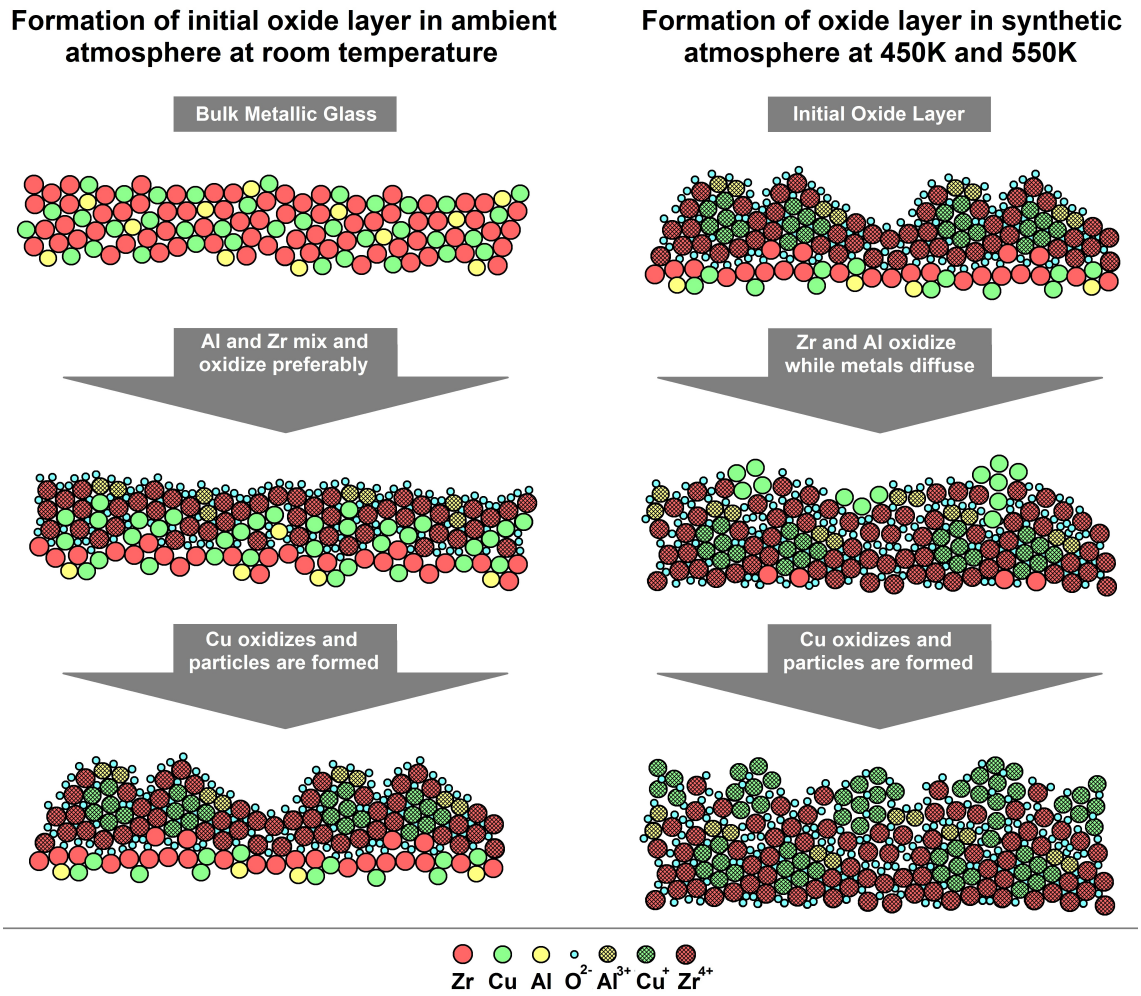


Figure 3.14: Illustration of the oxidation mechanisms of initial oxide on metallic glass under ambient conditions and of the oxide layer at temperatures of 450K and 550K in synthetic atmosphere with a composition of 80% $N_2$ and 20% $O_2$ on top of the initial oxide.

# 4 Nanotribological Measurements

This chapter reports nanotribological investigations on clean and on oxidised surfaces of $Zr_{60}Cu_{30}Al_{10}$ bulk metallic glass. Preparation and characterisation were described in the previous two chapters. Surfaces referred to as oxidised mean those surfaces that have been oxidised for 30 minutes at 450K unless otherwise stated. These surfaces proved to be the most suitable oxidised sample for investigations by AFM, owing to their homogeneous structure and the relatively low roughness. Experiments, results, and derived tribological properties of the oxidised surface are compared with those of the pure surface of the metallic glass.
Experiments with AFM in ultra-high vacuum are presented, which cover a load range from 1nN to above 1$\mu$N and provide insights into the friction and wear of the surfaces.

## 4.1 The ultra-high vacuum system

The generation of a pure atmosphere for the nanotribological investigations as presented in this chapter was of great importance. Therefore, a brief introduction into the fundamentals of vacuum physics is provided in the following.
Ultra-high vacuum (UHV) typically covers a pressure range between $10^{-10}$mbar to $10^{-12}$mbar and is required to prevent reactive surfaces from contamination. This includes any kind of adsorbate such as water and oxygen which might result in the oxidation of metallic surfaces. In UHV the flux $Z$ of residual gas molecules striking the surface is given by the kinetic theory of gases and the Hertz-Knudsen equation:

$$Z = \frac{N_A p}{\sqrt{2\pi MRT}} \tag{4.1}$$

Here, $N_A$ is the Avogadro's number, $M$ is the molar mass, $R$ is the gas constant, $T$ is the absolute temperature, and $p$ is the pressure. The contamination time for a perfectly clean surface to acquire a monolayer of contaminant depends also on the reactivity of the system which can be expressed as the probability that an incident molecule will remain on the surface in some form after collision. Fig. 4.1a shows the dependencies of the contamination time, and the mean free path length on the gas pressure for different reactivities. In order to achieve the UHV regime the vacuum chamber must be free of true and virtual leaks. Virtual leaks arise from gases adsorbed on the internal surfaces. At higher temperatures they desorb faster, hence a bakeout procedure of the chamber is necessary after each venting of the system. The vacuum system is pumped down mainly by turbomolecular pumps and

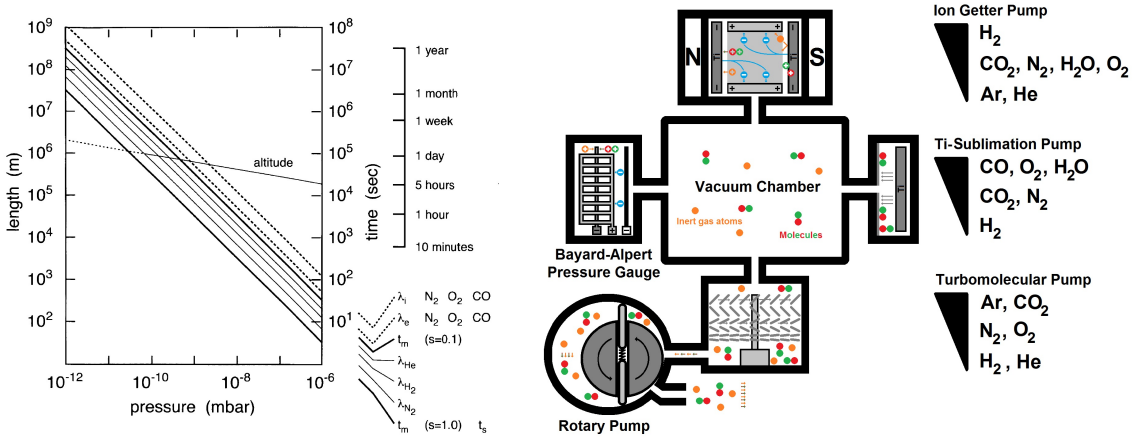


(a) Pressure dependence of mean free path of particles and their collision time.

(b) Illustration of the main components of a vacuum system with their working principle.

Figure 4.1: Properties of vacuum and its technical achievement with the individual pumping efficiencies for different residuals within the vacuum chamber. Illustration based on [56].

ion getter pumps. Titanium sublimation pumps contribute with additional pumping (see illustration in fig. 4.1b. After UHV has been achieved dominant residuals are $H_2$, $H_2O$, CO, $CO_2$ and a variety of hydrocarbons.(chapter 2 in [47])

## 4.2 In-situ preparation of surfaces for tribological investigations

In order to remove the initial oxide from the surface of the metallic glass, it was treated by $Ar^+$ sputtering. The success of surface preparation after sputter treatment was confirmed by chemical analysis, carried out with surface sensitive Auger Electron Spectroscopy (AES).

Auger electrons are the result of a three electron process. At first, an electron of a core shell of a target atom is ejected by an incident electron. The ejected electron leaves behind a vacancy which is rapidly filled by an electron of a shell of higher energy. This process results in an atom of energetically excited state. The atom can loose its excitation either by ejection of an X-ray photon with the corresponding energy or the ejection of another electron. The cross-section of both processes is dependent on the atomic number $Z$ of the excited atom. For elements of low atomic number ($Z < 40$) the emission of electrons, so-called Auger electrons, is favored. Their energy is characteristic of the source atom. In reference to the Fermi level the energy of the Auger electron $E_{Auger}$ is:

$$E_{Auger} = E_1 - E_2 - E_3 - U_{eff} \tag{4.2}$$

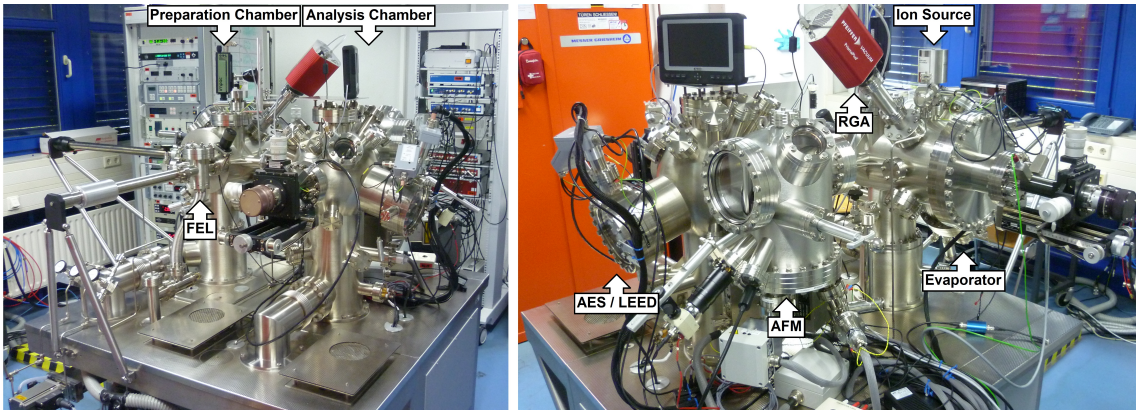


(a) Vacuum chambers for preparation and analysis with instruments including Auger Electron Spectroscope (AES), Low Energy Electron Diffraction (LEED), Residual Gas Analyser (RGA), and Atomic Force Microscope (AFM).

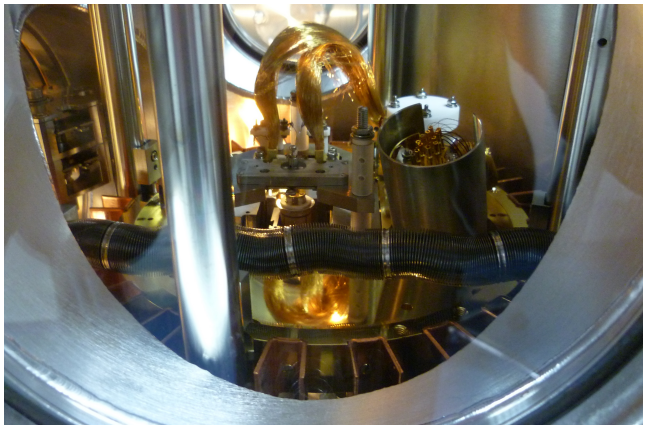

(b) The Atomic Force Microscope.

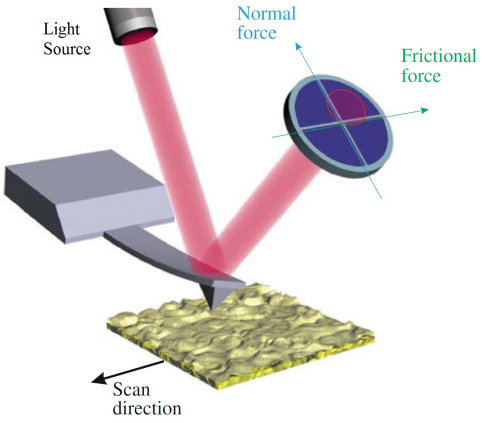


(c) Schematic technical principles of the AFM.

Figure 4.2: Vacuum system of type Multiprobe (manufacturer Omicron) with main instruments including Atomic Force Microscope. Schematics from [57].

Here, $E_1$ is the ionisation energy of the core hole which is filled by an electron from a higher energy level $E_2$. $E_3$ is the energy level the Auger electron is released from and $U_{eff}$ is the additional energy needed to remove an electron from a doubly ionised atom. The energy distribution of Auger electrons is characterised by a decay between 50eV and 100eV which is a result of multiple inelastic collisions of electrons within the solid surface. The Auger peaks are superimposed on this signal while elastically scattered electrons give rise to another peak at the energy of the primary beam. Auger electrons can also be generated by incident X-ray beams or ion beams. In Auger Electron Spectroscopy mostly electron sources are employed which produce electrons with kinetic energies of up to 10keV. A Retarding Field Analyser (RFA) permits the selection of collected electrons regarding their kinetic energy so that only those electrons are counted which pass the retarding field. Because of the inelastic mean free path of Auger electrons, which is between 0,5nm and 2nm, AES is a very surface sensitive analysis method.(chapter 6 in [47])

**Final preparations and examinations of surface purity**

The acceleration voltage was 1kV and the specimen was positioned in such a way, that the ions were incident along its surface normal. The surface was sputtered for about 3 minutes and the pressure within the chamber was approximately $8 \cdot 10^{-6}$mbar, resulting in a beam current of about $25\mu$A. Fig. 4.3a and b showing the effect of sputter treatment on a not oxidised surface, exposed to ambient atmosphere for a few seconds, of $Zr_{60}Cu_{30}Al_{10}$ bulk metallic glass which was prepared as described in Chapter 2.3. Before sputtering, in a) small spherical shaped particles with diameters between 5nm and 30nm and heights between 0,5nm and 1,5nm are observed, which were identified as $Cu_2O$ in the previous chapter. After the sputter procedure no such structures can be found. Instead, round holes were observed with similar concentration as the nanoparticles before ion sputtering. Their diameters are between 20nm and 40nm and their depth are between 50pm and 250pm.
To verify an oxide-free surface Auger Electron Spectroscopy was applied. The AES device was of type Spectaleed (manufacturer Omicron). In fig. 4.3c Auger electron spectra are shown for an oxidised surface and an $Ar^+$ sputtered surface. Zr and C are found on both surfaces. The origin of the carbon signal can be explained by the use a carbon-based epoxy glue with which each sample was attached to the sample holder. In the spectrum obtained on the oxidised surface the oxygen signal indicates the presence of oxides on top of the surface, whereas on the sputtered surface no signal related to oxides was found. Both spectra in fig. 4.3c were recorded with the same experimental parameters.

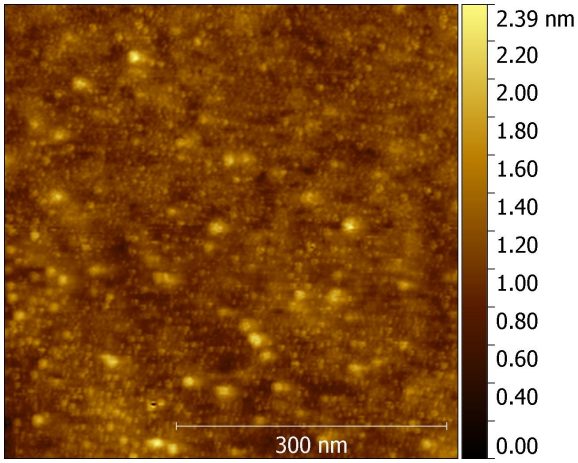


(a) Surface of with initial oxide.

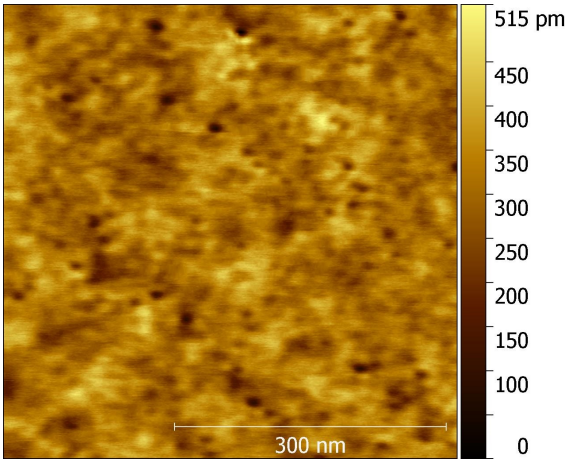


(b) Surface after $Ar^+$ sputtering for 3 minutes.

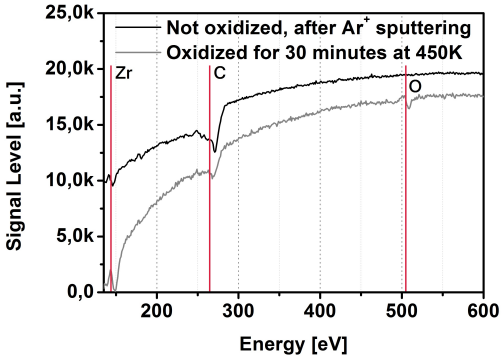


(c) AES spectra, measured on a clean surface and on an oxidised surface. Signals correspond to Zr (M45NVV / M5NVV), C (KVV), and O (KVV).

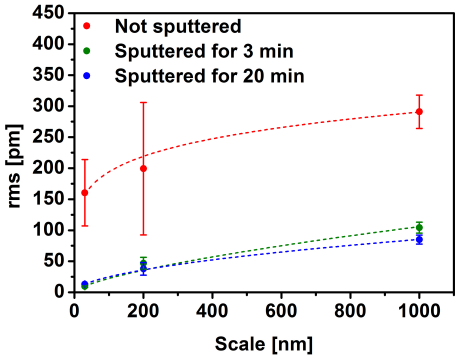


(d) Scale dependent root mean square roughness of surfaces before and after sputtering for different times.

Figure 4.3: Effect of $Ar^+$ sputter treatment on topography and chemical composition of surfaces of $Zr_{60}Cu_{30}Al_{10}$ bulk metallic glass. Sputtering current approximately 25$\mu$A, and beam energy 1keV.

In order to investigate the influence of the argon sputtering process on surface roughness, non-contact images were recorded after different sputtering times at different scan sizes. Each image was recorded at a different place on the surface and for each scan size multiple images were obtained. The results are plotted as root mean square (rms) values against the scan size in Fig. 4.3d. The mean roughness values of the not-sputtered surface and those after 3 minutes and 20 minutes of sputtering time are visible. The not sputtered surface exhibits the highest rms-roughness for all scan sizes and the deviation from the mean is greatest. This can be explained by the inhomogeneous distribution of the spherical particles, which causes a scan frame of small size to lie between the structures with high probability, while at larger scan size the particles contribute irregular to the topography which causes the deviation of roughness to increase. If the scan size is further increased, the deviation from the mean value decreases because the topography reveals a more uniform structure again. Apparently there is no clear difference in the rms values of the surfaces after 3 minutes and after 20 minutes of sputter treatment. The indicated fitting curves were generated according to an empirical power law which relates the surface roughness to the scale as proposed in (chapter 16 in [3]), considering a Gaussian height distribution for each scan size. Therefore, the deviation from this law on the not sputtered surface reflects the deviation from Gaussian height distribution, caused by the influence of oxide particles.

## 4.3 Single asperity friction

In 1985 Binning et. al. developed an Atomic Force Microscope (AFM) to measure forces between the tip of a sensor and a sample surface. Today AFMs are able to measure both normal and friction forces, generally called friction force microscopy (FFM), and have become a popular surface profiler for topographic measurements on micro- and nanoscale. In addition to numerous applications, such as studies of adhesion, wear, and for measurements of elastic and plastic mechanical properties, they are also used for the examination of electric and magnetic properties on the nanoscale.

The AFM uses a piezo tube as actuator to scan the sample. The piezoelectric material expands in one directions and contracts in others, due to an applied electric field. The scanning probe consists of a sharp tip which is attached to a cantilever which is mounted on top of the piezo tube and scans the sample surface. While scanning, the AFM outputs the cantilever's deflection as error signal to the control station. The cantilever deflection is measured using a laser which is deflected onto

a four quadrant photodetector. A feedback loop controls the z position of the piezo, based on the error signal. For small deflections of the cantilever its elastic properties provide a spring-holding of the probe.
In absence of any surface potential the normal resonance frequency of the cantilever beam with thickness $t$ is

$$\omega_m = \frac{\lambda_m^2}{2\sqrt{3}} \frac{t}{l^2} \sqrt{\frac{E}{\rho}} \tag{4.3}$$

with the mass density of the cantilever material $\rho$. The subscript $m$ represents the number of mode, and it is: $\lambda_0 = (0,596864\ldots)\pi, \lambda_1 = (1,494175\ldots)\pi, \lambda_m \to (m+1/2)\pi$. The normal stiffness $k_n$ and the lateral stiffness $k_l$ of a cantilever are given by

$$k_n = \frac{Ewt^3}{4l^3} \text{ and } k_l = \frac{Etw^3}{4l^3} \tag{4.4}$$

with elastic modulus $E$, width $w$, and length $l$. For a wide, thin cantilever ($w >> t$), with an attached tip of height $h$ , the torsional stiffness along the lateral axis $k_{lt}$ can be calculated by

$$k_{lt} = \frac{Gwt^3}{3lh^2} \tag{4.5}$$

where $G = E/2(1+\nu)$ is the shear modulus, expressed with the Poisson's ratio $\nu$. The calibration of the photodetector can be achieved by force-distance curves on a rigid surface where the slope of the curve in the repulsive part is represented by the inverse of sensitivity $S$ of the photodetector. Then, the normal and the torsional force can be determined by

$$F_n = k_n \cdot S \cdot V_n \text{ and } F_t = \frac{3}{2} \cdot k_{lt} \cdot \frac{h}{l} \cdot S \cdot V_l \tag{4.6}$$

by assuming the same sensitivity in both directions. $V_n$ and $V_l$ are the voltages at the photodetector which correspond to the intensity difference of the left and right sets of quadrants of the photodetector. A friction force between the sample and the tip will cause a torsion of the cantilever resulting in an intensity difference which is proportional to the degree of twist angle and to the friction force. From the torsional force $\vec{F_t}$ along the sliding path $\vec{s}$ the dissipated energy during sliding is

$$E_{dis} = \oint \vec{F_t}(\vec{s}) \mathrm{d}\vec{s} \tag{4.7}$$

In addition to thermal and electronic noise, the scanning devices are affected by linear and nonlinear distortions. Linear distortions, such as crosstalk between the motion axes of the piezos, mainly result from imperfections in the machining of the

piezo translators. Whereas the presence of a hysteresis loop in the piezo ceramics results in nonlinear distortions.(chapter 2 in [3])

**The setup and the scope of nanotribological investigations**

Measurements were performed with an Atomic Force Microscope of type VT AFM XA (manufacturer: Omicron). The AFM control software was Nanonis SPM Control Software (Generic 4, 2014, by Specs-Zurich GmbH), and data evaluation was carried out with Gwyddion SPM data visualization and analysis tool (version 2.20), matlab (2010, by MathWorks®) and Excel (2010, by Microsoft®).

In this chapter the fast scan direction is always horizontal and the normal force points against the surface normal. The thickness of the cantilevers were calculated from the free resonance frequency of the first normal mode according to equation 4.3. The normal stiffness and the torsional stiffness were then calculated with the known geometry of the cantilever and the tip length with equation 4.4 and 4.5, respectively. Reciprocal friction force measurements were carried out by determination of the torsional deflection of the cantilever in forward and in backward direction during sliding on the sample surface. The friction force was calculated as the difference between both curves, divided by two. Since torsional deflection and topography are mostly correlated while scanning in contact mode, the surface structure contributes to the error of the torsional deflection in addition to thermal noise. The largest error in the measurements is caused by the calibration of force sensors, which was estimated from the variation of sensitivities of up to 15%. Therefore, we do not show any error for friction forces, deduced from friction loops, obtained from single one dimensional reciprocal sliding. The friction forces, obtained from multiple friction loops due to scanning a two dimensional surface frame, were presented as the average of all calculated friction forces within the scan frame, with the standard deviation as their corresponding statistical error. For the selection of a cantilever, regarding its stiffness, the maximum sensitivity with simultaneous linearity of the cantilever bending in the selected measuring range was aimed. All types of cantilevers used for measurements presented in this work are listed in table 4.1. Fig. 4.4a shows the friction forces for both the clean surfaces of metallic glass and the oxidised surface versus the normal load in a double logarithmic plot. The graph represents the scope of this thesis and gives an overview of the frictional forces whose origins were probed and presented in the following. Full symbols represent the clean surface and empty symbols the oxidised surface. Each cantilever which was used can be identified by the color code. In the load range included by the graph, the friction force on the oxidised surface is on average about four times higher than on the clean surface of

| Type | Tip | Apex Radius | Normal Stiffness | Manufacturer |
|---|---|---|---|---|
| SCD-D10<br><br>SCD-D300 | Single Crystal Diamond, orientation <100> along tip axis | 5-10nm | ≈0,15N/m<br><br>≈40N/m | Artech™ |
| CDT-Cont<br><br>DT-FMR | Diamond Coated, nanoroughness in the 10nm regime | 100-200nm | ≈0,5N/m<br><br>≈6,2N/m | Nanosensors™ |
| PPP-Cont | Highly doped Si | <10nm | ≈0,2N/m | Nanosensors™ |
| Adama-D4 | Diamond | ≈5nm | ≈40N/m | Adama<br><br>Innovations Ltd. |

Table 4.1: Manufacturer's information about cantilevers used for measurements presented in this work. For tip visualisation a test sample with Si spikes (tip curvature radius ≤10nm) of type TGT-1, manufacturer NT-MDT™, was used.

metallic glass, measured with diamond tips. In the transition from the load range of one cantilever to another one almost always discontinuities in the frictional force can be observed and are most probably the result of deviations in the calibrations. Differences in the friction forces for the same type of cantilever can be explained by different tip shapes which lead to different contact properties. Fig.4.4b and c show TEM images of diamond tips before use. According to table 4.1 the apex radius for tips of type SCD is between 5nm and 10nm. The TEM image shows a double tip at the very end of the crystal. One apex has a radius of about 10nm, the other one a radius of about 2nm. Depending on which apex is in contact to the sample it results in a different friction force. The effects of different apex radii on contact properties can be deduced from table 4.2. In addition, depending on the surface roughness, the different aspect ratios of both contact partners result in different contact properties which may influence the torsional deflection of the tip during sliding. The TEM image in fig. 4.4c confirms the diamond coating of the tip. The apex with a estimated radius between 100nm and 200nm reveals a surface roughness, comparable to manufacturers information. In the following, we assume that temperature rises due to frictional heat production at the interface between tip and sample surface during contact-AFM experiments with applied normal forces less than $1\mu$N are neglectable because of the large metallic volume which enables the transport of generated heat away from the contact.

In the first subchapter the effect of chemical and physical properties of contact partners on the friction force is discussed and adhesive wear mechanisms are identified. The second subchapter is dedicated to the influence of surface topography on friction and adhesion.

### 4.3.1 Influence of chemistry and physical properties on friction

A brief introduction into the basic concepts of corresponding contact properties and friction mechanisms is provided at the beginning of each topic.

A tip approaching a surface is influenced by various surface forces. In vacuum the attractive van der Waals forces, mainly based on dipole-dipole interactions, are the dominating long range forces in addition to electrostatic forces. At short range, also covalent or metallic bonding forces can appear as attractive interactions. In contact, these attractive forces are in equilibrium with the short-range hard-core repulsion (compare fig. 4.13b in chapter 4.4). The work of adhesion is the energy change per unit area required to separate two surfaces from contact to an infinite

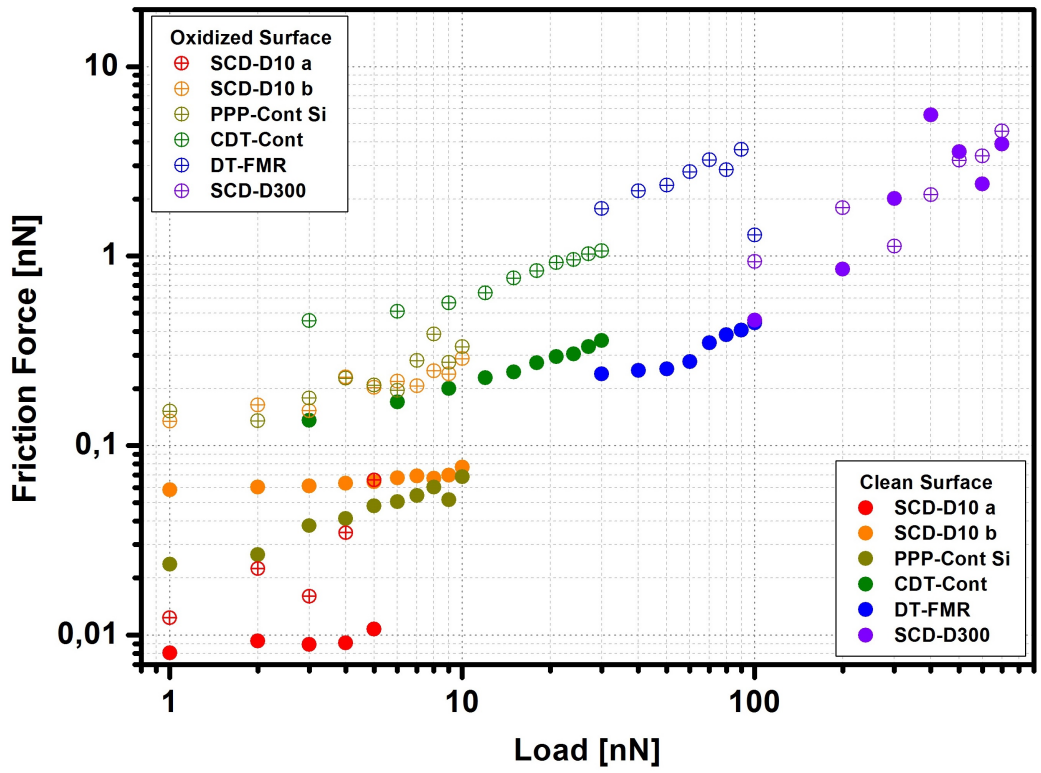


(a) Double-logarithmic plot of friction forces for different loads.

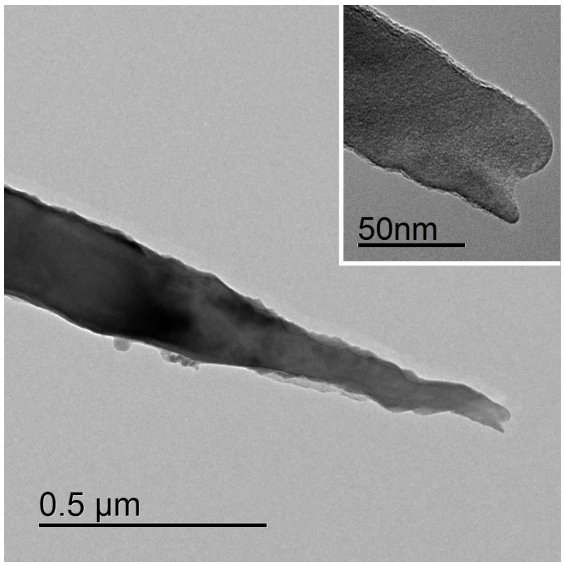


(b) TEM image of a unused tip of type SCD.

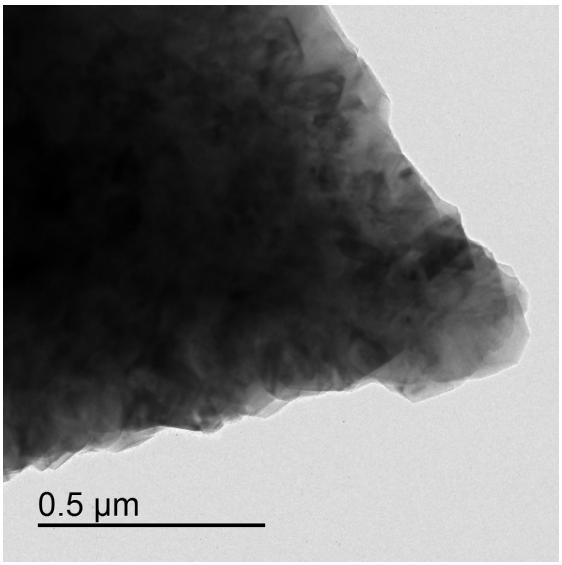


(c) TEM image of a unused tip of type DT.

Figure 4.4: Friction forces on clean surface of metallic glass and oxidised surfaces for different kinds of tips and cantilevers.

| | Hertz | DMT | JKR |
|---|---|---|---|
| $a$ | $\sqrt[3]{\frac{RF}{E_{tot}}}$ | $\sqrt[3]{\frac{R}{E_{tot}}\left(F+2\pi RW\right)}$ | $\sqrt[3]{\frac{R}{E_{tot}}\left(F+3\pi RW+\sqrt{6\pi RWF+\left(3\pi RW\right)^2}\right)}$ |
| $\delta$ | $\frac{a^2}{R}=\left(\frac{F^2}{RE_{tot}^2}\right)^{1/3}$ | $\frac{a^2}{R}=\frac{\left(F+2\pi RW\right)^{2/3}}{\sqrt[3]{RE_{tot}^2}}$ | $\frac{a^2}{R}-\frac{2}{3}\sqrt{\frac{6\pi Wa}{E_{tot}}}$ |
| $F_{ad}$ | 0 | $2\pi RW$ | $\frac{3\pi RW}{2}$ |

Table 4.2: Derivation of contact radius $a$, surface deformation $\delta$, and adhesion Force $F_{ad}$ from different contact theories.

distance in a vacuum.
In case of pure elastic deformation, the relations between contact radius, deformation of the sample, and the adhesion force for a spherical tip, which can be considered as single asperity on a plane surface, are discussed by the contact theories of Hertz, Derjaguin-Müller-Toporov (DMT), and Johnson-Kendall-Roberts (JKR). In the model of Hertz adhesive forces are neglected. The DMT-theory includes adhesion outside, and the JKR-theory considers adhesion inside the contact area. Table 4.2 shows the relations between contact radius $a$, sample deformation $\delta$, and adhesion force $F_{ad}$ to the radius of a spherical tip $R$, the adhesion work per unit area $W$, and the reduced Young's modulus $E_{tot}$ according to

$$\frac{1}{E_{tot}}=\frac{3}{4}\left(\frac{1-\nu_s^2}{E_s}+\frac{1-\nu_t^2}{E_t}\right) \tag{4.8}$$

where $\nu_t$, $E_t$, $\nu_s$ and $E_s$ are the Poisson's ratio and Young's modulus of tip and sample, respectively.

For any punch that can be described as a solid of revolution of a smooth function, the relationship between load and displacement (compare Hertz-contact from table 4.2) is given by

$$F=\alpha\delta^n \tag{4.9}$$

Here, $\alpha$ and $n$ are constants ($n=1$ for flat cylinders, $n=2$ for cones, $n=1,5$ for spheres and paraboloids).[58]

A single asperity sliding on a surface was discussed by Tomlinson. In the one-dimensional Tomlinson model the total potential energy of the system is given by the position-dependent inter-atom potential and the energy which is stored in the spring. If a support moves with a constant velocity $v$ and spring-holds a tip with

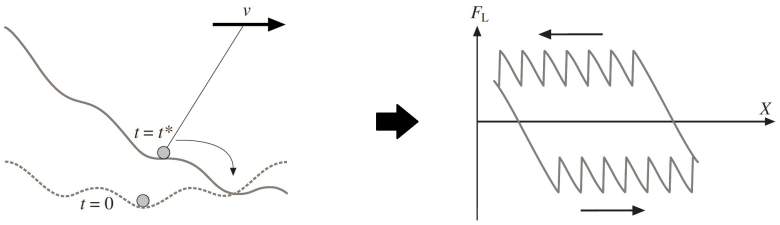


Figure 4.5: Illustration of the stick-slip mechanism according to Tomlinson (left) which results in a sawtooth-shaped lateral deflection (right), based on [3].

an effective torsional spring constant $k$ within a periodic potential, the effective potential can be expressed as

$$E(x,t) = -\frac{V_0}{2} cos\left(\frac{2\pi x}{a}\right) + \frac{1}{2}k\left(vt - x\right)^2 \tag{4.10}$$

The parameter $V_0$ is the amplitude of the periodic potential and $a$ is its periodicity. In this model, which can be extended into two dimensions, the tip resides in a minimum of the effective potential at the time $t = 0$. Due to the motion of support the tip's position becomes unstable and the tip suddenly jumps into the next minimum of the potential at $t = t^*$. This transition is illustrated in fig. 4.5 together with the resulting lateral force $F_L$ as a function of cantilever position $x$.(chapter 10 in [3]) This process is called stick-slip. Energy dissipation in the tip-sample interaction is related to phonon excitation, electronic excitation, and irreversible changes of the surface. According to the Tomlinson mechanism, irreversible jumps, occurring during a sliding process, lead to a dissipative character of friction.(chapter 3 in [2])
Plastic deformation between contact asperities during sliding was considered as another aspect of friction by Bowden and Tabor. They proposed that the friction force $F_f$ is proportional to the real area of contact $A$, and to the shear strength $\tau$ which is the lateral force per unit area necessary to shear the junctions between contact partners. Due to plastic deformation, caused by a normal force $F_n$ which is applied to the surface, the contact asperities are compressed until a yield pressure $p$ is reached at which they are able to support the external load. This results in

$$A = \frac{F_n}{p} \quad \text{and therefore} \quad F_f = \frac{\tau}{p} F_n \tag{4.11}$$

in which $\frac{\tau}{p}$ can be expressed as the coefficient of friction $\mu$. According to Greenwood and Williamson, the proportional relationship between contact area and normal force is also valid for elastic contacts, if asperities, all with the same radius of curvature, and normal distributed heights are in contact with a flat surface.(chapter 10 in [59])

However, computer simulations proposed a slightly sublinear dependence between the contact area and the contact pressure for harmonic height profiles.[60]
Two materials of comparable hardness in sliding contact might form a wear particle in the presence of strong adhesive force as discussed in [61] by Aghababaei et. al.. The authors simulated the plastic deformation of two asperities during collision and found a critical length scale that governs the adhesive wear mechanism. Debris particles, having the size $d$, will form if

$$d > \lambda \frac{G \cdot \Delta w}{\sigma^2} \tag{4.12}$$

with $\lambda$ representing all geometrical factors, the shear modulus $G$, and the shear strength of the junction $\sigma$. The energy associated to newly create free surfaces because of a unit area of crack growth in each sliding body is given by $\Delta w$. If the condition of equation 4.12 is not fulfilled, continual asperity smoothing occurs that eventually leads to cold welding of both surfaces.

**Nanotribological examinations by AFM**
We will demonstrate in the following that for the understanding of the underlying wear mechanisms structural and chemical surface properties are of high influence.

In the previous chapter the analysis of the surface which was exposed to air for a few seconds, revealed a few spherical particles on the surface which were attributed to $Cu_2O$. Most of the surface was covered by a layer consisting mainly of $ZrO_2$ and $Al_2O_3$. To distinguish the tribological effects of the $Cu_2O$ nanoparticles from those of amorphous $ZrO_2$ and $Al_2O_3$, experiments were performed on the clean, the oxidised and the not oxidised surface which was exposed to ambient atmosphere. Additionally to friction experiments, force-distance curves are taken into account to decouple the adhesion force from the friction force. For the measurements a soft cantilever of type SCD-D10 was used. The preload for each force-distance measurement was 3nN. The unloading rate was varied between 0,05nN/s and 1,32nN/s, and the time the tip was in contact to the surface before retracting was varied between 1 second and 5 seconds. The pull-off force revealed no dependence on the unloading rate, or on the time in contact. The graph in fig. 4.6 shows a two dimensional histogram in which the total work of separation $E_{separation}$ is plotted against the maximum pull-off force $F_{pull-off}$.

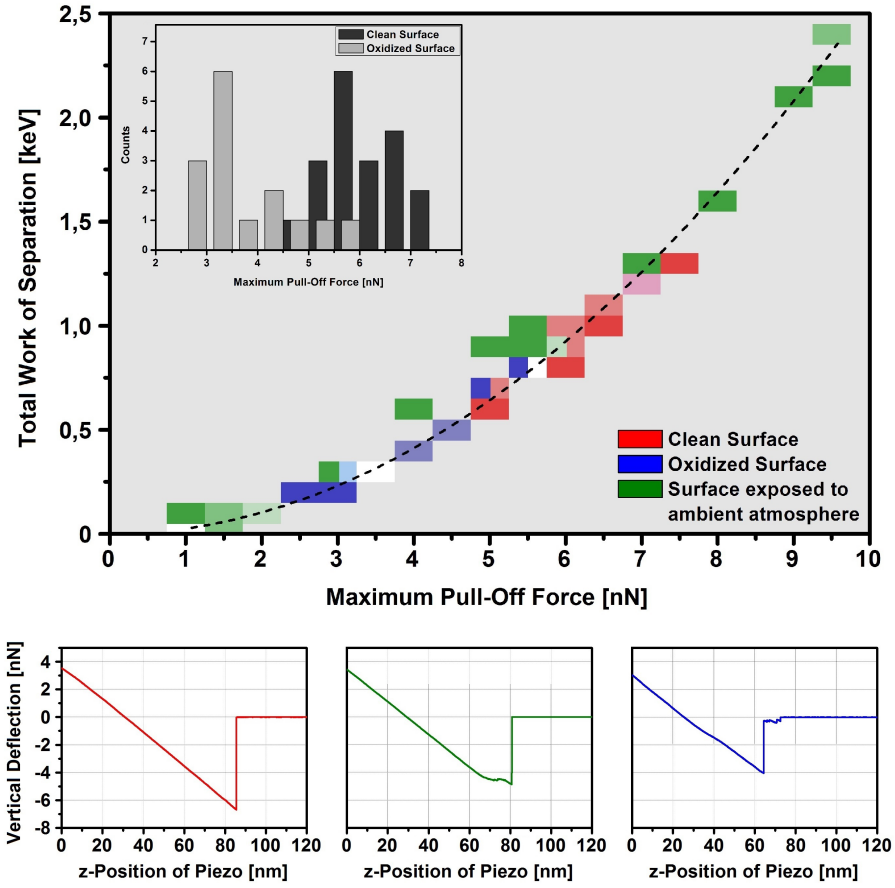


Figure 4.6: Histogram of the total work of separation in dependence of the maximum pull-off force with parabolic fit of data points, indicated by the dashed curve. The brighter the color of a certain field, the more counts were measured within the corresponding interval. The inset shows the histograms of the maximum pull-off force on the oxidised and the clean surface. In the last row of this figure three force-distance curves are shown, measured on each surface. The color code for each surface is given in the graph.

The dashed line represents a parabolic fit of the data according to

$$E_{separation} = \frac{F_{pull-off}^2}{2k_{eff}} \tag{4.13}$$

from which the effective stiffness of the contact was determined as being $k_{eff} = (0,122 \pm 0,001)N/m$ which is in agreement with the normal stiffness of the cantilever. From this we conclude that the contact stiffness between the surfaces of each sample and the tip is several magnitudes higher than the normal stiffness of the cantilever which was about $0,123N/m$. For the surface which was exposed to ambient atmosphere, there are deviations from the fitting curve, especially at pull-off forces between 4nN and 7nN. The corresponding force-distance curves indicate a separation process in which the tip doesn't separate spontaneously from the surface but separates more continuously before the contact finally breaks off completely. We conclude that this process is caused by third-party material between tip and metallic glass. In 20% of all force-distance curves on the oxidised surface ruptures can be identified as additional separations after the separation of the tip from the surface. Each curve of multiple separations shows one to four ruptures with lengths between 1,2nm and 4,9nm and stiffnesses in a range between 0,064N/m and 0,092N/m. Examples of such irregular shaped curves can be seen below the histogram in fig. 4.6. The closer the fields in the histogram are to the parabola, the more often the tip separates from the surface in a single jump, without any rupture. The mean maximum pull-off forces for the clean surface and the oxidised surface were obtained from the histograms by curve fitting with a Gaussian distribution. The adhesion force on the clean surface was $F_{ad,clean} = (6,0 \pm 0,8)nN$ and on the oxidised surface it was $F_{ad,oxidised} = (3,1 \pm 0,3)nN$.

Friction was determined on a square scan frame with side length of 20nm and the scan speed was 39nm/s. The graph of fig. 4.7a shows the friction force against the load for each surface. As can be seen, the graphs representing the clean surface and the oxidised surface show a linear dependence on the load. The initial oxide on the surface exposed to ambient atmosphere for a few seconds leads to a higher friction force compared to the one obtained on the metallic glass. The data points mostly exhibit less friction than on the oxidised surface. The friction values are subject to larger variation, which can be explained by structural and chemical inhomogeneities of the initial surface oxide. Judging by its shape, the graph assigned to the surface exposed to ambient atmosphere appears to represent a transition between the one of pure metallic glass and the oxidised surface.

In chapter 3 it was found that the surface oxidised in ambient atmosphere for sev-

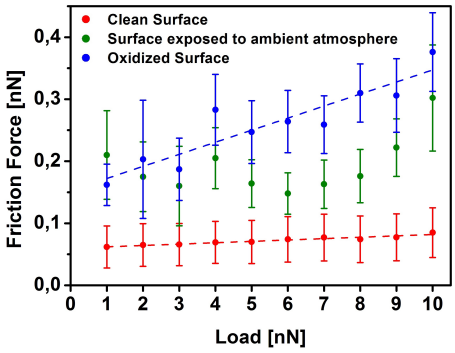


(a) Friction forces on the clean, the oxidised and the not oxidised surface which was exposed to ambient atmosphere. Measurements were performed with a cantilever of type SCD-D10.

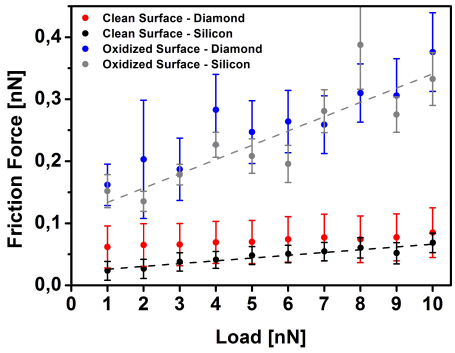


(b) Friction forces on the clean and the oxidised surface. Measurements were performed with cantilevers of type SCD-D10 and PPP-Cont.

Figure 4.7: Influence of friction force on chemical composition of surface and tip. Data points are from fig 4. Corresponding linear fits are illustrated by dashed lines.

eral seconds is covered with an initial oxide layer consisting mainly of amorphous $ZrO_2$ and $Al_2O_3$, which can be identified as the cause of the higher friction force on this surface. By XPS, an increased concentration of Cu and a depletion of Zr was detected in the top surface region of the surface which was oxidised for 30 minutes at 450K, and more surface-sensitive measurements by AES proved Zr on the oxidised surface (compare fig. 4.3c in chapter 4.2). Since the friction force on the surface exposed to ambient atmosphere, in absence of spherical particles which can be attributed to $Cu_2O$, is similar to that on the oxidised surface, we conclude that the spherical particles of $Cu_2O$ are covered with a thin layer of amorphous $ZrO_2$ and $Al_2O_3$. This indicates that this is the material which ruptures during force-distance curves on the oxidised surface and on the surface exposed to ambient atmosphere. Since ruptures were only observed during a limited amount of measurements it is suggested that the binding strength within the amorphous oxide is approximately on the order of the adhesion between the oxide and the diamond tip.

To explore the influence of chemical reactive tips, compared to chemical inert diamond tips, on the friction force, sliding experiments were performed with diamond tips of type SCD-D10 and tips of Si of type PPP-Cont. Before measurements the tips were Ion sputtered for 30 seconds to remove the $SiO_x$ cover layer. The residual amount of $SiO_x$ on the tip after sputter treatment is unknown. The measurements were performed by scanning square frames of 20nm size with a velocity of 39nm/s. During sliding residual $SiO_x$ should be removed, so that we finally assume a contact of pure Si with the sample surface. Since the friction mechanisms involve the shearing of junctions, formed by covalent bonding and welding, we will consider

the friction theories of Bowden and Tabor in the following, so that the shear stress is represented by the friction coefficient. The coefficients of friction for each combination of tip and surface were determined as the corresponding slopes of linear approximations in fig. 4.7. On the clean surface of metallic glass we obtained friction coefficients of $\mu = (1,7 \pm 0,2) \cdot 10^{-3}$ with the diamond tip and $\mu = (4,5 \pm 0,5) \cdot 10^{-3}$ with the Si tip. On the oxidised surface of metallic glass we obtained friction coefficients of $\mu = (19 \pm 3) \cdot 10^{-3}$ with the diamond tip and $\mu = (23 \pm 5) \cdot 10^{-3}$ with the Si tip. With respect to the error values the coefficient of friction is higher for Si tips on pure metallic glass compared to the friction coefficient resulting from diamond tips. On oxidised surfaces the coefficients of friction are similar for both kind of tips. In their experiments on Pt-based metallic glasses, Caron et. al. observed a higher coefficient of friction for $SiO_x$-tips compared to diamond tips. They concluded the formation of a neck between tip and surface and referred to the high affinity of Si to Pt which results in the formation of silicides.[62] According to [63] the formation enthalpies of $Zr_5Si_4$, ZrSi, and $ZrSi_2$ are -91,9kJ/mol, -94,5kJ/mol, and -60,3kJ/mol, respectively. On the oxidised surface we have to consider the formation enthalpies for compounds of $ZrO_2$ with Si between -27,9kJ/mol and 186,6kJ/mol and of $Cu_2O$ with Si.[64] For the formation of $Cu_3Si$ a formation enthalpy of -13,6kJ/mol and -10,5kJ/mol for $Cu_5Si$ was found.[65] The formation enthalpies for copper silicides challenge the one for the far more stable $Cu_2O$ (-171kJ/mol) [66]. The concept of neck formation, driven by the formation of silicides, applied to our situation explains the higher coefficient of friction on the clean surface of metallic glass by creation of silicides mainly with Zr, whereas on the oxidised surface the lower affinity of silicide formation results in a friction coefficient similar to that obtained with chemical inert diamond tips. Since the highest friction force was measured on the oxidised surface, an additional influence of the oxide's structure is suggested. Therefore, friction mechanisms were investigated over several length scales in the following, including the atomic scale.

Further friction experiments were performed in contact mode by scanning a square frame of certain dimension. Different normal forces were applied to the contact. For the measurements, a soft cantilever of type SCD-D10 was used and the scan speed was 39nm/s.
As can be seen in fig. 4.8a and b stick-slip events were observed on the clean and on the oxidised surfaces of metallic glass at normal forces between 0nN and 10nN. On the oxidised surface a spontaneous change of the stick-slip can be observed which could not be attributed to any measurement error. In the middle area of the scan

frame, indicated by the orange arrow, the stick-slip pattern is very different from the one of previously scanned lines. After further scanning of several more lines it changes its pattern again. This results in a stick-slip structure in the center of the scan frame which differs from that of the surrounding pattern. Gnecco et. al. reported a similar observation after scratching with an AFM tip on KBr.[67] The surface which was modified by the tip revealed an atomic lattice, shifted to the one of the undisturbed surface. In our case, the disturbed region expands just over several individual stick-slip structures. By taking into account the occurrence of ruptures during the previously described force-distance measurements on the oxidised surface, the localised change of stick-slip pattern is a strong indication for adhesive wear of surface material which then adheres to the tip during sliding on the oxidised surface. In our case, the worn material may be $ZrO_2$ or $Al_2O_3$ which both forms the amorphous matrix and, as previously supposed, a thin cover for the $Cu_2O$ nanoparticles within the oxide layer. Fig. 4.8c and d show the torsional force on the clean surface of metallic glass and on the oxidised surface during sliding. On the clean surface, trace and re-trace show higher similarity than on the oxidised surface. With the reduction of the load, at negative normal forces, the stick-slip starts to disappear beginning with stick-slip events of small stick lengths.
Stick-slip on amorphous surface potentials was discussed by Rivas et. al. in [68]. According to their simulations, the stick-slip length on amorphous surfaces increases with increasing strength of interaction potential between surface and tip. In this way during slipping the tip may jump over several surface structures until it sticks again, whereas at much weaker interaction potential the tip follows the surface potential and stick-slip vanishes. Craciun et al. observed irregular stick-slip on $Al_2O_3$, $SiO_2$ and glass and proposed a transition into continuous sliding at small contact areas and for large torsional spring constants. By taking into account the variation of contact surface after each slip event, and a surface interaction potential which is obtained by summing up all attractive parts of the potentials they concluded a stochastic jump behavior of the tip.[69] The Power Spectral Density (PSD) offers the possibility to identify recurring structures also in non-periodic signals and is used here to gain information about the surface structures. Normalised PSD functions from the torsional deflection, measured on the clean surface and on the oxidised surface, are shown in fig. 4.8e and f. Each graph represents the average of the PSD, calculated for each line in the fast scan direction. Stick-slip measurements on HOPG revealed a accuracy of about 30pm on the sub-nm length scale. The clean surface of metallic glass exhibits characteristic stick-slip lengths of 637pm, 229pm and 125pm. The structure of 637pm possibly represents the cluster size within the metallic glass,

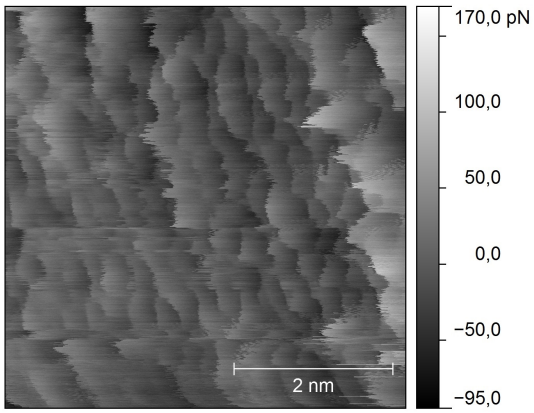


(a) Torsional Deflection on the clean surface (Scan direction: upward).

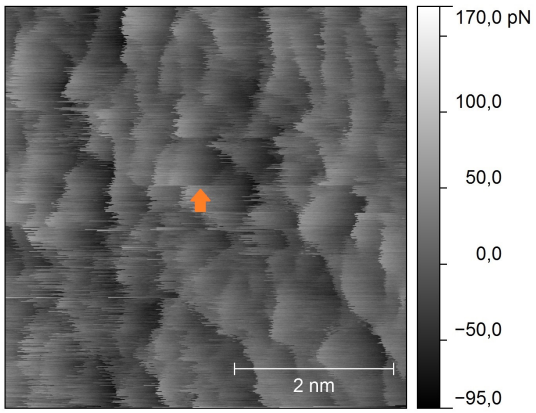


(b) Torsional Deflection on the oxidised surface surface (Scan direction: upward).

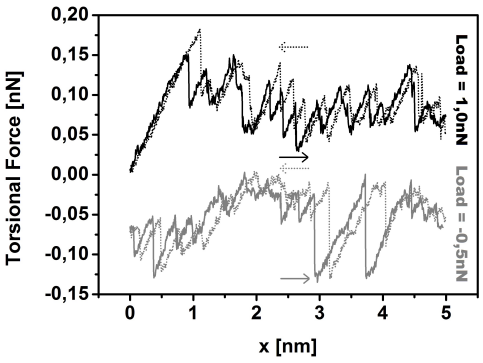


(c) Stick-slip on clean surface.

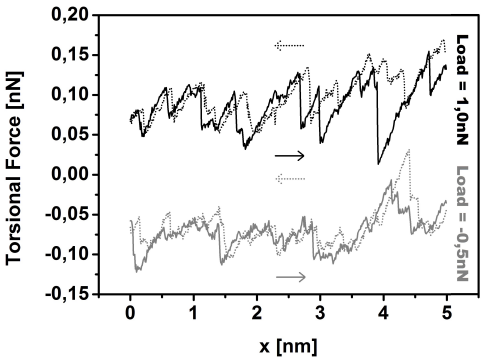


(d) Stick-slip on oxidised surface.

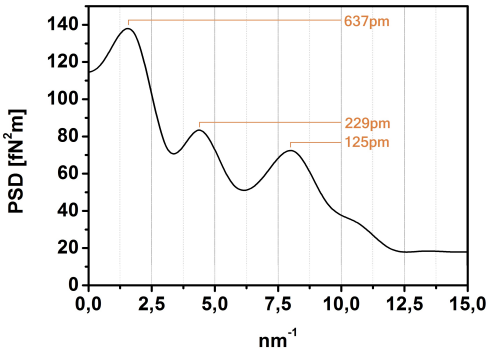


(e) Power Spectral Density of the clean surface.

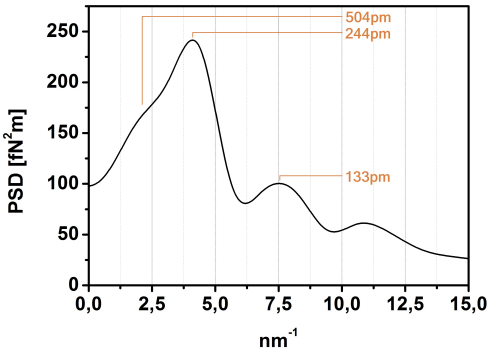


(f) Power Spectral Density of oxidised surface.

Figure 4.8: Torsional Deflection on the clean surface and on the oxidised surface, converted to units of force, measured with a cantilever of type SCD-D10 with a normal force of 1nN. Trace and Re-trace of torsional deflection signal with stick-slip events on clean and oxidised surface of metallic glass. Power Spectral Density (PSD) of torsional deflection signals on each surface.

while the length of 229pm is characteristic for atomic radii of metals. Interatomic distances of $Zr_{60}Cu_{30}Al_{10}$ metallic glass were determined by Antonowicz et. al. by X-ray absorption fine structure measurements.[70] Based on the author's results, and taking into account the measurement uncertainties, it is possible to attribute the stick-slip length of 229pm to the interatomic distances between Cu and Cu or Zr and Cu. On the oxidised surface we find stick-slip lengths of 504pm, 244pm and 133pm. The structure of about 504pm is assumed to be double the one of 244pm which can be attributed to atomic radii of metals. Owing to the limited accuracy, the length of 125pm on the clean surface is identified as the same structure as the one of 133pm on the oxidised surface and can be identified as the binding length of a carbon-carbon single-bond. With the assumptions of a tilted tip during scanning, and that the orientation of the tip's diamond crystal is not perfectly aligned along the tip axis, it may be attributed to carbon-bonds on the tip's apex.
The transition from stick-slip to continuous friction, observed with decreasing load, is quantified in the following data evaluation. Therefore, the friction curves were evaluated in a way that allowed distinguishing both friction phenomena with a single parameter. According to [71] in this approach the relation between the corrugation of the surface potential and the elastic energy stored in the probe can be expressed with the stick-slip height $F_l^{max}$, the stick-slip length $a$, and the contact stiffness $k_{exp}$, given by the lateral force and the displacement at the beginning of each stick phase, as

$$\eta = \frac{2\pi F_l^{max}}{k_{exp} a} - 1 \tag{4.14}$$

The contact stiffness is connected to the effective lateral stiffness $k$ by the parameter $\eta$ as follows:

$$k = \frac{\eta + 1}{\eta} k_{exp} \tag{4.15}$$

Fig. 4.9a shows averaged values for $\eta$ obtained on the clean and on the oxidised surface at different loads. The graphs of both surfaces hardly differ from each other. Both the clean and the oxidised surface show an increase of $\eta$ with the load. In the adhesive regime, with decreasing load, $\eta$ is aiming for values less than one. For illustration in fig. 4.9b the distributions at three different loads, obtained on the oxidised surface, are shown. With decreasing load, the total number of detectable events decreases, besides there is a shift in the distributions to lower values of $\eta$ which were determined by means of curve fitting of the respective histograms whereby error bars of $\eta$ correspond to the fitting error of the mean value. Both findings can be explained by the increased conversion of stick-slip events into continuous sliding friction with decreasing load, similar to observations on NaCl single crystals

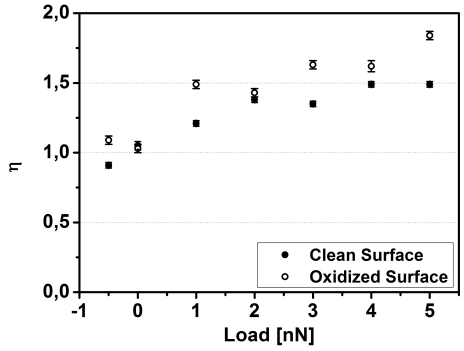


(a) Dependence of parameter $\eta$ on the load the clean surface and oxidised surface for different scan sizes.

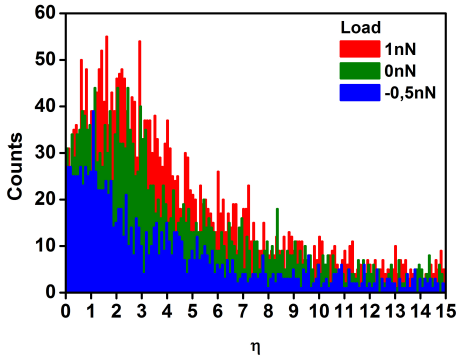


(b) Histographical distribution of $\eta$ on oxidised surface at a scan size of 5nm.

Figure 4.9: Relation between the corrugation of the surface potential and the elastic energy stored in the probe for the clean surface of metallic glass and the oxidised surface. Error bars in a) are given by the corresponding errors of average values obtained from curve fitting with a extreme-value distribution function of the corresponding histograms. Considering the widths of distributions, the errors might be underestimated.

as reported in [71]. Here, the decreasing of $\eta$ and $k_{exp}$ was related to the cease of instabilities which produce stick-slip. This process was observed as an overlap of the forward and backward friction curves which finally resulted in ultra-low friction. In fig. 4.8c and d we can see similar effects on both surfaces when normal forces are in the adhesive regime, respectively. The lower the load, the more the stick-slip seems to vanish, since the mechanism of transition from stick-slip to continuous sliding applies also to amorphous surfaces. The parameter $\eta$ does not only represent the stability of the stick-slip system, but also determines the amount of energy dissipated during the slip. The transition from pure stick-slip to continuous sliding is accompanied by a decrease of dissipated energy.[72] The datapoints in fig. 4.9a are subject to large variation, so that the dependence of $\eta$ on the load is hard to distinguish for both surfaces. Nevertheless, in tendency, $\eta$ seems slightly larger on the oxidised surface than on the clean surface. During further experiments, focussing on the influence of surface structure on tribological properties, friction measurements were performed on different scales. In fig. 4.10a, b and c friction forces are plotted against the load and it was possible to approximate all curves according to the DMT-model. Due to the already provided proof of adhesion, the Hertz model was excluded for the approximation of the data points. Since a neck formation as considered by the JKR model was not expected in contact with diamond tips, this model was also excluded for the evaluations. On the clean surface we find the friction force to be $> 0$ if $\eta < 1$. We assume that at negative normal forces the adhesion between tip

and sample leads to energy dissipation due to continuous sliding which is caused by the low curvature of surface potential corrugation. The origin of higher stability of stick-slip on the oxidised surface is unclear but the investigations described in the following provide a possible explanation for this phenomenon.

On the oxidised surface a large variation of the minimum load was found, at which the tip was separated from the surface. For scan sizes of 5nm the oxidised surface of the metallic glass is difficult to distinguish from the clean surface by friction forces. At a scan size of 50nm, the oxidised surface tends to show higher frictional forces, while at a scan size of 20nm the values of friction forces have large statistical errors (see fig. 4.10b). In fig. 4.10d the shear stress $\tau$ is related to $\tau \left(\frac{R}{E_{tot}}\right)^{2/3}$, obtained from the fit curves of the DMT-model on the oxidised surface for different scan sizes. Here, the shear stress tends to increase with increasing scan size and apparently begins to stabilise at about 50nm. On the clean surface no variation of the shear stress with changing scan size was found. From fig. 4.10e one can see a large variation in adhesion force on the oxidised surface for the different scan sizes which was deduced from the corresponding fit curve of the DMT-model. While on the clean surface the adhesion force was found to be independent on the scale, on the oxidised surface the adhesion force shows an increasing trend with increasing scan size. Noticeably, from the force-distance measurements in the previous sub-chapter we obtained an adhesion force on the clean surface of metallic glass which was higher as the one measured on the oxidised surface. This is in agreement to the findings after application of the DMT fit on the friction data of the clean surface and of the oxidised surface at a scan size of 5nm.

### 4.3.2 Topography dependence of friction

In order to understand the scale dependence of shear strengths and adhesion forces on the oxidised surface, we compare torsional forces with the surfaces topography in the following. In Fig. 4.11 the topography, and the torsional force are compared for the clean surface, and for the oxidised surface. In all measurements, a strong correlation between topography and torsional deflection was found. The entire oxidised surface is covered by spherical structures. According to PSD analysis the average size of these structures is 17nm. The oxidised surface shows a significant increase in the stick-slip length at the boundaries perpendicular to the fast scan direction. By comparing the topography with the torsional deflection at the boundaries and their periphery, it seems that the tip slips while moving towards a gap between to particles due to topography and finally sticks within crevices. On top of the spherical structures stick-slip motion of the tip is observed. As demonstrated by the profile in

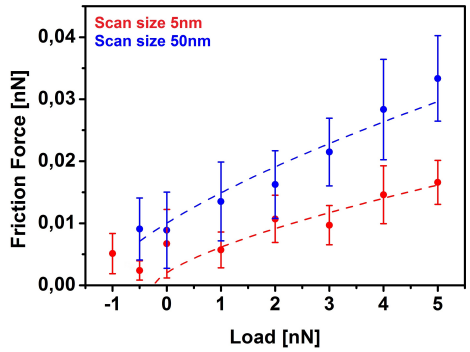


(a) Friction force against load on the oxidised surface with a scan sizes of 5nm and 50nm.

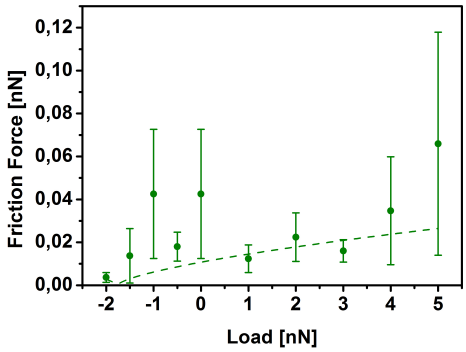


(b) Friction force against load on the oxidised surface with a scan size of 20nm.

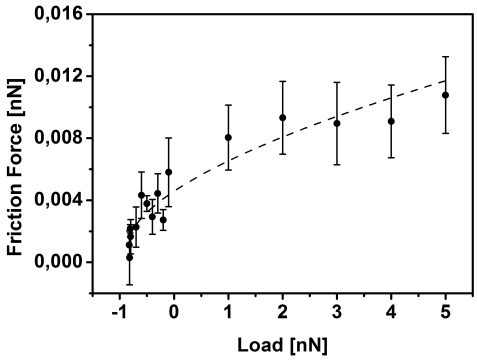


(c) Friction force against load on the clean surface with a scan size of 20nm.

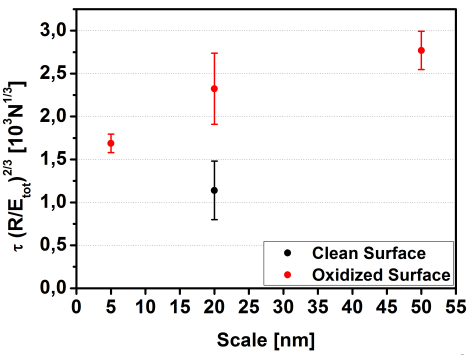


(d) Shear stress multiplied with $\left(\frac{R}{E_{tot}}\right)^{2/3}$ on clean and on oxidised surface, derived from data points obtained from scans of different frame size.

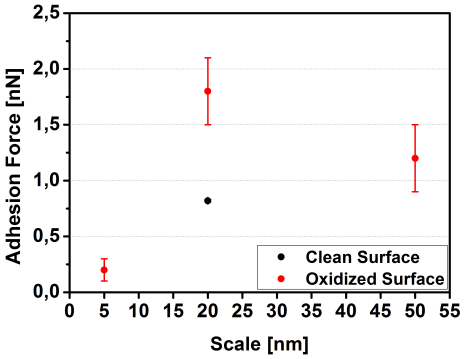


(e) Adhesion force on clean and on oxidised surface, derived from data points obtained from scans of different frame size.

Figure 4.10: Scale dependence of tribological properties on the clean surface and on the oxidised surface of metallic glass. Measurements were performed with SCD-D10.

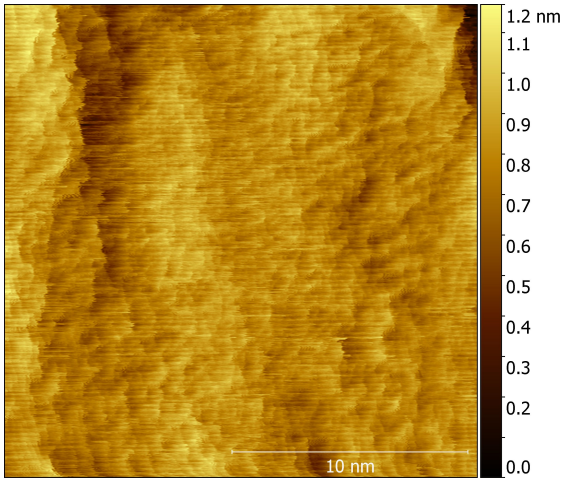


(a) Topography on clean surface.

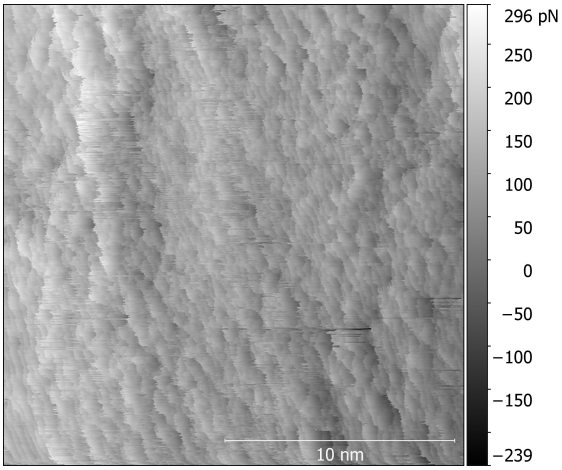


(b) Torsional deflection on clean surface.

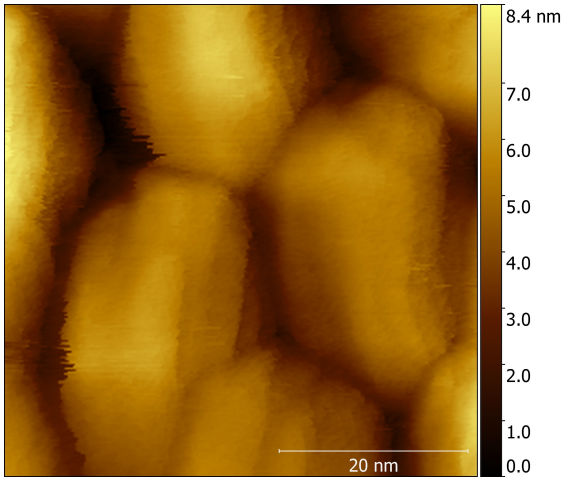


(c) Topography on oxidised surface.

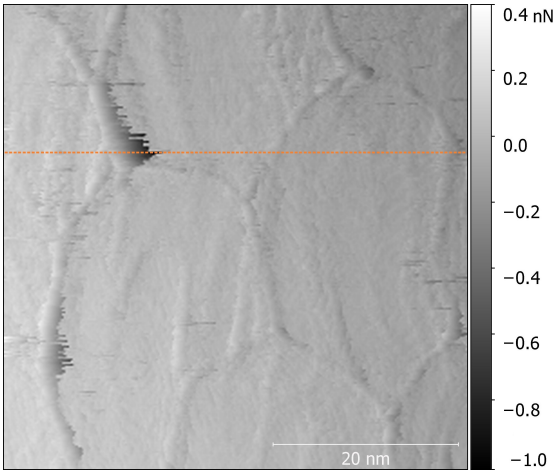


(d) Torsional deflection on oxidised surface.

Figure 4.11: Topography and torsional deflection on the clean surface of metallic glass at a scan size of 20nm and on the oxidised surface at a scan sizes of 50nm.

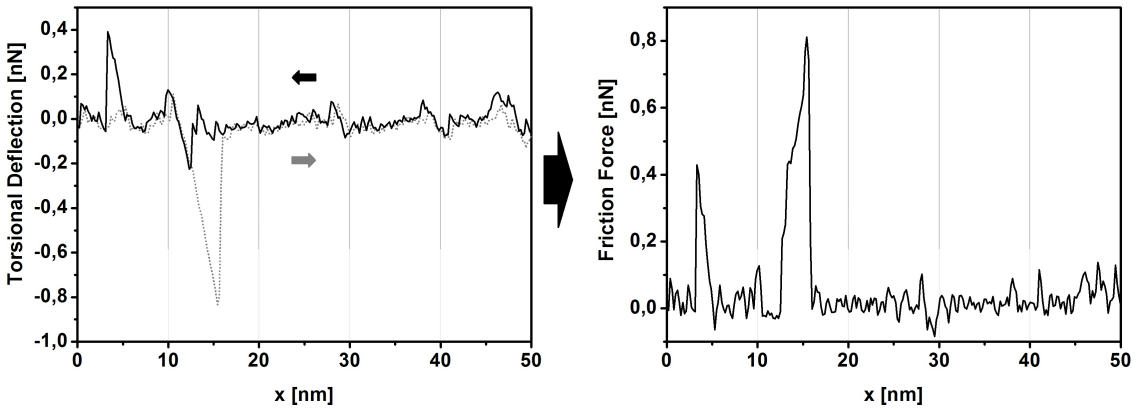


Figure 4.12: Line profile of the lateral deflection and calculated friction force on the oxidised surface with a scan size of 50nm. The position of the profile is indicated by the dashed orange line in fig. 4.11d.

fig. 4.22, extracted from the forward and backward torsional deflection signal which was measured on the oxidised surface, high friction at the boundaries is a result of a mismatch of the stick-slip in the signals for the forward and the backward scan direction of the tip. We conclude that as the tip approaches the border region of a surface particle, the tip slips into the gap between two structures due to instabilities caused by the surface tilt. The tip then sticks between both structures. As the support moves, the energy stored within the spring holding system increases until it is sufficient to release the tip by slipping out of the gap. The difference between forward and backward direction of the torsional force can be explained by asymmetries of both the tip's apex structure, and the one of the spherical structure on each side of the gap. This effect is supported by the special kind of contact between tip and surface within the gap. As the tip sticks between two structures the tip is in contact with at least two points of the surface resulting in a multi asperity contact. Another contribution to this effect may have the correlation between friction forces and surface topography due to variations of van der Waals forces as referred in (chapter 8 in [3]). As a result of our findings, the total measured shear stress and adhesion on scales larger than the surface structures, in our case about 20nm, is given by the contributions of both, the shear stress on the spherical structures and the one generated by the motion of the scanning tip in between the structures. This may also explain the tendentially higher values for $\eta$ on the oxidised surface than on the clean surface for a scale of 20nm. When the tip sticks between in the crevice between two structures, the friction is not anymore governed by the corrugation of atomic stick-slip processes. Instead, the potential to overcome is strongly related to surface topography. Assuming that the curvature of topography in between two structures is higher than the curvature of the atomic surface potential, a higher

overall stick-slip stability is observed.
Basically, the mechanism discussed in this sub-chapter should apply on each experiment, carried out with a scanning tip that can dovetail with the surface structures. This requires that no plastic deformation occurs during sliding which superimposes effects of friction with those of wear mechanisms. One example are the measurements performed with a cantilever of type CDT-Cont on the oxidised surface (see fig. 4.4a and c). The diamond coated silicon tip has a curvature radius between 100nm and 200nm and exhibits a roughness in the 10nm regime which could be able to dovetail with the structures on the oxidised surface, resulting in similar mismatches between forward and backward torsional force during sliding.

## 4.4 The influence of contact geometry and normal force on friction and wear

This subchapter reports the examination of friction and wear as strictly linked phenomena. In this context, the identification of different wear mechanisms plays an important role. Therefore, after experiments in contact mode on the clean and oxidised surfaces of the metallic glass, the sites of plastic deformations were imaged in non-contact mode in order to obtain information about the structure and amount of surface wear after plastic deformation. In the following, we first give a short introduction into non-contact AFM, followed by an overview of different deformation mechanisms of metallic glasses and of oxides, which are understood as wear in the context of this work.
During non-contact AFM the cantilever is oscillated at its resonance frequency (equation 4.3). The force acting between tip and sample, resulting from the superposition of corresponding surface potentials as illustrated in fig. 4.13b, causes a shift of resonance frequency according to

$$\Delta f = \frac{f_0}{kA^{3/2}}\gamma(z) \tag{4.16}$$

with the frequency of the unpertubed harmonic oscillation $f_0$ and

$$\gamma(z) = \frac{1}{\sqrt{2}\pi}\int_0^\infty \frac{F(x)}{\sqrt{x-z}}\mathrm{d}x \tag{4.17}$$

which is also referred as normalised frequency shift. $F(x)$ represents the interaction force between tip and sample surface. While the cantilever is driven at its resonance frequency, the deflection signal is demodulated and the frequency shift is transmitted to the z-controller. The z-controller then varies the scan height in such a way that

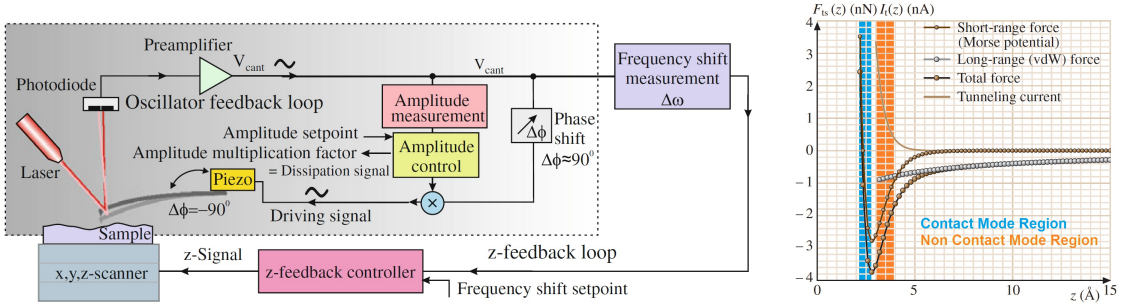


(a) Schematics of amplitude and oscillation control.

(b) Surface forces between surface and tip.

Figure 4.13: Control loop for amplitude and oscillation during non-contact imaging with AFM. Illustration of surface forces acting on a tip during measurement and indicated distances of the tip to the surface in contact mode and in non-contact mode. Schematics in a) from [57], in b) based on [3].

the frequency shift is equal to a given setpoint. Thus, the z-signal provides the topography information. A PI-controller provides a constant oscillation amplitude so that the tip-sample force only influences the frequency shift. The amplitude signal therefore provides further information about the dissipated energy between tip and sample. This signal feedback is illustrated in fig. 4.13a. The amplitude calibration was carried out as described in [73] by sequentially changing the oscillation amplitude of the cantilever by a certain factor. The value for $\Delta f$ has to be changed according to equation 4.16 in order to preserve the interaction between the tip and sample. For each set of amplitude and frequency shift, the corresponding z piezo position is read out which provides a correlation of the z position to the amplitude value. For comparison, the tip-sample distances for contact- and non-contact AFM are illustrated in fig. 4.13b.

The resolution of non-contact AFM is limited by the minimum detectable force gradient. Considering only thermal noise, the minimum detectable force gradient is given by

$$\left.\frac{\partial F}{\partial x}\right|_{min} = \sqrt{\frac{2k_B T B \cdot k}{\pi f_0 Q < z_{osc}^2 >}} \tag{4.18}$$

where $B$ is the bandwidth of the measurement, $k_B$ the Boltzmann constant, T the temperature, and $< z_{osc}^2 >$ the mean-square amplitude of the oscillation, and $Q$ is the cantilever's quality factor.(chapter 6 in [3]) Usually, the energy dissipation when scanning in non-contact mode is low compared to contact mode.[57] Therefore, we assume that the influence on the topography during imaging is neglectable in our experiments.

After investigations of plastic deformations, as presented in this chapter, various

mechanisms were identified by scratching on the nanometer scale. Their appearance were assigned to known wear modes which are described in the following.
Plastic deformation of a metallic glass is either homogeneous or inhomogeneous. Homogeneous deformation occurs primarily at high temperatures or low strain rates, resulting in mechanical creep. Homogeneous deformation of metallic glasses is often described by the free volume theory which is introduced in chapter 2.1. Atoms need space to move during local shear transformations. In the case of only a few atoms moving, the Stokes-Einstein relationship connects the diffusivity with the viscosity of the moving object. While the free volume model is rooted in the interaction of hard spheres, a more realistic approach includes bond rearrangements during deformation. Inhomogeneous deformation occurs mostly at lower temperature or high strain rates and is characterised by the formation of localised shear bands, which propagate fast trough the material, and sudden fracture. Shear banding is associated with local heating which may cause shear softening within the bands. The expected temperature rise is in a range from a few tenth Kelvin up to a few thousand Kelvin.(chapter 6 in [5])
Wear mechanisms can appear as adhesive wear, abrasive wear, delamination wear, erosive wear, fretting wear, fatigue wear, and corrosive wear. Adhesive wear occurs if two surfaces are in contact and binding forces between both surfaces initiate a material transfer. Abrasive wear is caused by hard asperities of one material which are pressed into the surface of a softer material. This leads to abrasion by several deformation modes if tangential movement is imposed. Plowing, wedge formation, or cutting are initial processes which effect material loss, mostly on the softer surface. Delamination is result of traction which induces incremental plastic shear deformation below the surface and produces pileups of dislocations which over time lead to microvoids or cracks. These cracks then coalesce and propagate parallel to the surface until the material between the crack and the surface shears, yielding thin laminated wear debris. Fatigue wear happens due to repeated loading and unloading which induces the formation of surface or subsurface cracks. A critical number of cracks then results in the breakup of the surface with the formation of large fragments.(chapter 3 in [74])
In the context of this work we introduce plowing as a deformation mechanism which penetrates the surface only during sliding. During plowing the surface material is moved due to a reordering process. If the yield pressure of the surface is exceeded, the indenter penetrates the surface before sliding begins and the wear mode is described as cutting. Cutting leads to a surface tension, perpendicular to the sliding direction and tangential to the surface, resulting in a compression of the surface material

parallel to the wear track.
In case of plowing wear, Bowden and Tabor connected plastic deformation with the friction force. In addition to pure shearing, as introduced in 4.3.1, they discussed shearing and plowing at the same time.(chapter 5 in [1]) According to their model, if $A$ is the projected area of the contact and $A'$ is the cross section of the grooved wear track, the friction force is

$$F_f = \tau A\left(F_n\right) + \tau' A'\left(F_n\right) \tag{4.19}$$

where $\tau'$ represents the resistance of movement due to plastic deformation during plowing. Since the friction coefficient can be expressed as $\mu = \frac{\mathrm{d}F_f}{\mathrm{d}F_n}$ and $A'$ is a function of $A$ this leads to

$$\mu = \frac{\tau}{p} + \frac{\tau'}{p} \cdot \frac{\partial A'}{\partial A} \tag{4.20}$$

as long as $\tau$ and $\tau'$ are independent on $F_n$. The coefficient of shearing friction $\mu_s = \frac{\tau}{p}$ and the coefficient of plowing friction $\mu_p = \frac{\tau'}{p} \cdot \frac{\partial A'}{\partial A}$ then can be identified from equation 4.20. From this it follows that for a hemispherical indenter $\mu_p$ is proportional to $\sqrt{F_n}$, whereas for conical the coefficient of plowing friction is independent on the normal force.
For a conical indenter, which forms a wear particle during sliding with a certain probability $k^*$, the total volume $V$ of generated wear particles is

$$V = k_{wear} \frac{F_n x}{p} \tag{4.21}$$

with the coefficient $k_{wear} = k^*/3$ and the length over which a contact is formed and again destroyed $x$. In case of abrasive mechanisms $k_{wear}$ represents the specific geometry of the abrasive surface.(chapter 17 in [59])
Wear is always a mixture of different wear processes and each single process has its own regimes at individual operating conditions. Increasing normal load results in an increase of the real contact area and the number of adhesive junctions. Increasing sliding velocity leads to a higher interfacial temperature which affects the material properties such as hardness or elastic modulus. Temperature also may accelerate the chemical reactivity of the surfaces, altering their physical properties or changing their structural response. A high elastic modulus results in a decrease of real contact area leading to less adhesion induced wear. The abrasive wear resistance can be increased by decreasing the elastic modulus or increasing the hardness, since hardness affects the penetration which may induce the wear process. If a critical strain is reached, the wear rate increases and depends on the fracture toughness of

the material. A low fracture toughness results in high brittleness and therefore leads to a high wear rate. A low thermal diffusivity causes a weak dissipation of frictional heat away from the interface. The thermal accumulation then may degrade the mechanical strength of the material resulting in high wear.
Depending on the environment, both contact partners are not fully in direct contact to each other. Instead, there is an interfacial layer in between, an oxide layer in ambient conditions, for example.(chapter 3 in [74]) The different breakdown mechanisms of layer systems are presented in subchapter 4.5. Wear mechanisms of oxides on the nanometer scale are only scarcely explored. During the initial stages of indentation on metal surface oxide with a thickness of a few nanometer, revealed a yield pressure which initiates an excursion associated with the onset of plasticity. Although, most of discontinuous yield excursions in metallic systems are associated with dislocation nucleation and not oxide breakdown.[14]

In the previous subchapter we found a scale dependence of friction on the oxidised surface of metallic glass. From this we consider similar dependencies on the friction and wear mechanisms at higher loads. For this reason, we distinguish between wear mechanisms, caused by standard AFM tips from those, initiated by ultra-sharp AFM tips. Standard AFM tips are of type DT or CDT, and ultra-sharp tips are of type SCD. In the following, results with regard to the mechanisms of friction and adhesion at applied loads between 10nN and 1$\mu$N are presented and discussed. The graph in fig. 4.14 shows the friction forces in a load regime in which plastic deformation can be observed on both, the clean surface of metallic glass and the oxidised surface. Standard tips result in higher friction coefficients on the oxidised surface. Between 3nN and 30nN the coefficient of friction is $\mu = (24 \pm 1) \cdot 10^{-3}$ on the oxide and $\mu = (7,9 \pm 0,3) \cdot 10^{-3}$ on the clean surface. Between 30nN and 100nN a sudden increase in the friction coefficient at a load of about 60nN indicates a change in the interaction between tip and sample surface on the clean surface. This issue is further examined in the following subchapter. On the oxidised surface the friction coefficient is $\mu = (28 \pm 4) \cdot 10^{-3}$, whereby the data point at 100nN was considered as outlying from the linear friction law and was excluded from linear regression. The friction coefficient is similar to the one obtained between 3nN and 30nN. At normal forces between 100nN and 700nN the friction forces and friction coefficients on the oxidised surface and the surface of metallic glass are similar, when measured with ultra-sharp tips. Friction coefficients are $\mu = (5 \pm 3) \cdot 10^{-3}$ on the oxidised surface, and $\mu = (6 \pm 1) \cdot 10^{-3}$ on the clean surface of metallic glass. The friction values on the clean surface show a large variation with the normal force during measurements,

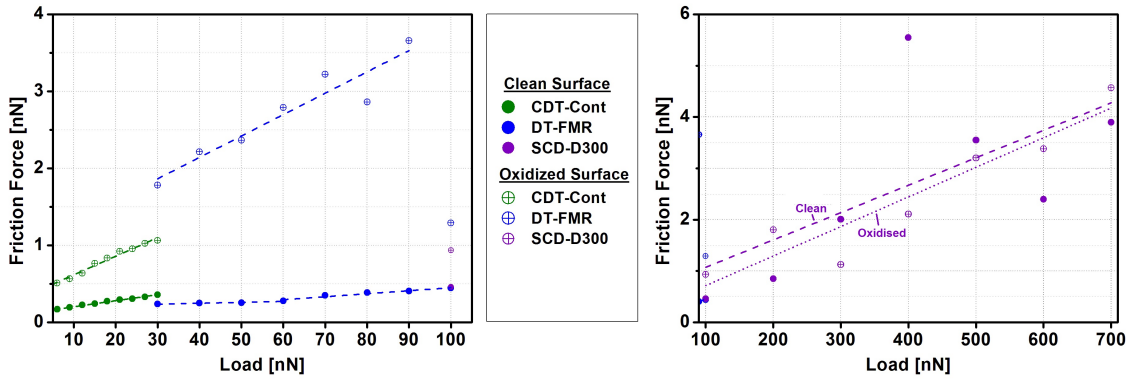


Figure 4.14: Friction forces on the clean surface of metallic glass and on the oxidised surface for different kinds of tips and cantilevers against loads between 10nN and 100nN and between 100nN and 700nN. Measurements were performed by line scans with diamond tips. Data points are from fig 4.4a.

performed with a sharp tip. After measurements, the tip was imaged either by scanning a TGT-1 test sample, or by electron microscopy, such as SEM or TEM. Unless otherwise stated, no deviation of the tip geometry from the manufacturer's information could be observed after the respective experiment. The experiments described in the following subchapter investigate the plastic deformation and the removal of surface material in a load range between 10nN and 1$\mu$N. Measurements were carried out under linear cyclic sliding with constant load. The areas of the scratched surfaces were subsequently imaged to obtain information on the nature and extent of surface wear.

### 4.4.1 Friction and wear with standard AFM-tips

The larger the contact area, the lower the pressure which is applied to the surface at a constant force. On the oxidised surface, experiments with cantilevers of type CDT-Cont and DT-FMR result in projected contact areas larger than the structure size of about 20nm.

On both surfaces multiple cycles of reciprocal sliding experiments along a 200nm long path were performed with load between 10nN and 100nN with a cantilever of type DT-FMR. Results which were obtained with an applied normal force of 70nN and are shown in fig. 4.15a for 100 cycles. On the clean surface of the metallic glass, a slide-in effect as increase in frictional force is clearly visible after the first cycle. On the oxidised surface, the initial increase in frictional force extends over several cycles. Between five and ten cycles we find a maximum friction force, whereupon a continuously decreasing course can be identified with increasing number of cycles

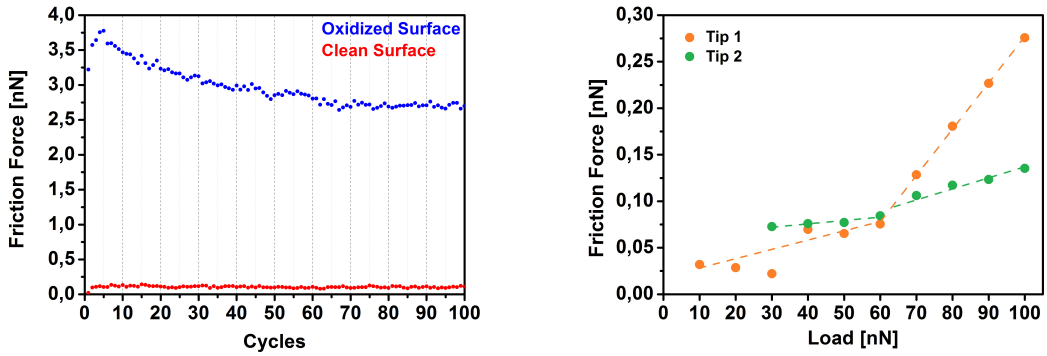


(a) Friction force on the clean surface and on the oxidised surface of metallic glass in dependence on the amount of cycles.

(b) Transition from pure shearing to shearing and plowing on the clean surface of metallic glass.

Figure 4.15: Evolution of friction forces with increasing amount of cycles and the friction force during initial single sliding on the clean surface within a load range in which the onset of plastic deformation was proved.

after which the friction force stabilises.

To gain information about the evolution of friction force and plastic deformation during cyclic sliding, the sites of scratch experiments were imaged in non-contact mode after one, ten, and 35 cycles for each load. Fig. 4.16a shows the topography of the clean surface of metallic glass after single and cyclic reciprocal nano-scratching with loads between 10nN and 100nN. Judging from the shape of wear tracks, especially at higher loads, the wear mechanism is dominated by homogeneous deformation. In [62] plastic deformations after nanoscratching with AFM were described as homogeneous and the wear mechanisms were identified as plowing. Since no wear particles were found after scratching on our surface, we also assume a plowing process in our case, although no clear pileup can be identified. In the course of the next subchapter the occurrence of pileup after nanoscatching on metallic glass with higher loads supports our assumption. According to Bowden and Tabor, the transition from pure elastic to plastic deformation is characterised by the onset of a frictional plowing component, which acts additional to the shearing of junctions (compare equation 4.20). This issue is reflected in fig. 4.15b for two different tips, both of the same type, as a change in the coefficient of friction at a load of 60nN. At loads less than or equal to 60nN the friction force showed a linear dependence on the normal force and was attributed to pure shearing mechanisms, and approximated by a linear law, resulting in a coefficient of friction of $\mu_s = (10 \pm 2) \cdot 10^{-4}$ for tip 1, and $\mu_s = (4 \pm 1) \cdot 10^{-4}$ for tip 2. From 60nN the friction force shows a linear dependence of different slope, resulting in a coefficient of friction of $\mu_s + \mu_p = (50 \pm 1) \cdot 10^{-4}$

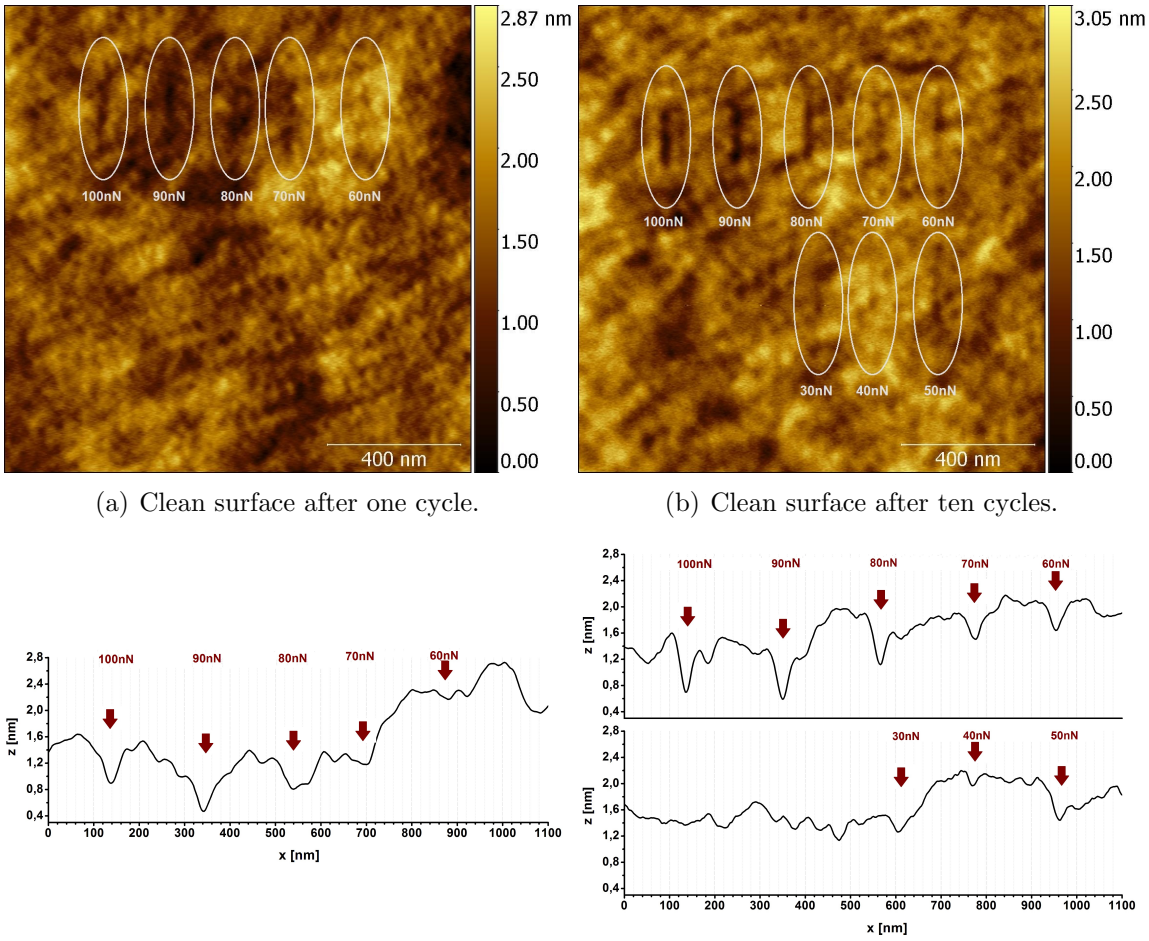


(a) Clean surface after one cycle.

(b) Clean surface after ten cycles.

(c) Surface profile after one cycle.

(d) Surface profiles after ten cycles.

Figure 4.16: Wear Tracks on clean surface of metallic glass. Surface profiles perpendicular to sliding direction averaged over the total scratch length of 200nm. Experiments were performed with a cantilever of type DT-FMR.

for tip 1, and $\mu_s + \mu_p = (12 \pm 2) \cdot 10^{-4}$ for tip 2 which leads to a coefficient of plowing friction of $\mu_p = (40 \pm 2) \cdot 10^{-4}$ for tip 1, and $\mu_p = (8 \pm 2) \cdot 10^{-4}$ for tip 2. Noticeably, between 40nN and 60nN the friction forces for both tips are very similar. Considering all data points between 10nN and 60nN the values for $\mu_s$ differ by more than a factor of two. The coefficients of plowing friction $\mu_p$ differ by a factor of eight. Considering equation 4.20, the large derivation of both values for $\mu_p$ can be explained by different relations between the projected area of the contact and the cross section of the wear track generated due to plastic deformation of the surface of metallic glass.

The onset of plastic deformation during the first cycle is also visible in fig. 4.16a at a load of 60nN. After ten cycles plastic deformation is visible from a load of 30nN (see fig. 4.16b). For normal forces between 30nN and 50nN, there is no significant increase of the friction force after a certain amount of cycles. Apparently, the onset of plastic deformation decreases with increasing amount of cycles. During wear experiments on the nanoscale as reported in [75], Colaço found a load threshold for the onset of wear on a ductile monophasic metal alloy but no dependence on the amount of cycles on the wear volume was observed. Although the reported wear experiments only considered abrasive wear, surface topographies obtained by AFM-imaging, as presented in the corresponding publication, revealed no indication for plowing mechanisms which is in contrast to our observations. According to (chapter 10 in [3]) wear on the atomic scale during cyclic sliding on a surface is related to thermal activation and is initiated by atomic defects. After the nucleation of atomic defects to a critical concentration, a wear mechanism is initialised. This process is accompanied by a sudden increase in the friction force. Since we were able to identify the onset of plowing by the increase of the friction force only during the first cycle, the occurrence of wear tracks after ten cycles of sliding with lower loads is still unclear. Nevertheless, we consider a thermally activated mechanism of defect nucleation, as described above, to be possible.

The depths and widths for each scratch after one, ten, and 35 cycles were determined from the topography profiles of fig. 4.16c and d) and are depicted in fig. 4.17. Each parameter represents the average value along the whole scratch distance, obtained from the corresponding profile after subtraction of a polynomial underground. For more detailed information, fig. 4.23a in chapter 4.4.2 illustrates this procedure. The depths after one and after ten cycles show an increasing trend with increasing load. The width after ten cycles shows a linear increase between 30nN and 60nN, after which it stabilises and, within the error, coincides with the values of one cycle. Noticeably, between 30nN and 60nN the onset of plastic deformation is identifiable

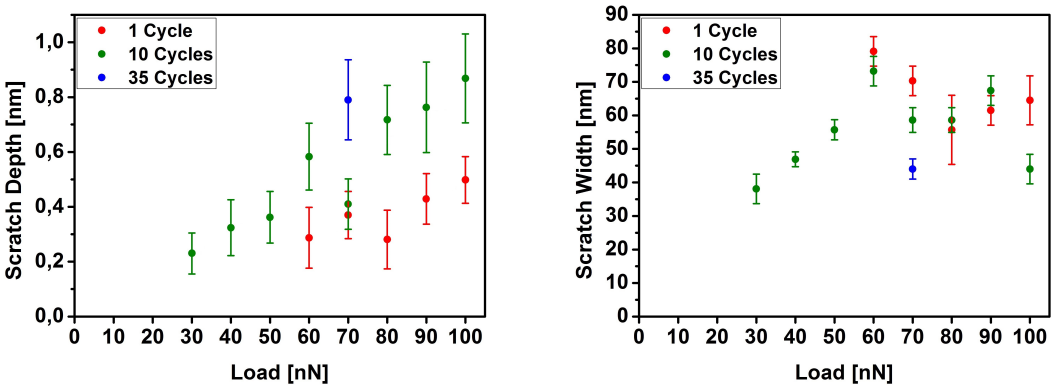


Figure 4.17: Depths and widths of wear tracks for different loads after one, ten, and 35 cycles on the clean surface of metallic glass.

between one and ten cycles, suggesting that the scratch width is stable if plastic deformation occurs during the first cycle. We assume the continuously increasing depth with increasing amount of cycles to be either a result of an unstable contact area due to the material transport during plowing, or as a result of a decrease in the hardness of the metallic glass during sliding. The latter possibility could also explain the occurrence of wear tracks after ten cycles of sliding with loads with which no scratch was observed after single sliding. After simulations of the sliding on a Zr based metallic glass, presented in [16], the authors suggested a material flow caused by combined compression and shear which results in a softer layer close to the worn surface. In [76] Bhowmic et. al. observed a lower hardness after subsequent indentations of a Zr-based metallic glass surface at the same spot. With DSC analysis they confirmed a decrease of free volume in the plastically deformed region and suggested that the the lower hardness of the deformed region results from a formation of nano-voids due to the coalescence of the excess free volume which was generated during previous plastic deformation. In our case, a softening mechanism would explain fig. 4.18a, showing a tip of the same type of cantilever after 3500 cycles along a sliding distance of 200nm, each cycle with a constant load of 120nN. The roughness of the diamond coating can be identified and amorphous material between the crystals structure is observable. The material's constituents were identified as Zr, Cu, and Al by EDX. In [77] Mulhearn et. al. related a fill-up of the harder material's roughnesses by the softer material with a change of wear mode. During cyclic sliding the indenter further penetrates the surface and metallic glass abrades and adheres to the tip where it is localised between the asperities. We suggest that the material transfer is initialised by the decreasing hardness which results, according to equation 4.21, in an increase of the wear volume. With further

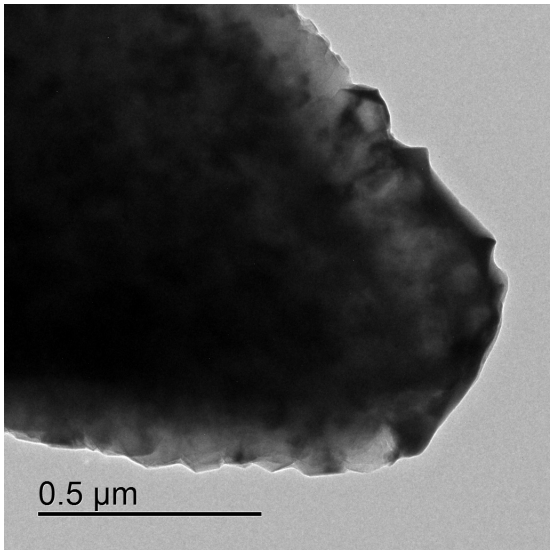


(a) Cantilever of type DT-FMR after cyclic sliding at a load of 120nN.

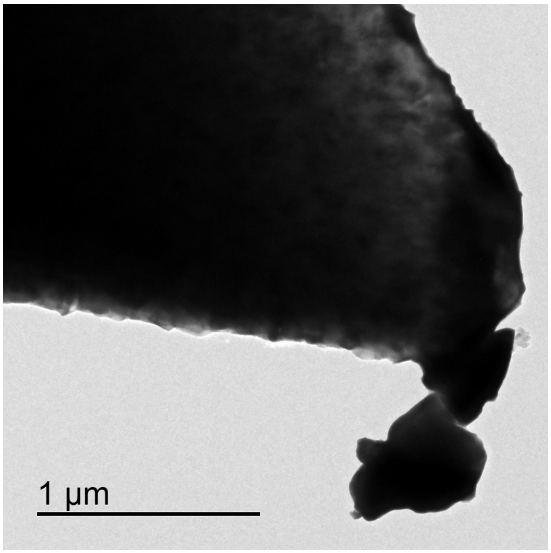


(b) Cantilever of type CDT-NCLR after cyclic sliding at a load of about 5$\mu$N.

Figure 4.18: Abrasion of surface material adhered to the tip after cyclic sliding experiments at different loads.

increasing amount of cycles the metallic glass, instead of getting plowed, adheres to the tip due to a change of the wear mode and enables the tip's lubrication. It is unclear after how many cycles lubrication affects the friction between tip and surface, but a decreasing hardness and a decrease of shear stress, due to lubrication, may explain the constant friction force with increasing amount of cycles on the metallic glass, as shown in fig. 4.15a. Noticeably, due to cyclic sliding experiments at higher loads, the metallic glass tends to fracture, as can be seen in fig. 4.18b. Wear debris was also found in [10] after scratch experiments on a Zr based bulk metallic glass with applied loads of several tenth of Newton. The authors reported the partial crystallisation of debris due to frictional heat. In our case, it is unknown if the debris on the tip in fig. 4.18b is crystallised or not.

Fig. 4.19 shows the topographies of the oxidised surfaces before a) and after b) single and cyclic reciprocal nano-scratching with loads between 10nN and 100nN. The sliding length was 200nm. In contrast to the non-contact images in chapter 3.1.2, the spherical surface structure of the oxidised surface can not be recognised. The reason for this is the larger radius of curvature of the DT-FMR tip and the roughness of the oxidised surface, which prevents the tip from approaching the surface as close as with a sharp tip, to achieve the same topographic resolution. After scratch experiments with a cantilever of type DT-FMR, the oxidised surface of metallic glass exhibited plastic deformation with no clearly distinguishable discrete scratches. Just as unclear as the localisation of the wear tracks is that of the wear

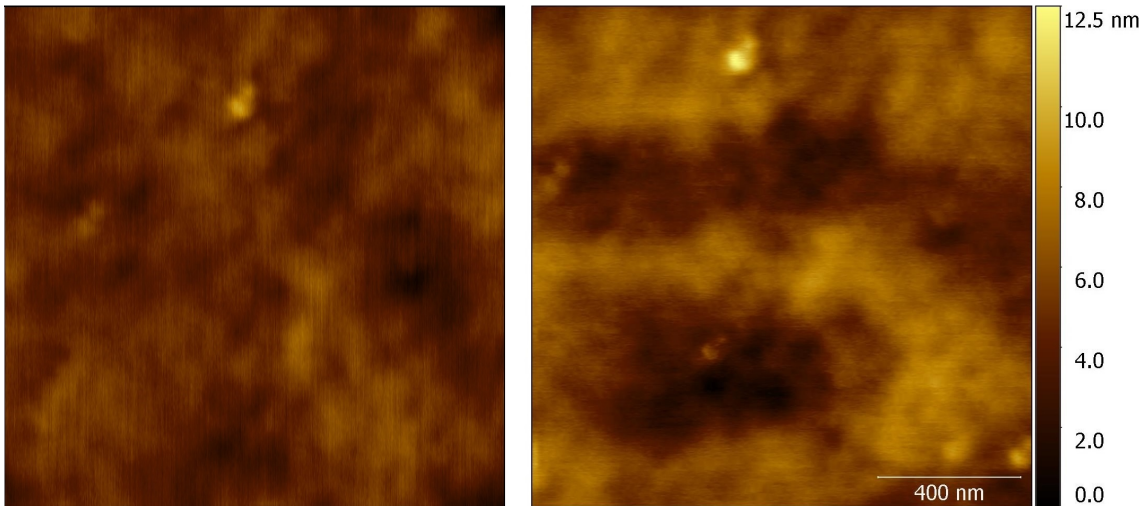


(a) Oxidised surface before (left) and after (right) one cycle.

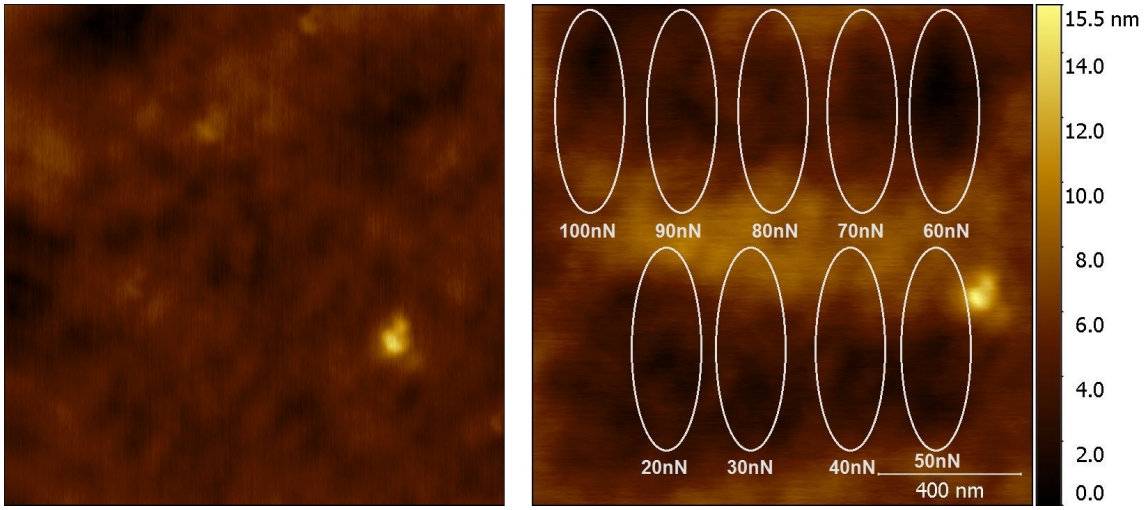


(b) Oxidised surface before (left) and after (right) ten cycles.

Figure 4.19: Wear tracks on the oxidised surface of metallic glass. Experiments were performed with a cantilever of type DT-FMR.

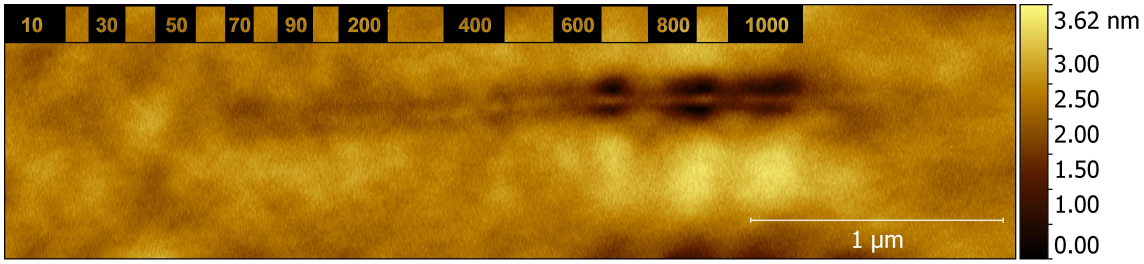


(a) Clean Surface.

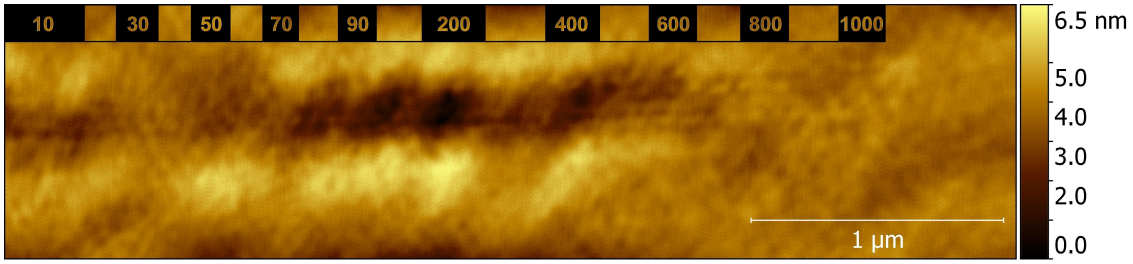


(b) Oxidised Surface.

Figure 4.20: Plastic deformation on clean surface of metallic glass and on oxidised surface after stepwise increase of the load from 10nN to 1$\mu$N while sliding on the surface with a diamond tip.

volumina, suggesting that the surface material has been deformed much more wider distributed than on the clean surface of the metallic glass. According to Rigney, the ratio of the hardnesses of the surface material and the indenter determines whether or not the surface is penetrated to produce severe wear. Various sliding tests with metals in vacuum showed that if this ratio remains greater than one during the wear process, smooth sliding and mild wear occur.[78] Since the hardnesses of the surface oxides are not expected to exceed the one of diamond, we suggest that the surface stability is provided by the structural properties of the oxide layer which supports the applied load due to the distribution of internal stresses. Nevertheless, a sufficient amount of cyclic loading could initiate the wear of the oxide layer due to surface fatigue. Further deformation processes, as proposed by Aghababaei et. al. in [61] and described in chapter 4.3.1, could have contributed to the change of friction force between the first and the tenth cycle of the measurement on the oxidised surface due to mixing or fracturing of individual asperities (compare fig. 4.15a).

For a better classification of the deformation mechanisms, a single scratch experiment was performed on both surfaces by increasing the load stepwise from 10nN to 1$\mu$N by using a cantilever of type DT-FMR. Subsequently, the respective sites were imaged to investigate the scratches. In fig. 4.20 both scratches are shown, one on the surface of the metallic glass and one on the oxidised surface. On the clean sur-

face, the onset of plastic deformation can be seen at a normal force of about 70nN. Its depth increases with increasing load. From about 600nN, both the scratch depth and its width increase suddenly stronger. Apparently, the indenter has a double tip with which it penetrates the surface. The observation of a spontaneous appearance of the wear track at a certain load is in agreement to our previous findings on the clean surface. On the oxidised surface, plastic deformation can already be seen at a load of 10nN. Between 30nN and 70nN, we observe a smooth wear track, after which the depth increases again and reaches its maximum at about 200nN. From about 500nN, the scratch depth is again minimal. Still, the contact between diamond-coated tip and oxide layer can be confirmed by the slightly recognisable wear track. The unexpected changes in the scratch depth are in agreement to the observations depicted in fig. 4.19b and support the suggestion that plastic deformation of the oxide layer occurs less localised around the tip as on the metallic glass. A spontaneous decrease in the wear rate was observable while the load increased. Before and after each measurement, the tip was imaged by a test sample of type TGT-1. After scratching on the oxidised surface, a significant increase of the tip's apex radius was observed. These findings indicate a change of contact properties between tip and surface which was confirmed by electron microscopy as depicted in fig. 4.21. After the scratch experiments on the oxidised surface, debris can be seen at the tip's apex. Apparently, the debris was displaced from the contact point and accumulated next to the apex of the tip. Besides abraded surface material, also debris from the tip was observed with SEM, and identified by EDX (fig. 4.21a). This indicates that the tip has suffered significant wear, most probably at a load of about 500nN.

A closer look at the removed surface material with TEM (fig. 4.21b) reveals an amorphous structure in which crystalline structures are embedded. In the translucent area in the middle image of fig. 4.21b Zr, Cu, Al and O were detected by EDX measurements. The crystalline structures could be assigned to $Cu_2O$, $ZrO_2$, and $Al_2O_3$. In case of $Al_2O_3$ the assignment is questionable insofar, that the lattice constant of the crystalline structure corresponds to one of $Al_2O_3$ within the scope of the measurement accuracy, but since $Al_2O_3$ has relatively many measurable lattice parameters, its assignment is very often possible, also to any other crystal structure. Judging from the penetration depths in fig. 4.20b it can be concluded that the worn surface material at the tip has its origin completely in the oxide layer, because, as stated in chapter 3, the oxide layer has a thickness of about 16nm and the maximum penetration depth is only about 6,5nm. We suppose that after a yield stress was exceeded, in our case at about 80nN, the oxide was abraded and moved by the tip. In addition, this experiment demonstrated the effect of contact size on the surface

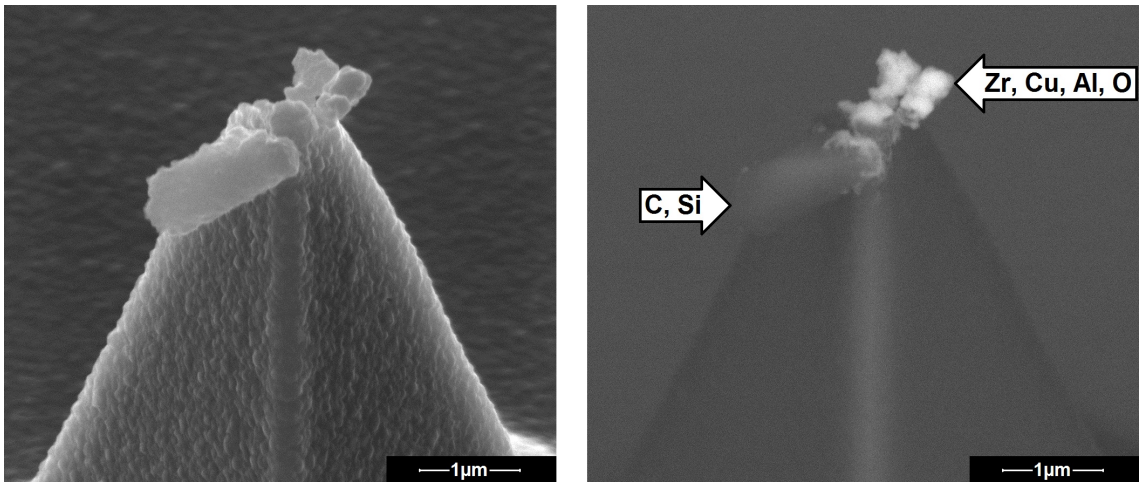


(a) Secondary electron image (left) and backscatter electron image (right).

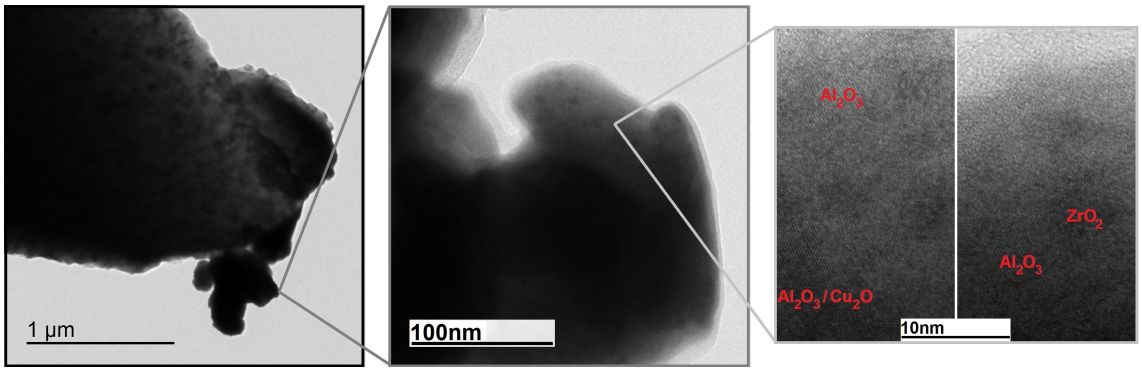


(b) TEM images.

Figure 4.21: Abraded material on diamond tip after nano-scratching on the oxidised surface.

penetration of the oxide. As the tip fractured, it was unable to penetrate the surface in the same depth as before, since the normal stress applied to the surface suddenly decreased due to the larger contact area and was insufficient to deform the surface oxide plastically.

### 4.4.2 Friction and wear with ultra-sharp AFM-tips

For the following experiments, cantilevers of type SCD-D300 were used which lead to smaller contact areas than diamond coated tips. Reciprocal nanoscratching was performed in a load range between 100nN and 1$\mu$N. Before and after each scratching process, the penetrated surface area was imaged in non-contact mode.
From 100nN to 1$\mu$N both surfaces can hardly be distinguished by friction. Fig. 4.22 shows the surfaces after the scratch experiments on the clean surface a) and on the oxidised surface b). After scratching, both surfaces differ not only in the shape of the wear tracks but also in the one of the pileups. The depths and widths averaged over the entire length of the wear track were determined as illustrated in fig. 4.23a and are shown as a function of the load in fig. 4.23b. On the clean surface, the wear track is visible after scratching with a load of 200nN. In addition to the wear track, pileup is visible for loads higher than 200nN. The shape of wear tracks is homogeneous and suggests a stable contact between the tip and the surface during plastic deformation and indicates a wear mechanism characteristic for plowing. Most of the pileup appears as abraded material which was moved by the tip and accumulated on or next to the wear track. On the oxidised surface, at lower loads, initially material from the top surface of the oxide layer gets abraded and transported by the tip. From normal forces of 500nN a scratch becomes visible on the surface. With increasing load the amount of pileup tends to increase and the worn material accumulates mostly at the ends of the wear track. On both the clean surface and the oxidised surface the graphs for both parameters are subject to large variation but the depth and width of the scratches are positively correlated. On the oxidised surface the widths and depths of scratches are constant for lower loads and increase continuously when the tip begins to cut the oxide from a normal force of 700nN. The scratch widths vary along the scratch path with an amplitude in the order of the particles size. Each volume of pileup was measured and plotted against the load, together with the volumina calculated from depths and widths of the corresponding tracks for comparison. The latter is referred as scratch volume. As approximation, a hemispherical tip apex was assumed with a diameter equal to the measured average scratch width. The scratch volume was claculated as one half of the circular area, multiplied with the scratch length. By neglecting compression of surface material during plastic deformation,

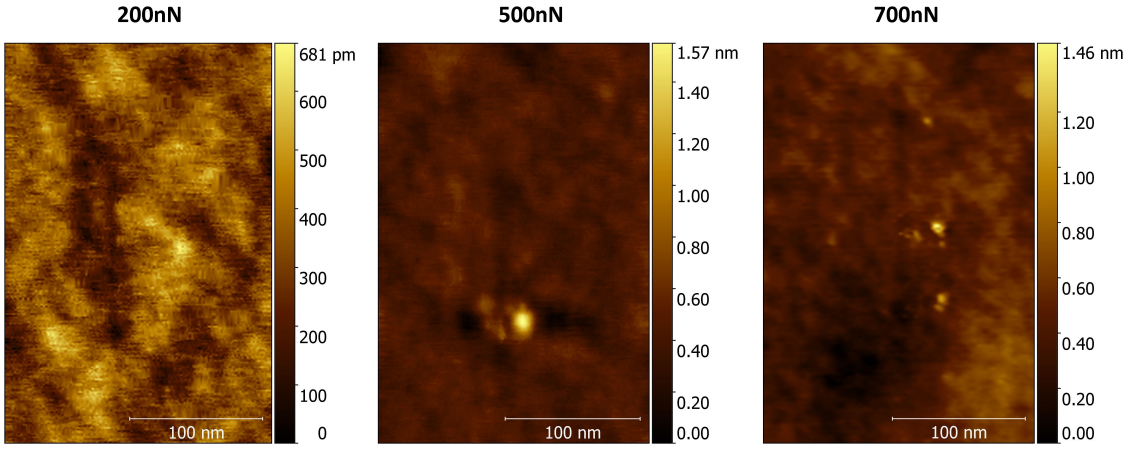


(a) Scratches on the clean surface.

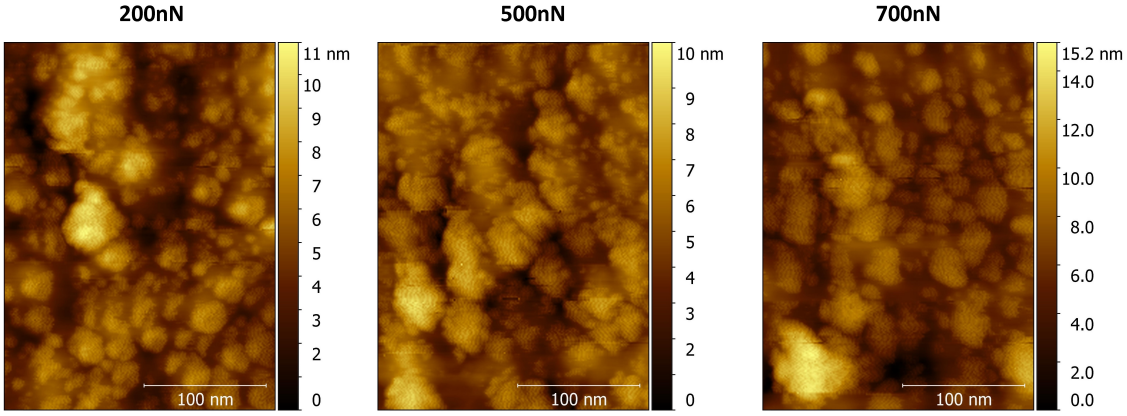


(b) Scratches on the oxidised surface.

Figure 4.22: Wear Tracks after reciprocal scratching on the clean and on the oxidised surface of metallic glass for different loads. Experiments were performed with a cantilever of type SCD-D300. The relative position of wear tracks within a scan frame on the clean surface in a) are similar to the wear tracks on the oxidised surface in b).

both volumes are expected to be equal. On the clean surface both volumes are scattered but values for loads from 500nN suggest a positive correlation between pileup volume and scratch volume. On the oxidised surface at loads of 200nN and 500nN no significant pileup can be identified. At a normal force of 700nN the pileup volume increases due to accumulation of surface material.

On the oxidised surface we see wear tracks with shapes which are dominated by the shape of the surface structures. In the course of previous investigations we found that the structure of the oxidised surface is characterised by spherical particles that is convoluted with the geometry of the scanning tip, as shown in fig. 4.22b. This indicates that plastic deformation occurs due to rearrangement of the spherical structures which in turn suggests a yield force for breaking the bonds between these particles. Therefore, this yield force, respectively yield pressure, is expected to initiate a breakdown of the oxide layer. Although scratch experiments with loads of up to 700nN enabled us to confirm the plastic deformation of the oxide layer, we were not able to observe any kind of wear which could be attributed to a breakdown of the oxide. In the following, we will present further investigations of the wear mechanism after exceeding the yield pressure. Therefore, scratch experiments were perfomed with minimum loads of 1$\mu$N. Results are shown in fig. 4.24. After scratching with a load of 1000nN the surface was apparently cut by the tip due to displacement of the oxide particles. Pileup can be identified at one end of the scratch. On the surface which was scratched with a normal force of 1200nN almost no pileup volume can be determined while the scratch volume has further increased. We suggest that the smaller pileup volume is caused by the accumulation of surface material at the end of the wear track due to scratching. The higher the load, the more surface material is transported. If the amount of worn material is sufficient, it may rather adhere to the tip than to the surface which results in a detachment of the material from the surface to the tip. Therefore, the debris cannot be imaged any more. The surface after scratching with a normal force of 1700nN visualises the phenomenon of wear transport. Only half of the 200nm long scratch can be recognised. The large amount of wear volume was not fully removed, probably due to unstable attachment to the tip which pulled it partly over the wear track before the detachment. After the surface was cut by the tip we observe a decrease of the pileup volume again whereas the scratch volume increases. The larger pileup volume can be explained by an overestimation of the volume, based on imaging due to the fact that the pileup is detached and laying on the surface so that the space in between is not considered. Our assumption about the transport of worn material by the tip is supported by the TEM image of a SCD-D300 tip after indenting and scratch-

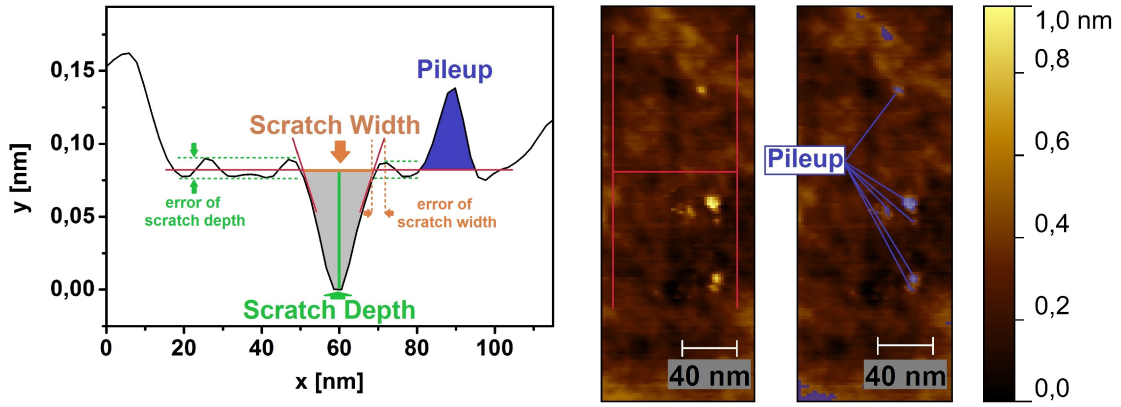


(a) Illustration of the procedure for determining the geometrical dimensions of wear tracks and the wear volume. The error values for depths and widths were derived from the accuracy of the corresponding baseline which in turn is limited by the surface roughness. Therefore, the amplitude of topographical variation in vicinity of the corresponding surface feature, for example a scratch, was related to the error signals.

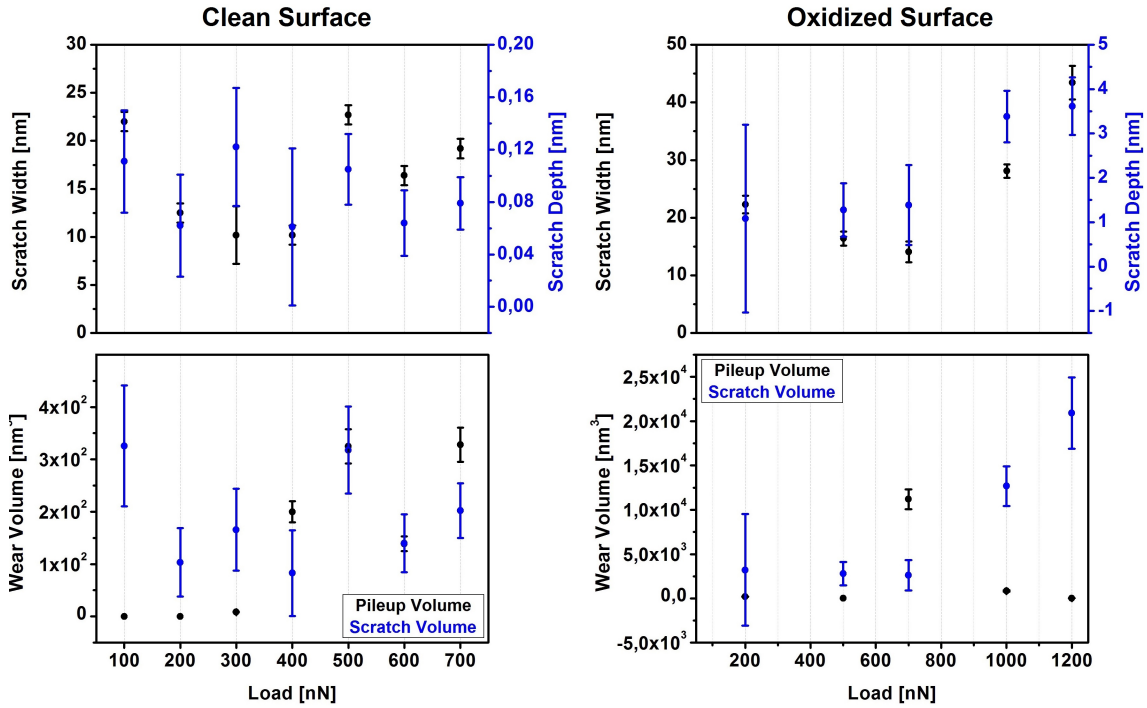


(b) Geometrical dimensions of wear tracks and the wear volume on the clean (left) and oxidised (right) surface.

Figure 4.23: Geometrical dimensions of wear tracks and wear volume after scratching on the clean and on the oxidised surface of metallic glass for different loads with a diamond tip of type SCD-D300.

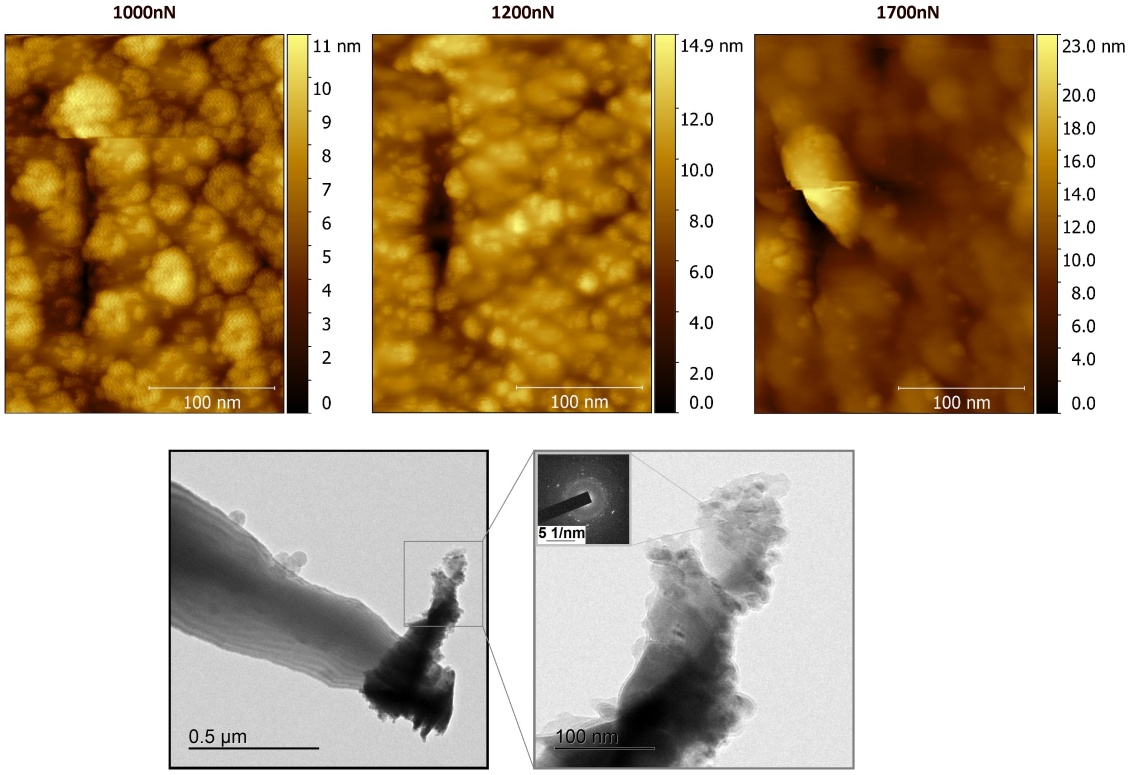


Figure 4.24: Wear tracks on the oxidised surface with loads between 1$\mu$N and 2$\mu$N with a tip of type SCD-D300 and TEM images of the tip after indenting and scratching on the oxidised surface.

ing on the oxidised surface with normal forces between 1$\mu$N and about 10$\mu$N. The wear debris of the oxidised surface can be seen at the tip's end, and the spherical structures of the oxide can be identified. Crystalline structures can also be detected within the abraded material. It is unclear if the crystallites are attributed only to the spherical oxide particles or if a partially crystallised matrix also contributes to the diffraction pattern. In any case we conclude that pileup can be abraded from the oxidised surface if it gets penetrated and cut by the tip.
Noticeably, the topography of the wear track after scratching with 1200nN offers insights into the oxide structure underneath the top surface. The crevice shows circular structures indicating that the area below the $Cu_2O$ particles is at least partially populated with other particles. These observations confirm the structure of the oxide layer as found in chapter 3. In view of the determined oxide layer thickness of about 16nm and the comparison with the SEM images, such as fig. 3.1a, from chapter 3, it is concluded that either the underlying particles are smaller than the observed particle size of 15-20nm, or the particles do not all have a perfect spherical structure but instead are flattened.

During scratch experiments on metallic glass, we observed wear mechanisms which were attributed to continuous deformation processes whereas inhomogeneous deformation due to shear band nucleation could not be verified in our experiments. According to [79] shear bands were confirmed by nano-indentation experiments on metallic glasses. In our case, low strain rates may have have caused homogeneous deformations. In contrast to our findings on the metallic glass, the deformation on the oxidised surface was interpreted mainly as a rearrangement process of the spherical oxide particles within the oxide matrix. From that is follows a pileup volume which is, in contrast to the scratch volume, an integer multiple of wear particles. Therefore, and because it is unknown if, and in which amount pileup is removed by the tip, we consider the scratch volume as being more reliable in the following analysis of mechanical parameters, which are derived from the scratch geometries on the clean and on the oxidised surface of metallic glass. By assuming a circular shaped contact area during scratching, the hardnesses for both surfaces were determined from the widths of scratches from fig. 4.22 and 4.24. The onset of wear was observed at a load of about 100nN on the clean surface of metallic glass and at a load of about 200nN on the oxidised surface. The depths and widths, corresponding to the topographies which showing the onset of wear, were considered as being not reliable for both surfaces, especially after inclusion of the corresponding errors. For this reason, the values for 100nN on the clean surface and 200nN on the

oxidised surface were excluded during further evaluation. The hardness on the clean surface of metallic glass was $H_{clean} = (1,4 \pm 0,9)$GPa and on the oxidised surface $H_{oxidised} = (0,6 \pm 0,3)$GPa. With respect to equation 4.21 the wear coefficients were derived from hardnesses and the evolution of scratch volume with increasing load for each surface. The wear coefficient was $k_{clean} = (1 \pm 1) \cdot 10^{-3}$ on the clean surface and $k_{oxidised} = (65 \pm 39) \cdot 10^{-3}$ on the oxidised surface. These values a comparable to constants for abrasive wear of two-body systems which, according to (chapter 17 in [59]), were found in a range between $0,7 \cdot 10^{-3}$ and $60 \cdot 10^{-3}$. It should be noted, the hardness refers to material systems that can be discussed in the context of continuum mechanics and therefore finds only limited application in the deformation of discrete particle systems. This has to be taken into account when penetrating the oxidised surface with an indenter with a size on the order of the oxide particles. Therefore, the comparison between the hardness values for both surfaces, obtained from experiments as presented in this work, has limited significance.

During previous experiments we have found that the surface oxide is mainly deformed by rearranging the spherical oxide particles. Therefore, we assume that abrasion, in which surface is generated, is due to the breaking of bonds between oxide particles. In order to estimate the strength of binding, indentation experiments were performed in which a diamond tip penetrated the oxidised surface with a normal force of approximately 5,5$\mu$N. The measurements were carried out on the surface which was oxidised at 450K for 60 minutes. The sample was chosen for the larger average diameter of the spherical structures, which increases the probability that only one of these particles will be touched by the tip and separates from the rest of the structure (compare fig. 3.2 and 3.3 in chapter 3). In addition, the porous appearing structure of the surface increases the degree of freedom for the motion of the particles after being separated. Before and after indentation, the surface was imaged in non-contact mode to examine the change in topography. A cantilever of type Adama was used for the measurements and the loading rate was about 60nN/s. In fig. 4.25 the surface before and after indentation, as well as the loading curve are shown.

The topographic convolution of the imaging tip and the surface results in a recurrent structure on the surface, composed of three spherical structures arranged in an arc. During indentation, the tip deforms the surface structure which can be identified in the loading curve by the sudden increase in the depth of the tip. Judging from the topography after indentation, we conclude a deformation which occurred completely within the oxide layer since oxide structures are visible below the top

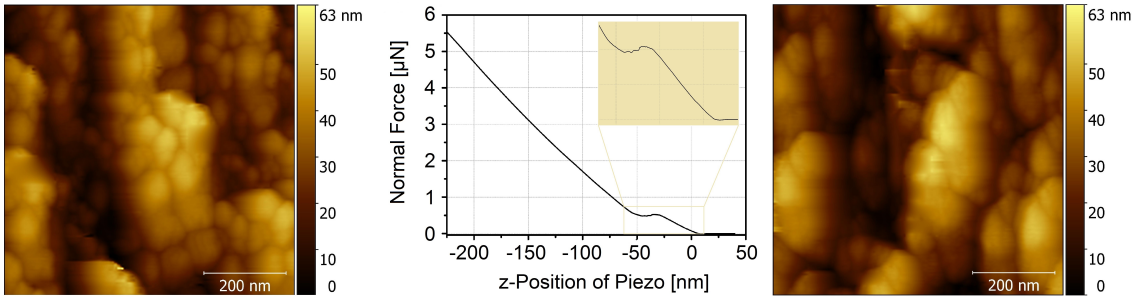


Figure 4.25: Surface oxidised at 450K for 60 minutes before (left image) and after (right image) indentation represented by the loading curve (center).

surface structures in the topography images of fig. 4.25. The corresponding load was 500nN. The inset graph of fig. 4.25 shows a zoom-in of the deformation regime in the loading curve. After the maximum force of 500nN the graph reveals a sudden decrease in the normal force which is followed by a constant normal force. After indentation, the displacement of one particle can be clearly seen in the topography. We suggest an activation of the deformation mechanism at a normal force of 500nN which yields an activation energy of about 50keV for the displacement which represents the binding energy of the oxide particle with the surrounding material. As observed on metallic glasses in [79] by Egami et. al. and on oxidised metallic surfaces in [13] by Bahr et. al., the deformation mechanism we found has a yield point, but not a discrete excursion. Instead, after plastic deformation was initiated, a continuous deformation occurred. The constant normal force during indentation indicates the presence of internal friction mechanisms between oxide particles. It is unknown from how many surrounding oxide particle the one particle was detached. Therefore, the force of 500nN and the energy of 50keV may be overestimated. Also unclear is how the contact area between all contact partners changed during motion. For the oxidised surface the finding of a yield force for plastic deformation explains the normal force for the onset of plastic deformation during scratch experiments which is about the same order of magnitude. The identification of cutting and abrasive wear during the scratch experiments is confirmed by the observation of single oxide particles moving due to indentation which, in addition to friction within the oxides constituents, determines the mechanism of plastic deformation of the oxide layer. Noticeably, the binding strength between oxide particles appears to be significantly weaker than the bonds within the particles, as they were not found to be fractured after indentation.

## 4.5 Wear processes at the microscale

From the experiments described previously, we learned that penetration into the oxidised surface depends strongly on the contact size. The experiments presented in chapter 4.4.1 showed that contact sizes, significantly larger than the oxide particles, prevent the indenter from further penetration into the oxide which results in plastic deformation due to plowing. The support of the applied load may happen due to transformation of the contact pressure into a homogeneous distribution of stresses within the oxide. Therefore, the stability of interface between metallic glass and oxide layer becomes more and more important with increasing load. In this subchapter we will investigate the wear mechanisms of the oxide layer as compound structure, coating the metallic glass.

An oxide layer can fracture in different modes, depending on the applied load, the coating thickness, the residual stresses in the layer, the indenter radius, the hardness of the substrate and the interfacial adhesion. Thin coatings preferentially fracture due to buckling if they are able to bend in response of applied stresses, whereas thicker coatings will fail by wedge spallation. A sharp transition indicates an adhesive failure at the interface when the layer is stripped from the substrate at a critical yield stress. A high hardness of the layer can result in additional wear modes such as chipping within the coating, and, due to high adhesion between a brittle layer and the coated material, also chipping within the substrate can occur.[80]

In order to observe the deformation of the oxide layer, and achieve insights into the interfacial binding mechanisms between metallic glass and oxide layer, scratch experiments were performed in the chamber of an ESEM. During the experiments, the deformed surface was imaged by SEM in time steps of several seconds. As indenter a tungsten wire with an apex radius of 200nm was moved by piezo actors of a micro-manipulator. From the geometry of plastic deformation and the hardness of the metallic glass, the load, applied to the surface was estimated to be in a range of 200$\mu$N to 600$\mu$N. The resulting contact pressure was about ten times higher than the one produced in the previous AFM experiments with diamond coated tips of type DT-FMR. Fig. 4.26 depicts the wear track on a surface of $Zr_{60}Cu_{30}Al_{10}$ bulk metallic glass which was oxidised at 450K for 30 minutes.

The oxide layer uniformly covers the surface and has spherical structures of a few nanometer in diameter. In the upper picture the tip can be seen on the left after it has produced a scratch on the surface, starting on the right side of the picture. The normal force on the surface was varied due to elastic bending of the tungsten wire during approaching and retracting. The shape of the wear track is mainly characterised by the delamination of the oxide from the surface of metallic glass.

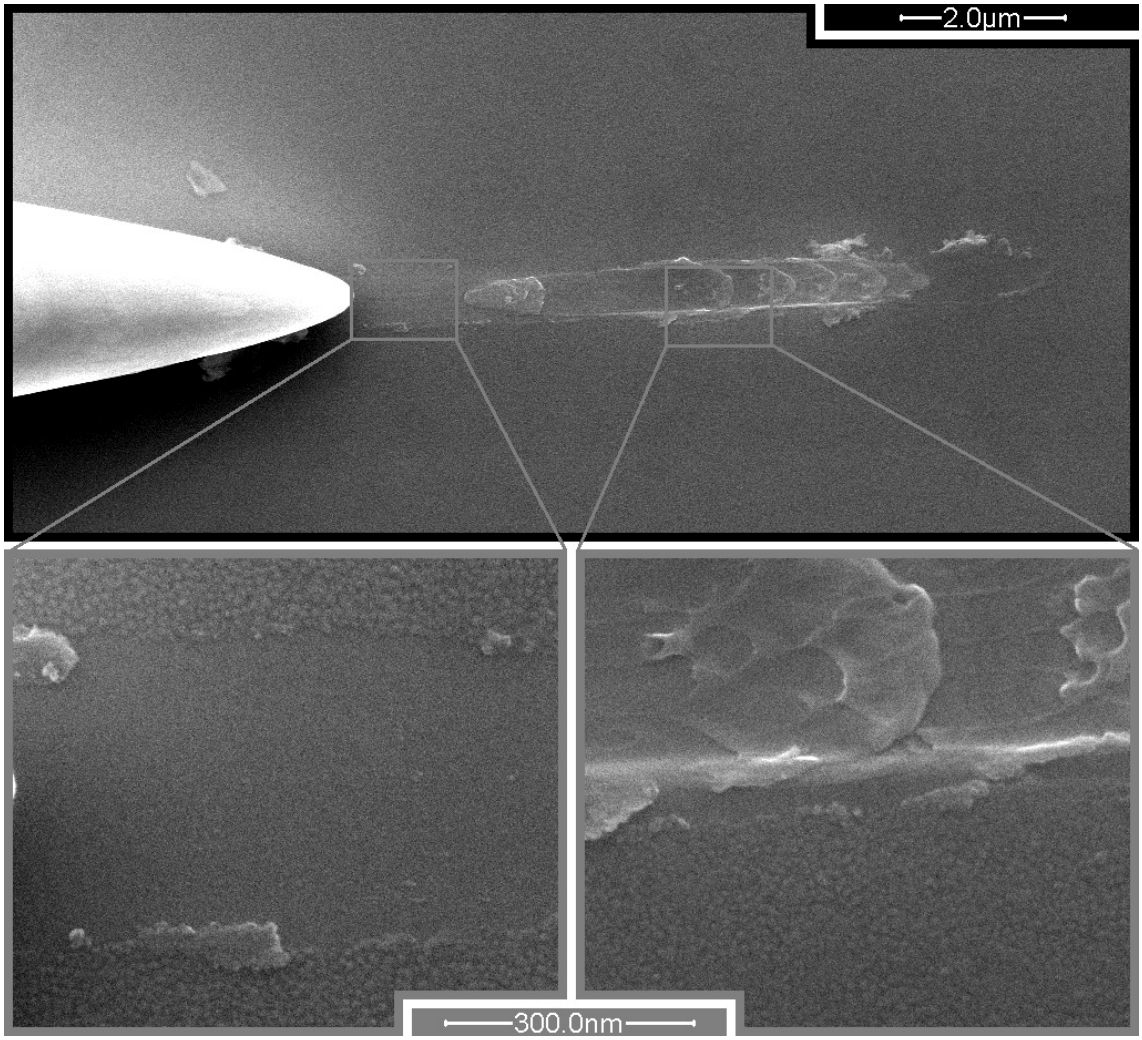


Figure 4.26: Plastic deformation of metallic glass and delamination of the oxide layer after scratching.

In the center of the frame the load was higher than within the other areas of the track, so that the plastic deformation of the metallic glass was induced. The curved structures of the metallic glass were created by moving the tip back and forth. In addition, remnants of abraded material can be seen in some places, which can be assigned to the amorphous metal. At the boundary areas, where the oxide has been separated from the residual oxide layer, reprecipitations of the oxide, and abrasion of oxide can be seen in some places. The shape of the removed oxide material indicates that the spherical structures are bonded together.
The curved, vein-like structures on the surface of the metallic glass after plastic deformation in the third image of fig. 4.26 are similar to patterns observed by Qu et. al. in [81] on the external surface of Zr-based bulk metallic glass after compression. In [82] this fracture morphology on Mg-based bulk metallic glass after surface fracture was attributed to the activation of plastic flow processes as the result of

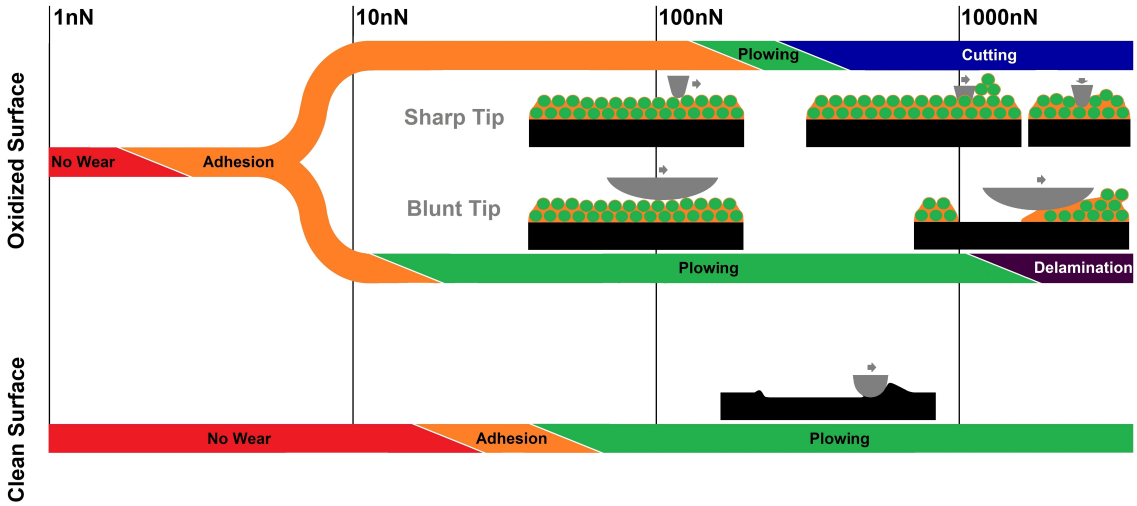


Figure 4.27: Illustration of the evolution of wear on the oxidised surface and on the clean surface of metallic glass with increasing load. In each picture of tip-sample-interaction, the metallic glass is drawn black, the amorphous oxide matrix is orange, and the particles are green.

local softening. With respect to (chapter 6 in [5]) we suggest that this mechanism is related to shear softening within nucleated shear bands.

## 4.6 Discussion of results

In this chapter, tribological mechanisms on the nanoscale were investigated on a surface of a $Zr_{60}Cu_{30}Al_{10}$ bulk metallic glass, oxidised at 450K for 30 minutes, and comparative experiments were performed on the clean surface of the metallic glass. Fundamental friction and wear mechanisms on both surfaces were identified and compared. The measurements were mainly carried out by contact and non-contact AFM in ultra-high vacuum. Additional experiments were performed with a micro-manipulator on the microscale.
In chapter 4.3.1 fig. 4.4a presents an overview of friction forces for different tips on the clean surface and on the oxidised surface of metallic glass. Fig 4.27 illustrates the evolution of associated wear mechanisms with increasing load. Together, both graphs represent the basic results of tribological experiments on the metallic glass and its oxidised surface in terms of friction and wear. These are discussed in the following.

At normal forces less than 10nN friction is scarcely influenced by plastic deformation and stick-slip friction occurs on the clean, and on the oxidised surface of metallic glass. The surface roughness strongly influences the friction on the oxidised surface on scales larger than 20nm. The more the tip is able to dovetail with the

structure of surface, the higher the friction. Constituents of the amorphous oxide matrix can bind adhesively to the indenter, whereby material from the embedding amorphous matrix is prone to be worn. In addition, these matrix oxides increase the shear stress compared to the one on the clean surface of metallic glass. On the smooth surface of metallic glass friction force is only correlated with the topography on atomic scale. The topographical effects on the friction at loads of up to 10nN are illustrated in fig. 4.28.. Note that the shear stress $\tau$ is scaled by the tip's apex radius $R$, and the reduced Young's modulus $E_{tot}$ which is given by equation 4.8 and might differ for clean and oxidised surface of metallic glass. We obtain the poisson ratios and the elastic moduli for a $Zr_{50}Cu_{40}Al_{10}$ bulk metallic glass from [83]. Assuming the elastic properties of the oxide to be dominated by the ones of the oxide particles we consider the elastic properties for $Cu_2O$ nanocubes from [84], and for diamond from [85]. Now the values for the shear stresses on the clean and on the oxidised surface can be compared to each other. The measurements on both surfaces were performed with the same tip, hence $R$ is the same. Since the literature values for poisson ratios and elastic moduli are very similar for the Zr based metallic glass and $Cu_2O$, the deviation of ratio between the shear stress on the clean surface and the shear stress on the oxidised surface at a scale of 5nm can be estimated to 6%. This results in a shear stress on the oxidised surface, at a scale of 5nm, which is about 40% higher than the one on the clean surface.

On the clean surface of metallic glass a chemical reactive indenter results in higher friction coefficients either due to reaction or by alloying with the surface material. The chemical more inert oxide layer prevents such reactions, so that chemical reactive tips have less effect on friction on the oxidised surface.

The onset of plastic deformation is continuous on the oxidised surface, whereas on the clean surface of metallic glass it is indicated by a discrete increase in the friction force. If deformation occurs on the oxidised surface, the geometrical aspects of contact partners decide whether the surface is penetrated or not. The onset of plastic deformation induced by an indenter with an apex radius significantly larger than the surface structure is characterised by plowing mechanisms. The individual structures absorb the normal stress as composite and distribute it to the sides and underlying material which thereby is plastically compressed. The indenter does not penetrate the surface, so a shallow and wide distributed wear track is observed. With increasing load the wear mode changes into abrasion with subsequent delamination of the oxide layer which shears from the smooth surface of metallic glass.

The smaller the indenting surface contact, the more the surface structure is penetrated and stressed in lateral direction during sliding, which results in the fracture

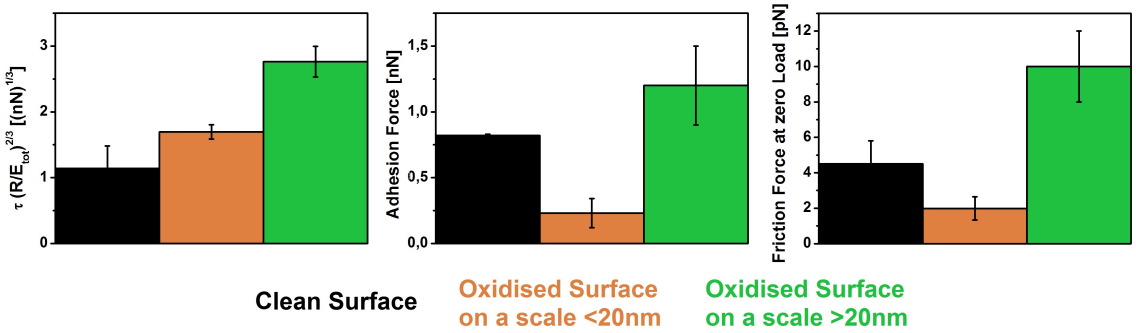


Figure 4.28: Comparisson of the shear stress, the adhesion force, and the friction force at a normal force of 0nN, for the metallic glass and the oxide matrix, obtained on scales <20nm and >20nm. Measured with a diamond tip.

of bonds in between the oxides constituents. The indenter then cuts the oxide layer by moving the oxide tangential to the surface plane. Worn surface material can be plowed or it adheres to the indenter, is carried away and deposited mainly at the ends of the deep wear track. In this way different wear modes are activated together during sliding and the width of plastic deformation can become larger than the apex radius of the indenter. The amount of worn material is significantly higher on the oxidised surface. On the clean surface of metallic glass plastic deformation is dominated by plowing.

During cyclic sliding material transfer from the metallic glass to the tip results in lubrication of the tip and promotes a change of wear mode. On the oxidised surface, below the yield stress of delamination, the oxide forms a protective layer which prevents the indenter from penetration. By using Si tips, the findings in [62] regarding the dependence of wear-less friction on the chemistry of the contact partners could be supplemented. As origin of this phenomenon, the affinity of Si to the surface metal was identified by the authors which, in our experiments, led to a higher coefficient of friction on the metallic glass than on the less reactive oxidised surface. Our observations of higher friction force on the oxidised surface are in agreement with results from [17]. Friction forces were found to be higher on the surface of metallic glass which was annealed in air compared to an as-cast sample surface. The authors attributed this effect to the presence of hydroxide-bonded metal on the annealed surface. Our findings of scale dependent sliding friction and adhesion, caused by surface roughness, could be the an additional, or the real reason for their observations. This assumption is supported by topography profiles of the as-cast and the annealed surface in [17] which show a higher roughness after thermal surface treatment.

In our experiments we found that, compared to experiments with tips of larger apex radius, the friction on both surfaces during plastic deformation, measured with sharp

tips, is more similar. This supports the observation that friction at low surface penetration is influenced by the topography, while at deeper penetration the plastic deformation determines the friction.
A correlation between friction force and wear volume was found during experiments with sharp tips on the clean and on the oxidised surface. On the clean surface of metallic glass homogeneous deformation mechanisms were identified. Both is in agreement to the findings reported in [18]. Homogeneous deformation was related to the confinement of stress field in a small volume within the metallic glass below the tip. In our experiments, a spreading of the stress field below the tip could explain the expanded wear tracks on the oxidised surface after scratching with a tip of large apex radius. This is supported by less pronounced pileups on the annealed metallic glass compared to the pileups on the as-cast sample after scratching with diamond coated tips Si tips in [18]. A spreading stress field within the oxide may also act as initiator for delamination of the oxide layer at higher normal forces.

# 5 Conclusions and Outlook

In this work fundamental mechanisms of friction and wear on the atomic scale were studied for different oxidation states of metallic glass surfaces. Tribological experiments were performed on a continuous load scale, extending over three decades with different cantilevers starting from 1nN. Macroscopically observable signs of wear were explored on a fundamental, molecular level. Although the oxidation of metal alloys is a highly complex stochastic process, it has nevertheless been possible to produce oxide coating systems that can be reproduced down to the nanometer scale. In this final chapter a summary of the basic findings is given which is followed by an outlook on experiments which may proceed the investigations presented in this work.

## 5.1 Results

1. $Zr_{60}Cu_{30}Al_{10}$ bulk metallic glass samples were produced by suction casting, and $Ni_{62}Nb_{38}$ bulk metallic glass samples were successfully produced by suction casting for the first time.

2. Oxidation of $Zr_{60}Cu_{30}Al_{10}$ starts with the diffusion of oxygen through the metal surface and proceeds with diffusion of metal ions through the oxide layer grown so far.

3. The oxidation temperature hardly affects the chemical composition and distribution of constituents of the oxide coating as long as an amorphous matrix is maintained. The crystallisation temperature of the oxides is below that of the $Zr_{60}Cu_{30}Al_{10}$ bulk metallic glass.

4. Due to crystallisation, the topography of the oxidised surface is determined by the oxidation temperature, rather than the oxidation time. Below the crystallisation temperature of the oxides, the oxide layer consists mainly of an amorphous matrix of $ZrO_2$ and $Al_2O_3$ with embedded crystalline $Cu_2O$ nanoparticles. The density of these particles determines both the internal structure of the layer and the top surface structure. There is a sharp transition between metallic glass and surface oxide.

5. For the nanotribology studies, we produced atomically smooth surfaces on the $Zr_{60}Cu_{30}Al_{10}$ and $Ni_{62}Nb_{38}$ bulk metallic glass samples by means of mechanical processing and ion milling. Some $Cu_2O$ nanoparticles grow into the surface of the metallic glass where they leave holes after argon sputtering.

6. The chemical reactivity of Si AFM tips increases the friction coefficient on the surface of the metallic glass whereas friction on the chemical more inert oxide surface is less influenced by chemistry.

7. Stick-slip friction is observable on both, the metallic glass and the oxide on scales of up to 50nm. On the oxidised surface stick-slip friction is influenced by the amorphous oxide matrix which is prone to adhesive wear.

8. Due to surface roughness, the friction on the oxidised surface is influenced by the topography on the nanoscale which is determined by the structure of nanoparticles. The interplay of asperities of both, the tip and the oxidised surface results in an increase of friction with increasing scale.

9. If scratching occurs, the sharpness of the AFM tip decides whether the oxidised surface is penetrated or not, resulting in different wear mechanisms. Indenters with contact areas of the same scale as the oxides surface structure enable the penetration of the surface and lead to cutting wear, whereas indenter with larger contact areas initiate plowing and eventually delamination from the surface of metallic glass.

10. Cyclic sliding on the surface of metallic glass leads to increasing penetration depth and promotes material transfer from the metallic glass to the indenter. On the oxidised surface, as long as no delamination occurs, the surface penetration tends to stabilise during cyclic sliding with indenters with apex radii larger than the surface structure. This prevents further penetration of the oxidised surface.

## 5.2 Outlook

The strength of metallic glasses is closely related to the chemical and physical properties of their constituents. The yield strength of ductile glassy alloys correlates with the glass transition temperature which scales almost linearly to the molar volume.(chapter 6 in [5]) Therefore, the comparison of nanomechanical properties of metallic glasses of different composition, and thus different glass transition temperature, is indispensable to obtain a more global understanding of the interaction between indenter and material surface. Additional reasons for the investigation of other alloys and their oxides are the different oxidation dynamics that lead not only to different chemical compositions but also may result in different structures of the oxide layers. One example is provided by Louzguine-Luzgin et. al. who reported about the preparation of $Ni_{62}Nb_{38}$ metallic glass by melt spinning technique.[86]

Oxidation at a temperature of 573K resulted in the formation of an amorphous phase of $Nb_2O_5$ acting as surface oxide. Within the surface Ni nanoparticles with a size of several nanometer were embedded. The special features of the oxide layer are its transparency and its superparamagnetic properties which makes the material suitable for magneto-optical applications.
In the following, we summarise the results of preliminary tribological and electrical experiments, carried out by Current Sensing AFM (CS-AFM), on clean and on oxidised surfaces of $Ni_{62}Nb_{38}$ bulk metallic glass. Sample material was produced by suction casting and the surface oxidation was carried out in synthetic air with concentrations of 80%$N_2$ and 20%$O_2$ by use of TGA. The crucible providing a sample with cross sectional dimensions of (1,0 X 8,0)mm did not produce fully amorphous sample material. By preparing a crucible with cross sectional dimensions of (1,0 X 3,0)mm, the surface to volume ratio has been increased from 2,3$mm^{-1}$ to 2,7$mm^{-1}$ (compare chapter 2, fig. 2.3b and table 1.1). The increased cooling rate enabled the production of $Ni_{62}Nb_{38}$ bulk metallic glass. Fig. 5.1 shows the XRD graph of sample material obtained from the larger and the smaller crucible. In both diffraction graphs the short range order of an amorphous phase is clearly visible between 30° and 50°. The diffraction peaks in the upper graph indicate partial crystallisation of the sample material during the production process. The lower graph shows the result after changing from the larger to the smaller crucible which provides a cooling rate sufficient to prevent any crystallisation.
The sample surfaces of $Ni_{62}Nb_{38}$ bulk metallic glass were mechanically prepared as reported in chapter 2.3. After ion milling procedure the surfaces were oxidised and characterised by electron microscopy and XPS. Results of surface imaging by SEM are visible in fig. 5.2a and b.

The smooth surface is covered with particles with sizes of several tens of nanometer. Backscatter electron images revealed that these particles have higher average atomic number than the underground.
In fig. 2c the cross section of chemical composition of the oxide layer is shown. Measurements were performed by XPS after different times of ion etching. After etch times longer than 1000 seconds the atomic concentrations are those of the bulk metallic glass, although there is a deviation of about 6% from the expected atomic ratios. A similar deviation in the atomic concentrations was found on the prepared surfaces of $Zr_{60}Cu_{30}Al_{10}$ bulk metallic glass (compare chapter 3.2.2). The top surface of the oxide layer reveals an enrichment of NiO whose concentration decreases rapidly, giving rise to metallic Ni and Nb. Throughout almost the whole oxide layer we detected $Nb_2O_5$. At the transition to the metallic glass the concentration of

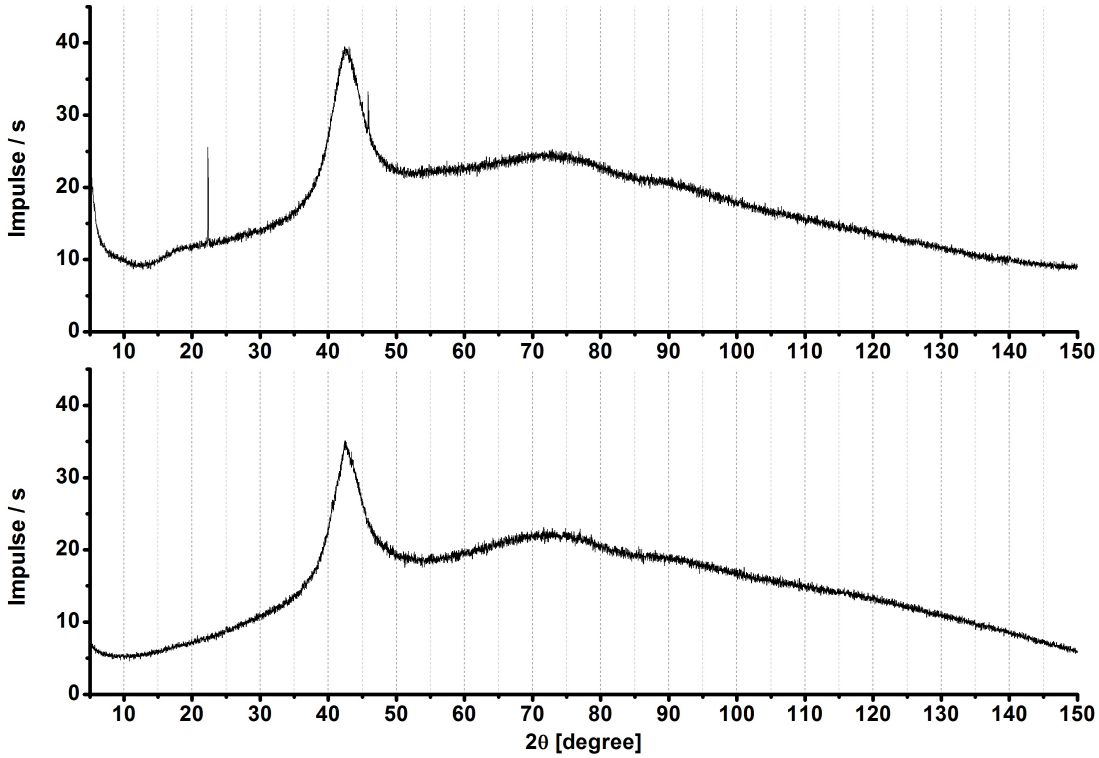


Figure 5.1: XRD-Plots of $Ni_{62}Nb_{38}$ obtained from suction casting. First graph corresponds to the sample casted in crucible for sample cross-sections of (1,0 X 8,0)mm. We assume that the refraction peaks correspond to crystalline phases. First graph corresponds to the sample casted in crucible for sample cross-sections of (1,0 X 3,0)mm.

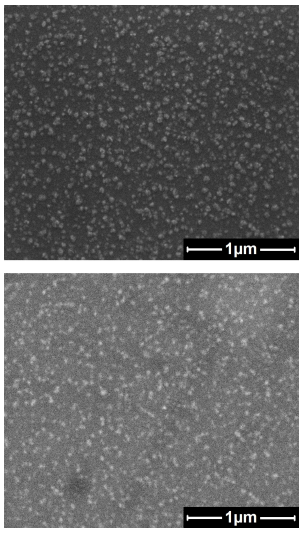


(a) Secondary electron imaging (top), and backscatter electron image (bottom).

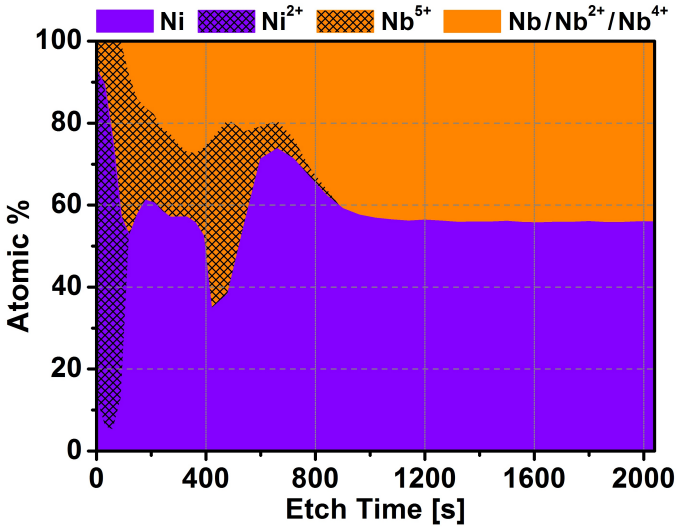


(b) Depth profile of elemental atomic fractions obtained with XPS.

Figure 5.2: Examination of surface oxide on $Ni_{62}Nb_{38}$ bulk metallic glass prepared at a temperature of 573K for 3 hours with SEM and XPS. The result of the XPS analysis is plotted as depth profile of the atomic concentration of constituents. Etching was performed by $Ar^+$ sputtering with a beam energy of 2kV.

metallic Ni shows a local maximum.

After cutting a cross-section lamella by FIB, the oxide layer was investigated by TEM. Fig. 5.3a shows the cross section of the metallic glass, the oxide layer, and the platinum cover, deposited as protection layer. The overall thickness of the oxide layer is about 30nm. Within the oxide, close to the transition to the metallic glass, crystalline rod-shaped structures with sizes of about 10nm were observed which are uniformly distributed.

The rod-shaped structures were identified as Ni by elemental mapping as depicted on the right side of a). The mapping confirms the appearance of Ni in the metallic glass and reveals its depletion within the oxide above the rod-shaped structures, where oxygen is apparently depleted. As can be seen in b), EDX analysis also revealed a high amount of Ni within the region of the structures but a lower amount of oxygen compared to the remaining layer. At each position, indicated by arrows in a), carbon was found which was most probably deposited during electron imaging. The Cu signal has its origin from the TEM holder at which the sample was attached, and the use of a Ga beam for ion-cutting during preparation for TEM can be identified as the source of the Ga signal. In c) the TEM images show the rod-shaped structures in high resolution. The crystalline structures can be assigned

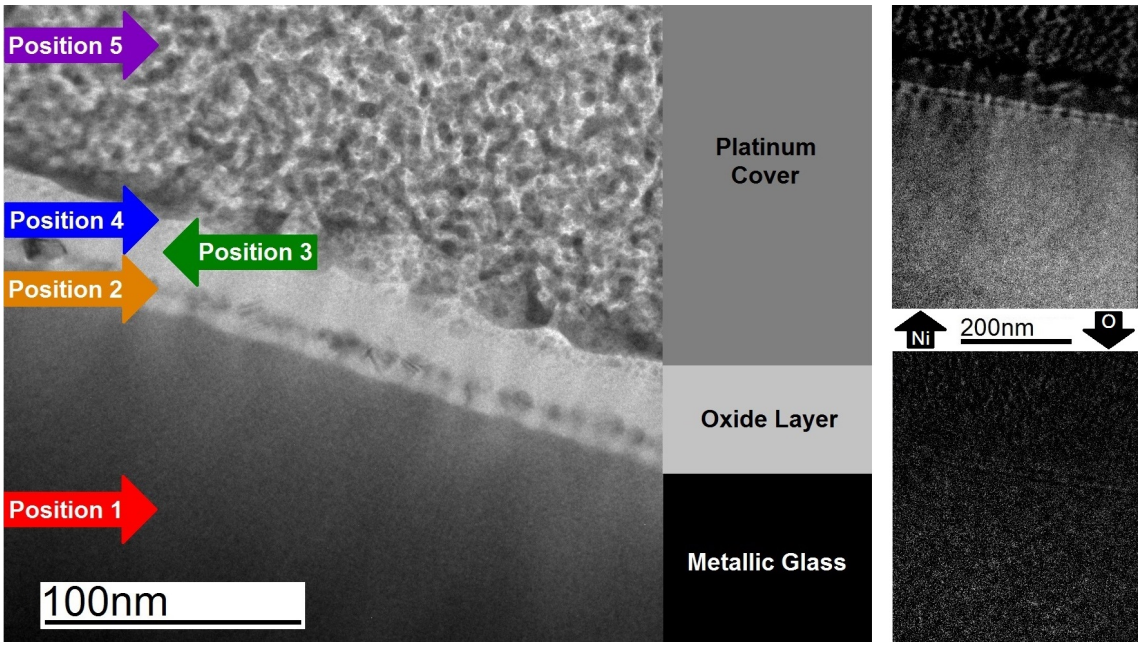


(a) Oxide layer and underlying metallic glass (left). Images on the right representing mappings of Ni (upper) and oxygen (lower) of the cross section.

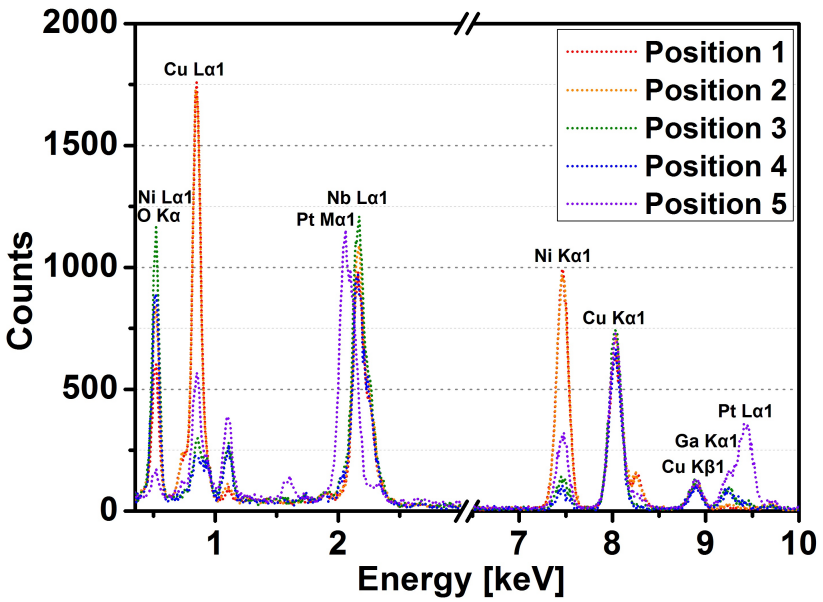


(b) Spectra of EDX analysis at positions indicated in a).

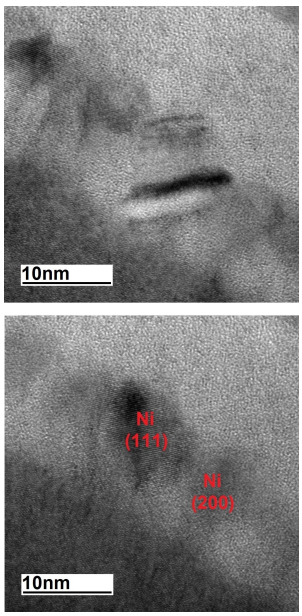


(c) Rod shaped Ni at the bottom of oxide layer with crystalline structures of Ni.

Figure 5.3: Cross sectional TEM analysis of an oxide layer on $Ni_{62}Nb_{38}$ bulk metallic glass prepared at a temperature of 573K for 3 hours after preparation by FIB technique.

to metallic Ni. The metallic glass at the transition to the oxide appears amorphous. The remaining oxide forms a matrix for the Ni rods and exhibits an amorphous structure, whereas crystalline inclusions are revealed by TEM images.
These findings are in agreement with the results from XPS analysis, where the Ni-rods were detected as local increase of the Ni signal within the oxide layer at the transition to the metallic glass. The increased amount of Nb above the rods was identified as $Nb_2O_5$ which appears together with the Ni content as mostly amorphous matrix. All these findings are in agreement to the findings in [86].
CS-AFM measurements were performed in contact-mode with a cantilever of type Adama. At constant load, a square area was repeatedly scanned line by line. The application of a bias voltage between sample and the electrically conductive tip resulted in an electric current. Assuming a homogeneous conductivity for the metallic glass, the spatial distribution of conductivity on the surface provides information about the electrical properties of the different components within the oxide layer.
Fig 5.4a shows the topography, the friction force, and the current for the fifth cycle with a normal force of $1\mu$N. In the topography we can see two round structures with diameters of about 100nm which appeared during the cyclic experiment. The friction force is correlated with the topography and within the scan frame it exhibits both, minimum and maximum friction in the regions of the round structures. The current signals in forward and backward scan direction were very similar to each other which suggests that we can exclude topographical effects due to different contact areas between tip and surface. The current was found to be increased in the regions of both structures and in addition, an increased conductivity in the upper part of the scan frame is indicated, where the smallest spatial extension of high conductivity was about 10nm. All observations concerning this experiment were reproducible in a way that the scan frames before and after this cycle showed similar results with the same spatial distribution. In fig. 5.4b the topography and the current are depicted on the oxidised surface after 15 cycles with a load of $7\mu$N on a square area of 400nm side length. In the center of the scan frame, wear of the surface oxide and the surrounding pileup is clearly visible. Similar to a), the current correlates with the topography, so that a high current was measured in the region of pileups. The normal force during the measurement was $1\mu$N and was chosen to achieve a sufficient electrical contact between tip and surface. Since wear on this surface was observed after the application of a normal force of 200nN, the topography in fig.4b may have been affected by the measurement.
Transport and accumulation of conductive surface material by the tip during the scratching process can be concluded. Assuming a higher conductivity of Ni than

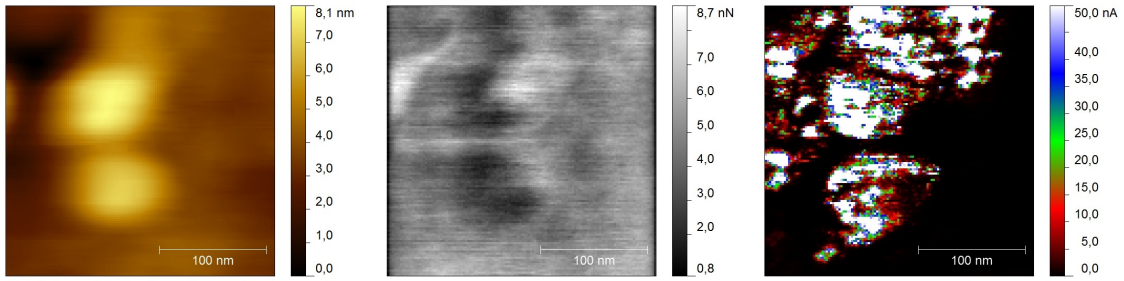


(a) Topography (left), friction force (center), and current (right) measured during the fifth cycle with an applied load of $1\mu$N.

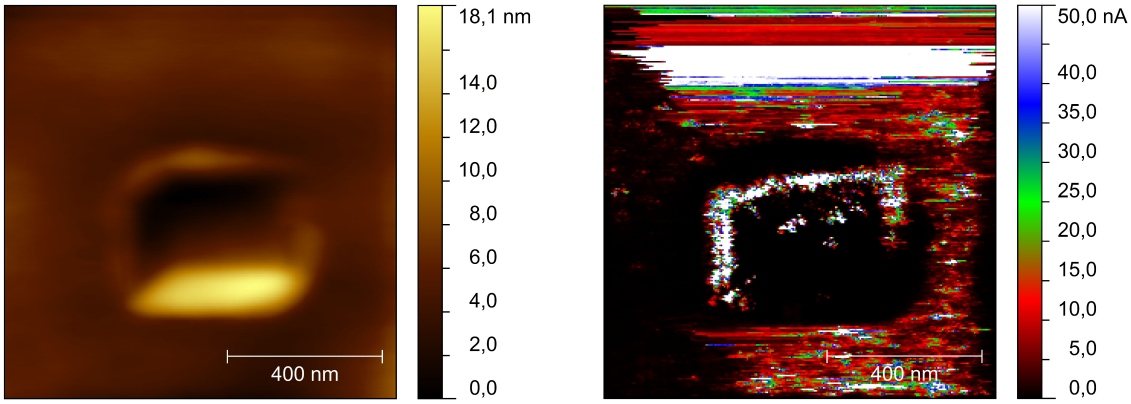


(b) Topography (left) and current (right) after 15 cycles with a load of $7\mu$N. From a value of 50nA the current exceeds the measuring range.

Figure 5.4: Contact-AFM measurements with square scan frame on the oxidised surface of $Ni_{62}Nb_{38}$ prepared at a temperature of 573K for 3 hours. Bias voltage was about -2,4V.

of $Nb_2O_5$, the motion of Ni-rods is suggested which is supported by the occurrence of surface regions with high conductivities and sizes of about 10nm which was estimated as the average size of Ni-rods within the oxide.

The experiments using CS-AFM on the oxidised surfaces of bulk metallic glass demonstrated how a strong contrast between the electrical conductivities of the oxide constituents can be used to investigate their relative motion. One of the challenges of the investigation of plastic deformation, performed with AFM, is to observe the site of the scratch, since it first has to be found again on the surface. Scratch length of only a few 100nm can only hardly be found when the sample was detached from the sample holder of the AFM. Even if the site was found by electron microscopy, considering structural sizes of 10nm, the spacial resolution provided by the device may be insufficient. Therefore, particles with a contrast in their physical properties within the oxide could enable a tracer method, similar as applied by Sakman, Burwell, and Irvine (1944) or Gregory (1946) by studying the distribution of radioactive particles in metal which were transported due to plastic deformation

during wear tests.(chapter 4 in [1])
According to [52], a significant difference in electronegativity between alloying metals leads to the preferential oxidation of the less noble elements and a partitioning of the constituents close to the surface. These are the prerequisites leading to an oxide layer structure in which agglomerates of the later oxidised nobler metals are embedded in an initially amorphous matrix of the oxidised less noble metals, just as described for the oxidation of $Zr_{60}Cu_{30}Al_{10}$ in chapter 3 and similar to the outcome for the oxidation of $Ni_{62}Nb_{38}$. This indicates that metallic glasses, consisting of noble and less noble metals, are prone to produces this kind of oxide layer structures. Noticeably, in (chapter 4 in [5]) it is referred to a correlation between glass forming ability and difference of electronegativities of alloying metals. Although this does not apply on any metallic glass system in general, a correlation between high glass forming ability and the characteristic structure of oxide layers, as found in this work and on similar metallic glass systems, for example in [48] and [51], might be possible. Further investigations could shed light on the underlying mechanisms of these phenomena.
Investigations on the dependence of friction and wear on the penetration rate have already been performed by Caron et. al. and showed a decrease of friction force and wear volume with increasing velocity. Due to increasing velocity an increase in the temperature is expected whose effect on friction and wear is still not well understood.[17][18]
Friction experiments on Zr based metallic glass with respect to roughness, after preparation of various groove-shaped surface structures by FIB technique were carried by Guo et. al in [87]. The authors observed a decreasing friction with increasing distribution density of grooves, each with a width of about 100nm, which were scanned perpendicular. Such kind of studies may provide the possibility to adjust friction and wear using controlled oxidation processes.
Surface changes induced by exothermic reactions such as crystallisation could be investigated after friction experiments, based on the experiments of Lewandowski and Greer, when the surfaces are coated with tin, which melts due to exothermic surface reactions and can be imaged after structural change due to its solidification under surface tension.[88]
The flow behavior and mechanical failure of metallic glasses is not controlled by defects but therefore is related to intrinsic properties of the material, such as the glass transition.[79] Investigations of metallic glasses with different glass transition temperatures may enable deeper understanding of the oxidation mechanisms of amorphous metals, and tribological experiments on the oxidised metallic glass surfaces

may give further insights into the mechanical interaction between the metals an their oxides.

Studies about delamination mechanisms between metal film and metal-oxide interfaces were carried out by Venkataraman et. al. in [89]. The authors found that the dissipated energy during micro-scale sliding on the thin film increased with increasing film thickness. In their model they related the normal stress and the shear stress during sliding on a thin deposited layer to the work of adhesion and found that the work of adhesion agrees well with the calculated van der Waals energy. In case of interfacial phenomena, such as the delamination of oxide from metallic glass surfaces on the nano-scale, this kind of investigation would effort the knowledge of elastic and shear moduli which, as shown in the previous chapter, are not reliably measurable on the nano-scale due to the characteristic deformation behavior of the oxide. On the micro-scale these parameters should be accessible since at larger scale deformation is less influenced by the oxide structure, so that this kind of evaluation could improve the understanding of the binding mechanisms between oxide and metallic glass.

Additional information on the mechanical properties of surface oxides can be expected by employing contact resonance measurements and FFM studies including in-situ oxidation under electrochemical control.

# References

[1] F.P. Bowden, D. Tabor. The Friction and Lubrication of Solids. *Oxford University Press New York*, reprinted 2008, ISBN: 978-0-19-850777-2

[2] E. Gnecco, E. Meyer. Fundamentals of friction and wear. *Springer-Verlag Berlin Heidelberg*, 2007, ISBN-13: 978-3-540-36806-9

[3] B. Bhushan. Nanotribology and Nanomechanics - An Introduction. *Springer-Verlag Berlin Heidelberg*, 2005, ISBN-13: 978-3-540-24267-3

[4] M.F. Ashby, A.L. Greer. Metallic glasses as structural materials. *Acta Materialia*, 10.1016/j.scriptamat.2005.09.051, 2005

[5] M. Miller, P. Liaw. Bulk Metallic Glasses - An Overview. *Springer Science+Business Media*, 2008, ISBN: 978-0-387-48920-9

[6] www.nature.com/news/mixed-up-metals-make-for-stronger-tougher-stretchier-alloys-1.19942 (last access: March 01, 2018)

[7] C.A. Schuh, T.G. Nieh. A nanoindentation study of serrated flow in bulk metallic glasses. *Acta Materialia*, 10.1016/S1359-6454(02)00303-8, 2002

[8] Y. Huang, Y.L.L. Chiu, J. Shen, Y. Sun, J.J.J. Chen. Mechanical performance of metallic glasses during nanoscratch tests. *Intermetallics*, 10.1016/j.intermet.2010.02.002, 2010

[9] D.-H. Lee, J.E. Evetts. Sliding friction and structural relaxation of metallic glasses. *Acta Metallurgica*, 10.1016/0001-6160(84)90006-3, 1984

[10] E. Fleury, S.M. Lee, H.S. Ahn, W.T. Kim, D.H. Kim. Tribological properties of bulk metallic glasses. *Materials Science and Engineering*, 10.1016/j.msea.2003.10.065, 2004

[11] B. Prakash. Abrasive wear behaviour of Fe, Co and Ni based metallic glasses. *Wear*, 10.1016/j.wear.2004.09.010, 2005

[12] B. Prakash, K. Hiratsuka. Sliding wear behaviour of some Fe-, Co- and Ni-based metallic glasses during rubbing against bearing steel. *Tribology Letters*, 2000

[13] D.F. Bahr, D.E. Kramer, W.W. Gerberich. Non-linear deformation mechanisms during nanoindentation. *Acta Materialia*, 10.1016/S1359-6454(98)00024-X, 1997

[14] D.E. Kramer, K.B. Yoder, W.W. Gerberich. Surface constrained plasticity: Oxide rupture and the yield point process. *Philosophical Magazine*, 10.1080/01418610108216651, 2009

[15] X.-Y. Fu, T. Kasai, M.L. Falk, D.A. Rigney. Sliding behavior of metallic glass: Part I. Experimental investigations. *Wear*, 10.1016/S0043-1648(01)00605-6, 2001

[16] X.-Y. Fu, M.L. Falk, D.A. Rigney. Sliding behavior of metallic glass: Part II. Computer simulations. *Wear*, 10.1016/S0043-1648(01)00607-X, 2001

[17] A. Caron, C.L. Qin, L. Gu, S. González, A. Shluger, H.-J. Fecht, D.V. Louzguine-Luzgin, A. Inoue. Structure and nano-mechanical characteristics of surface oxide layers on a metallic glass. *Nanotechnology*, 10.1088/0957-4484/22/9/095704, 2011

[18] A. Caron, P. Sharma, A. Shluger, H.-J. Fecht, D.V. Louzguine-Luzguin, A. Inoue. Effect of surface oxidation on the nm-scale wear behavior of a metallic glass. *Journal of Applied Physics*, 10.1063/1.3573778, 2011

[19] D.V. Louzguine-Luzguin, M. Ito, S.V. Ketov, A.S. Trifonov, J. Jiang, C.L. Chen, K. Nakajima. Exceptionally high nanoscale wear resistance of a $Cu_{47}Zr_{45}Al_8$ metallic glass with native and artificially grown oxide. *Intermetallics*, 10.1016/j.intermet.2017.10.011, 2017

[20] U. Koster, L. Jastrow. Oxidation of Zr-based metallic glasses and nanocrystalline alloys. *Materials Science and Engineering*, 10.1016/j.msea.2006.02.316, 2006

[21] S.J. Kang, K.T. Rittgen, S.G. Kwan, H.W. Park, R. Bennewitz, A. Caron. Importance of surface oxide for the tribology of a Zr-based metallic glass. *Friction*, 10.1007/s40544-017-0149-7, 2017

[22] P. Gabbott. Principles and Applications of Thermal Analysis. *Blackwell Publishing Ltd.* 2008, ISBN-13: 978-1-4051-3171-1

[23] Z.P. Lu, C.T. Liu. A new approach to understanding and measuring glass formation in bulk amorphous materials. *Intermetallics*, 10.1016/j.intermet.2004.04.032, 2004

[24] Renhong Tang, Bingwen Zhou,Yuejiao Ma, Fei Jia, Xingguo Zhan. Numerical Simulation of Zr-based Bulk Metallic Glass During Continuous Casting Solidification Process. *Materials Research*, 10.1590/1516-1439.319814, 2015

[25] H.Q.Li, J.H. Yan, H.J. Wu. Modelling and simulation of bulk metallic glass production process with suction casting. *Materials Science and Technology*, 10.1179/174328408X270248, 2009

[26] Yoshihiko Yokoyama, Tohru Yamasaki, Peter K. Liaw, Akihisa Inoue. Study of the structural relaxation-induced embrittlement of hypoeutectic Zr–Cu–Al ternary bulk glassy alloys. *Acta Materialia*, 10.1016/j.actamat.2008.08.026, 2008

[27] B. D. Cullity. Elements of X-ray Diffraction. *Addison-Wesley Publishing Company*, 1956, ISBN 978-0201012309

[28] A. Gebert, J. Eckert and L. Schultz. Effect of oxygen on phase formation and thermal stability of slowly cooled $Zr_{65}Al_{7,5}Cu_{17,5}Ni_{10}$ metallic glass. *Acta Materialia*, 10.1016/S1359-6454(98)00187-6, 1998

[29] H.E. Kissinger. Reaction Kinetics in Differential Thermal Analysis. *Analytical Chemistry*, 10.1021/ac60131a045, 1957

[30] C.T. Moynihan, A.J. Easteal, J. Wilder, J. Tucker. Dependence of the Glass Transition Temperature on Heating and Cooling Rate. *The Journal of Physical Chemistry*, 10.1021/j100619a008, 1974

[31] S. Gaisford, Evaluation of Analytical Instrumentation. Part XXV: Differential Scanning Calorimetry, *Analytical Methods*, 10.1039/c4ay90087a, 2015

[32] A.M. Kamath. Glass forming ability and relaxation behavior of Zr based metallic glasses. http://oaktrust.library.tamu.edu/bitstream/handle/1969.1/ETD-TAMU-2011-05-9044/KAMATH-THESIS.pdf?sequence=2&isAllowed=y, 2011, (last access: March 31, 2018)

[33] Z. Černošek, J. Holubová, E. Černošková, M. Liška. Enthalpic Relaxation and the glass transition. *Journal of Optoelectronics and Advanced Materials*, 2002

[34] N. Mehta, A. Kumar. Applicability of Kissinger's relation in the determination of activation energy of glass transition process. *Journal of Optoelectronics and Advanced Materials*, 2005

[35] G. Petzow. Metallographisches, Keramographisches, Plastographisches Ätzen. *Gebrüder Borntraeger Berlin, Stuttgart*, 2006, ISBN 3-443-23016-4

[36] M. Bakkal, C.T. Liu, T.R. Watkins, R.O. Scattergood, A.J. Shih. Oxidation and crystallization of Zr-based bulk metallic glass due to machining. *Intermetallics*, 10.1016/j.intermet.2003.09.017 ,2004

[37] A. Gebert, P.F. Gostin, L. Schultz. Effect of surface finishing of a Zr-based bulk metallic glass on its corrosion behavior. *Corrosion Science*, 10.1016/j.corsci.2010.01.027, 2010

[38] Tapobrata Som, Dinakar Kanjilal. Nanofabrication by Ion-Beam Sputtering. *Pan Stanford Publishing*, 2013, ISBN-13: 978-9-81430-376-7

[39] P. Sigmund. Theory of Sputtering. I. Sputtering Yield of Amorphous and Polycrystalline Targets. *Physical Review*, 10.1103/PhysRev.187.768, 1969

[40] Q. Wei, K.-D. Li, J. Lian, L. Wang. Angular dependence of sputtering yield of amorphous and polycrystalline materials. *Journal of Physics D – Applied Physics*, 10.1088/0022-3727/41/17/172002, 2008

[41] A.S. Khanna. Introduction to High Temperature Oxidation and Corrosion. *ASM International*, 2002, ISBN: 0-87170-762-4

[42] C.Y. Tam, C.H. Shek, W.H. Wang. Oxidation behaviour of a Cu-Zr-Al bulk metallic glass. *Advanced Materials Science*, 2008

[43] C.Y. Tam, C.H. Shek, Oxidation behavior of $Cu_{60}Zr_{30}Ti_{10}$ bulk metallic glass. *Journal of Materials Research*, 10.1557/JMR.2005.0182, 2005

[44] U. Köster, D. Zander, Triwikantoro. Hydrogenation and oxidation of Zr-based metallic glasses, quasicrystalline or nanocrystalline alloys. *Journal of Metastable and Nanocrystalline Materials*, 10.4028/www.scientific.net/JMNM.8.203, 2000

[45] H. Bethge, J. Heydenreich. Elektronenmikroskopie in der Festkörperphysik. *Deutscher Verlag der Wissenschaften*, 1982, ISBN: 978-3-642-93212-0

[46] R. Gauvin. A Universal Equation for the Emission Range of X Rays from Bulk Specimens. *Microscopy and Microanalysis*, 10.1017S143192760707081X, 2007

[47] D.J. O'Connor, B.A. Sexton, R.St.C. Smart. Surface analysis methods in material science. *Springer-Verlag Berlin Heidelberg*, 2003, ISBN: 978-3-642-07458-5

[48] C.Y. Tam, C.H. Shek. Oxidation-induced copper segregation in $Cu_{60}Zr_{30}Ti_{10}$ bulk metallic glass. *Journal of Materials Research*, 10.1557/JMR.2006.0120, 2005

[49] J.-H. Park, K. Natesan. Oxidation of Copper and Electronic Transport in Copper Oxides. *Oxidation of Metals*, 10.1007/BF00664664, 1993

[50] S.-K. Lee, H.-C. Hsu, W.-H. Tuan. Oxidation Behavior of Copper at a Temperature below 300°C and the Methodology for Passivation. *Materials Research*, 10.1590/1980-5373-MR-2015-0139, 2015

[51] D.V. Louzguine-Luzgin, C.L. Chen, L.Y. Lin, Z.C. Wang, S.V. Ketov, M.J. Miyama, A.S. Trifonov, A.V. Lubenchenko, Y. Ikuhara. Bulk metallic glassy surface native oxide: Its atomic structure, growth rate and electrical properties. *Acta Materialia*, 10.1016/j.actamat.2015.06.039, 2015

[52] S. Stanojevic, I. Gallino, H. Aboulfadl, M. Sahin, F. Mücklich, R. Busch. Oxidation of glassy Ni-Nb-Sn alloys and its influence on the thermodynamics and kinetics of crystallization. *Acta Materialia*, 10.1016/j.actamat.2015.09.009, 2016

[53] Y. Shen. Carbothermal synthesis of metal-functionalized nanostructures for energy and environmental applications. *Journal of Materials Chemistry A*, 10.1039/c5ta01228g, 2015

[54] B. Wang, D.Y. Huang, N. Prud'hommea, Z. Chen, F. Jomard, T. Zhang, V. Ji. Diffusion mechanism of Zr-based metallic glass during oxidation under dry air. *Intermetallics*, 10.1016/j.intermet.2012.04.003, 2012

[55] L.P.H. Jeurgens, A. Lyapin, E.J. Mittemeijer. The mechanism of low-temperature oxidation of zirconium. *Acta Materialia*, 10.1016/j.actamat.2005.06.028, 2005

[56] C. Edelmann. Vakuumphysik - Grundlagen, Vakuumerzeugung und -messung, Anwendungen. *Spektrum Akademischer Verlag, Heidelberg Berlin*, 1998, ISBN: 3-8274-0007-4

[57] B. Voigtländer. Scanning Probe Microscopy - Atomic Force Microscopy and Scanning Tunneling Microscopy. *Springer-Verlag Berlin Heidelberg*, 2015, ISBN: 978-3-662-45239-4

[58] H.-J. Butt, B. Cappella, M. Kappl. Force measurements with the atomic force microscope: Technique, interpretation and applications. *Surface Sience Reports*, 10.1016/j.surfrep.2005.08.003, 2005

[59] V.L. Popov. Contact Mechanics and Friction - Physical principles and applications, *Springer-Verlag Berlin Heidelberg*, ISBN: 978-3-642-10802-0, 2010

[60] M.H. Müser. On the Linearity of Contact Area and Reduced Pressure. *Tribology Letters*, 10.1007/s11249-017-0912-y, 2017

[61] R. Aghababaei, D.H. Warner, J.-F. Molinari. Critical length scale controls adhesive wear mechanisms. *Nature Communications*, 10.1038/ncomms11816, 2016

[62] A. Caron, D. V. Louzguine-Luzguin, and R. Bennewitz. Structure vs Chemistry: Friction and Wear of Pt-Based Metallic Surfaces. *Applied Materials and Interfaces*, 10.1021/am403564a, 2013

[63] S.V. Meschel, O.J. Kleppa. Standard enthalpies of formation of some 4d transition metal silicides by high temperature direct synthesis calorimetry, *Journal of Alloys and Compounds*, 10.1016/S0925-8388(98)00504-0, 1998

[64] M. Gutowski, J.E. Jaffe, C.-L. Liu, M. Stoker, R.I. Hegde, R.S. Rai, P.J. Tobin. Thermodynamic stability of high-K dielectric metal oxides $ZrO_2$ and $HfO_2$ in contact with Si and $SiO_2$. *Applied Physics Letters*, 10.1063/1.1458692, 2002

[65] R.R. Chromik, W.K. Neils, E.J. Cotts. Thermodynamic and kinetic study of solid state reactions in the Cu-Si system. *Journal of Applied Physics*, 10.1063/1.371357, 1999

[66] R.D. Holmes, H.ST.C. O'Neill, R.J. Arculus. Standard Gibbs free energy of formation for $Cu_2O$, NiO, CoO, and $Fe_xO$: High resolution electrochemical measurements using zirconia solid electrolytes from 900-1400K. *Ceochimica el Cosmochimica Acta*, 10.1016/0016-7037(86)90027-X, 1986

[67] E. Gnecco, R. Bennewitz, E. Meyer. Abrasive wear on the atomic scale. *Physical Review Letters*, 10.1103/PhysRevLett.88.215501, 2002

[68] A.M.F. Rivas, R.R.M. Zamora, R. Prioli. Lateral force microscopy profiles for amorphous potentials. *Ultramicroscopy*, 10.1016/S0304-3991(03)00057-3, 2003

[69] A. D. Craciun, J. L. Gallani, M. V. Rastei. Stochastic stick–slip nanoscale friction on oxide surfaces. *Nanotechnology*, 10.1088/0957-4484/27/5/055402, 2016

[70] J. Antonowicz, A. Pietnoczka, W. Zalewski, R. Bacewicz, M. Stoica, K. Georgarakis, A.R. Yavari. Local atomic structure of Zr–Cu and Zr–Cu–Al amorphous alloys investigated by EXAFS method. *Journal of Alloys and Compounds*, 10.1016/j.jallcom.2010.10.105, 2010

[71] A. Socoliuc, R. Bennewitz, E. Gnecco, E. Meyer. Transition from Stick-Slip to Continuous Sliding in Atomic Friction: Entering a New Regime of Ultralow Friction. *Physical Review Letters*, 10.1103/PhysRevLett.92.134301, 2004

[72] Z.J. Wang, T.-B. Ma, Y.-Z. Hu, L. Hu, H. Wang. Friction Energy dissipation of atomic-scale friction based on one-dimensional Prandtl-Tomlinson model. *Friction*, 10.1007/s40544-015-0086-2, 2015

[73] S. Kawai, C. Held, T. Glatzel. Automated amplitude calibration in non-contact AFM mode, Nanonis Application Note. www.specs-zurich.com/upload/cms/user/AN-AmplitudecalibrationncAFM.pdf, (last access: April 01, 2018)

[74] P.L. Menezes, S.P. Ingole, M. Nosonovsky, S.V. Kailas, M.R. Lovell. Tribology for Scientists and Engineers - From Basics to Advanced Concepts. *Springer Science+Business Media New York*, 2013, ISBN: 978-1-4614-1944-0

[75] R. Colaço. An AFM study of single-contact abrasive wear: The Rabinowicz wear equation revisited. *Wear*, 10.1016/j.wear.2008.12.024, 2009

[76] R. Bhowmick, R. Raghavan, K. Chattopadhyay, U. Ramamurty. Plastic flow softening in a bulk metallic glass. *Acta Materialia*, 10.1016/j.actamat.2006.05.011, 2006

[77] T.O. Mulhearn, L.E. Samuels. The Abrasion of Metals: A Model of the Process. *Wear*, 10.1016/0043-1648(62)90064-9, 1962

[78] D.A. Rigney. The roles of hardness in the sliding behavior of materials. *Wear*, 10.1016/0043-1648(94)90169-4, 1994

[79] T. Egami, T. Iwashita, W. Dmowski. Mechanical Properties of Metallic Glasses. *Metals*, 10.3390/met3010077, 2013

[80] S.J. Bull, E.G. Berasetegui. An overview of the potential of quantitative coating adhesion measurement by scratch testing. *Tribology International*, 10.1016/j.triboint.2005.04.013, 2006

[81] R. T. Qu, J. Eckert, Z. F. Zhang. Tensile fracture criterion of metallic glass. *Journal of Applied Physics*, 10.1063/1.3580285, 2011

[82] X. K. Xi, D. Q. Zhao, M. X. Pan, W. H. Wang, Y. Wu, J. J. Lewandowski. Fracture of Brittle Metallic Glasses: Brittleness or Plasticity. *Physical Review Letters*, 10.1103/PhysRevLett.94.125510, 2005

[83] Z. Zhang, V. Keppens, P.K. Liaw, Y. Yokoyama, A. Inoue. Elastic properties of Zr-based bulk metallic glasses studied by resonant ultrasound spectroscopy. *Journal of Materials Research*, 10.1557/JMR.2007.0040, 2007

[84] X. Li, H. Gao. Nanoindentation of $Cu_2O$ Nanocubes. *Nano Letters*, 10.1021/nl048941n, 2004

[85] C.A. Klein, G.F. Cardinale. Young's modulus and Poisson's ratio of CVD diamond. *Diamond and Related Materials*, 10.1016/0925-9635(93)90250-6, 1993

[86] D.V. Louzguine-Luzgin, T. Hitosugi, N. Chen, S.V. Ketov, A. Shluger, V.Yu. Zadorozhnyy, A. Caron, S. Gonzáles, C.L. Qin, A. Inoue. Investigation of transparent magnetic material formed by selective oxidation of a metallic glass. *Thin Solid Films*, 10.1016/j.tsf.2013.01.006, 2013

[87] D. Guo, X. Chen, C. Zhang, X. Wu, Z. Liu, K. Li, J. Zhang, C. Wang. Nanoscale tunable reduction of interfacial friction on nano-patterned wearresistant bulk metallic glass. *Applied Surface Science*, 10.1016/j.apsusc.2018.05.095, 2018

[88] J.J. Lewandowski, A.L. Greer. Temperature rise at shear bands in metallic glasses. *Nature Materials*, 10.1038/nmat1536, 2016

[89] S. Venkataraman, D.L. Kohlstedt, W.W. Gerberich. Continuous microscratch measurements of the practical and true works of adhesion for metal/ceramic systems. *Journal of Materials Research*, 10.1557/JMR.1996.0398, 1996

**Acknowledgements**

I thank my supervisor, Prof. Dr. Bennewitz, who offered me the opportunity to carry out the research presented in this thesis and to be part of the Nanotribology-group of the Leibniz Institute for New Materials (INM). In addition, I am grateful for many discussions and advices, for his continuous support, and for the trust he has placed in me with the technical support of the UHV-Lab.

I would like to thank Prof. Dr. Birringer for valuable discussions and advices, especially during the period of writing this thesis.

Special thanks to Prof. Dr. Arnaud Caron for the thorough scientific and technical introductions and advices, for many discussions, for the time he took for me, and for his friendship.

Thanks to Dr. Marcus Koch, who always encouraged and supported me, for his valuable contributions by means of electron microscopy. In addition, I thank the Physical Analysis group of the Leibniz Institute for New Materials, including Birgit Heiland for her comprehensive assistance with preparations, and Rudolf Karos for his support with XRD measurements.

I owe thanks to Robert Drumm for the introduction in thermal analysis methods and the numerous surface oxidations by TGA.
I thank Jörg Schmauch for interesting discussions regarding electron microscopy, and Dr. Frank Müller for his advices on XPS.

I am grateful to the entire INM for the friendly atmosphere within the institute, and for the very pleasant time. Special thanks to the director of the institute, Prof. Dr. Arzt, for his continuous support.

The entire research group "Nanotribology" deserves my thanks for the family atmosphere: Novaf Özgün, Dr. Xianqiang Pei, Dr. Johanna Blass, Günther Krämer, Haoran Ma, and the former colleagues Annika Diehl, Dr. Christiane Petzold, Dr. Balakrishna Soorali Ganeshamurthy, Dr. Arzu Colak, and Dr. Bianca Bozna

I thank Dr. Michael Opsölder for the pleasant office atmosphere and for many advices regarding chemical issues.

I am grateful to the German Research Foundation (DFG) for promoting this research project.

Finally, I thank my family, friends and everyone who supported me.